Measurement of differential cross sections for top quark pair production in pp collisions at $\sqrt{s} = 7$ TeV with the ATLAS detector

Miho Yamada

Doctor of Philosophy

The Graduate University for Advanced Studies
School of High Energy Accelerator Science
Department of Particle and Nuclear Physics

2012

Abstract

Measurement of differential cross sections for top quark pair production in proton-proton collisions at a center of mass energy of 7 TeV are described. They are measured as a function of the mass and the the rapidity of the top-anti-top ($t\bar{t}$) system using lepton (electron and muon)+jets events. The purpose of this study is the verification of the standard model by precise measurement of the production cross section of the heaviest fermion in high center of mass energy and high luminosity collision. In addition top quark has an important part to play in a beyond the standard model. New particles which couple to a top quark pair directly so that we observe signal of new physics on the invariant mass distribution of the $t\bar{t}$ system. Differential cross section as a function of the mass of the $t\bar{t}$ system has already measured at Tevatron however there was no evidence of new physics. This analysis based on the data of 4.7 fb^{-1} luminosity recorded by the ATLAS detector at LHC center of mass energy of 7 TeV of pp collisions in 2011, Measured differential cross sections are consistent with the standard model expectations.

Contents

List of Figures

List of Tables

Chapter 1

Introduction

1.1 Top Quark

The standard model of elementary particle physics [1] is the theory which gives an account of the interactions (mediated by gauge bosons) between matter elementary particles (fermions). It includes 12 flavors of fermions (spin-1/2), 6 flavors of quarks and 6 flavors of leptons, 4 gauge bosons (spin-1) which mediate forces between fermions and one scalar elementary particle (Higgs boson). The standard model well describes many current experimental results of the particle physics. In the summer of 2012, two experiments of the Large Hadron Collider at CERN, the ATLAS experiment observed a Higgs boson, which was the last undiscovered member of the standard model, with the significance of $5.9\,\sigma$ [2]. All fermions in the standard model, six quarks and six leptons, are shown in Table 1.1 [3], which form three weak-isospin doublets. They interact with each other by exchanging gauge bosons which are shown in Table 1.2. The six leptons consist of neutrinos and charged leptons. Neutrinos interact only weakly with other fermions via exchange of massive gauge bosons (Z and W) and charged leptons take part both in weak and electromagnetic interactions mediated by photons. The six flavors of quarks are classified into two prototypes of first generation, *up*-type and *down*-type. Quarks interact with other quarks via strong interaction mediated by gluons as well as weak and electromagnetic interactions. The top quark is the third generation up-type quark.

The top quark was discovered directly by the CDF and DØ experiments at the Tevatron [4, 5, 6] a proton-antiproton collider at a center of mass energy $\sqrt{s} = 1.8\,\mathrm{TeV}$ at Fermilab in 1995. The properties of the top quark are studied by experiments of the Tevatron and also of the LHC, and the average of published top mass measurements from Tevatron Run-I (1992–1996), Run-II (2001–2011) and the LHC (2008–) is $173.5 \pm 0.6 \pm 0.8\,\mathrm{GeV}$.

The top quark interacts by the strong interaction but decays only through the weak interaction. It decays into a W boson and a bottom quark almost in 100%.

Table 1.1: Fermions of the standard model. Their masses, charges and spins are shown.

Fermions	Charge $[e]$	Isospin	Generation		
			1	2	3
Quarks	$+\frac{2}{3}$	$+\frac{1}{2}$	u	c	t
	$-\frac{1}{3}$	$-\frac{1}{2}$	d	s	b
Leptons	0	$+\frac{1}{2}$	ν_e	ν_μ	ν_τ
	-1	$-\frac{1}{2}$	e	μ	τ

Table 1.2: Gauge bosons.

Gauge bosons	Mass [GeV]	Charge $[e]$	Interactions
Photon (γ)	0	0	electromagnetic
Gluon (g)	0	0	strong
Z boson (Z^0)	91.1876	0	weak
W boson $(W^\pm)$	80.385	± 1	weak

1.2 Production and Decays of the Top Quark Pair

1.2.1 Production Processes and Total Production Cross Section

The top quark pair production at high energy hadron collisions is well described by the Standard Model. The Feynman diagrams of the top quark pair production in the hadron collisions at the leading-order (LO) are shown in Figure 1.1. The total top quark pair production cross section for hard scattering processes at a center of mass energy $\sqrt{s}$ can be expressed by the following formula:

$$\sigma_{t\bar{t}}(\sqrt{s}, m_t) = \sum_{i,j=q,\bar{q},g} \int dx_i dx_j f_i(x_i, \mu^2) \bar{f}_j(x_j, \mu^2) \times \hat{\sigma}^{ij \to t\bar{t}}(\hat{s}) \tag{1.1}$$

where i and j are parton flavors, q, $\bar{q}$ and g, in the initial hadron, respectively, and $x_{i(j)}$ is their energy fraction with respect to their parent hadron. The total cross section is separated into two pieces, a short distance and a long distance ones. In eq. (1.1) the short distance part is expressed
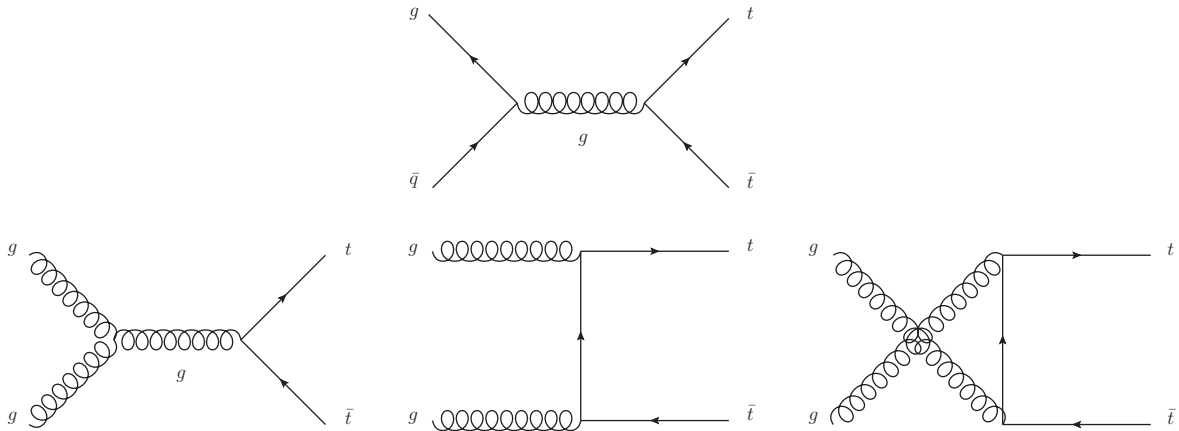
Figure 1.1: The top diagram shows the top quark production process via quark-anti-quark collision and the bottom three show that via gluon-gluon processes.

as $\hat{\sigma}^{ij \to t\bar{t}}(\hat{s})$ which is a cross section of the $t\bar{t}$ production via a hard collisions of partons (i and j) at the collision energy of $\sqrt{\hat{s}}$. The long distance part comes from the soft parton emissions from the initial partons (SR). In eq. (1.1) the probability to find a parton of flavor i with an energy fraction of x (PDF) is expressed as $f_i(x_i, \mu_F^2)$ where μ_F^2 is a energy scale of the separation between the short and the long distance parts. In Figure 1.3 [7] PDFs with the example parametrization obtained by the CTEQ [8] collaboration are shown. Since the typical energy fraction for the $t\bar{t}$ production is small ($2m_t/\sqrt{s} \approx 0.05$) at the LHC energy, the contribution of gluon collisions to the total cross section becomes very large due to the large PDF value. On the other hand that of $q\bar{q}$ collisions is small because the PDF value of $\bar{q}$ is small. At $\sqrt{s} = 7\,\text{TeV}$ the cross section of gluon-gluon collisions becomes about 90% of the total cross section and that of quark-antiquark annihilation is about 10%.

In Figure 1.2 the total production cross section of the top quark pair production is shown as a function of collision energies for hadron colliders (pp and $p\bar{p}$). The measured cross sections at Tevatron [9, 10] and LHC [11, 12, 13, 14] are compared to theoretical calculations in NLO (next-to-leading-order) by lines (solid and dot-dashed) and also approximate NNLO (next-to-next-to-leading) [15] with colored bands. At the LHC energy of $\sqrt{s} = 7\,\text{TeV}$, the theoretical prediction of the $t\bar{t}$ production cross section by the approximate NNLO calculation with $m_t = 172.5\,\text{GeV}$ becomes $\sigma_{t\bar{t}} = 166.8^{+16.5}_{-17.8}$ pb, whereas the combined cross section of the latest ATLAS measurement is 177^{+11}_{-10} pb.

1.2.2 Decay of the Top Quark Pair

The final state of the top quark pair production process is categorized according to the combination of decay modes of two W bosons in the final state. The W boson decays a charged lepton (e, μ and τ) and neutrino (ν_e, ν_μ and ν_τ) with a branching fraction 11%. They are observed as an isolated lepton with high transverse momentum and a missing transverse energy in a detector.
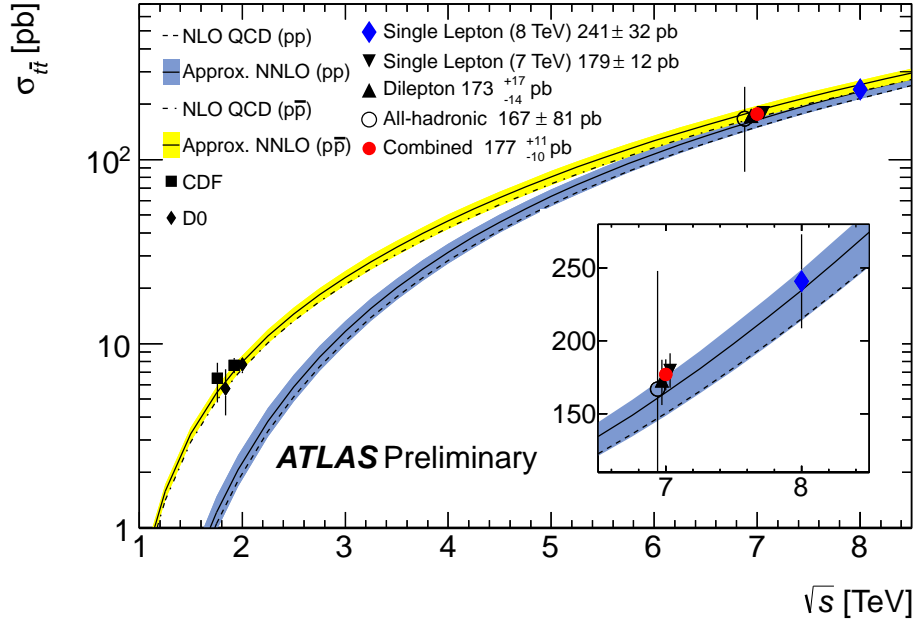
Figure 1.2: $t\bar{t}$ cross section as a function of the center of mass energy.
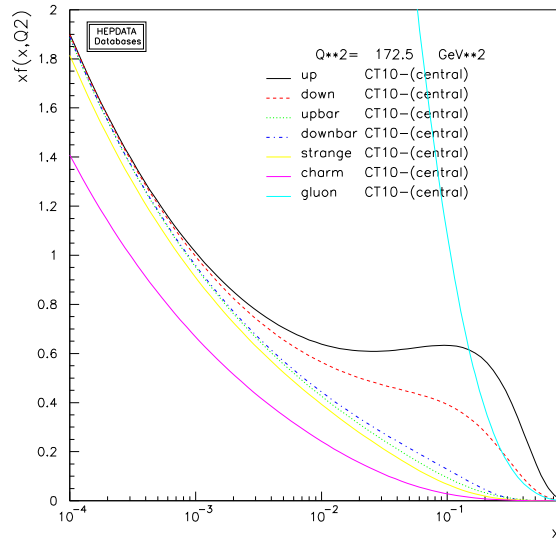
Figure 1.3: Parton distribution function $f_i(x_i, \mu_F^2)$ for scale of $Q^2 = \mu_F^2 = 172.5\,\text{GeV}$ obtained by the CTEQ collaboration (CT10 [8]).

The W boson also decays into a pair of quarks ($W \rightarrow q\bar{q}'$) with a branching fraction of 67% and these quarks are observed as jets in a detector.

Top Pair Branching Fractions
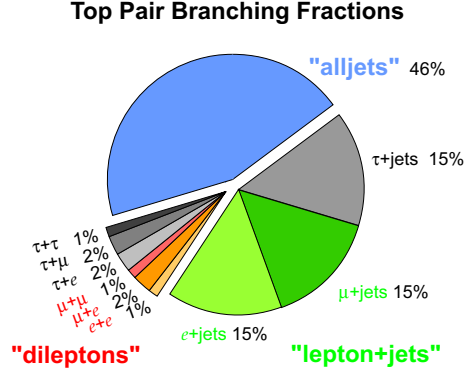
Figure 1.4: Top pair branching fractions

The following list shows the possible combination of decays of two W bosons in the final state of the top quark pair production.

A: All hadronic channel $t\bar{t} \rightarrow (W^+b)(W^-\bar{b}) \rightarrow (q\bar{q})b\,(q\bar{q})\bar{b}$

Both W bosons decay into a quark pair, resulting six hadronic jets (2 b-jets + 4 light quark jets) in its final state. This channel has a large branching ratio of 46% as shown in Figure 1.4, but suffers from the large amount of irreducible QCD background.

B: Lepton+jets channel $t\bar{t} \rightarrow (W^+b)(W^-\bar{b}) \rightarrow (q\bar{q}')b\,(\ell\nu_\ell)\bar{b} + (\ell\nu_\ell)b\,(q\bar{q}')\bar{b}$

One of the W boson decays into a quark pair, another one decays into a charged lepton and a neutrino. This channel has also a large branching fraction of 15% for each lepton flavor, e, μ and τ. This channel has a high transverse momentum charged lepton, a missing transverse energy of the neutrino, two light quark jets and two b-jets in the final state. We consider only e and μ channel as a signal in this analysis due to a complexity of τ decay patterns. In the lepton+jets channel the W boson which decays into a charged lepton and neutrino can be reconstructed from a single lepton and missing transverse energy without any combinatorial backgrounds.

C: Di-lepton channel $t\bar{t} \rightarrow (W^+b)(W^-\bar{b}) \rightarrow (\ell\nu_\ell)b\,(\ell\nu_\ell)\bar{b}$

Both W bosons decay into a lepton and a neutrino. In the final state of this channel, there are two high transverse momentum charged lepton, a large missing transverse energy from two neutrino and two b-quark jets. The signal to background ratio is much better than lepton+jets channel due to two high transverse momentum charged leptons. However, its branching fraction is only 7% for e and μ. Since two neutrinos are missing in the final state, it is difficult to reconstruct the $t\bar{t}$ system.

The signal process of this study is the "lepton+jets" decay channel because it has a good S/N ratio and a large branching fraction, and the kinematics of the final state can be reconstructed.

5

The total production cross section of top quark pair has been already measured precisely with a large amount of $t\bar{t}$ events and this enables to investigate the detail of properties of top quark pair production in terms of characteristic variables of the $t\bar{t}$ system. At first, the purpose of this analysis is verification of the standard model. To compare the differential cross sections as a function of kinematic variables of $t\bar{t}$ system to theoretical predictions directly, we can know the consistency of the standard model. Currently accurate theoretical predictions for the $t\bar{t}$ invariant mass distribution $(m_{t\bar{t}})$ at NLO and next-to-next-to-leading logarithm (NNLL) are available [16], [17]. The $t\bar{t}$ invariant mass is sensitive to physics beyond the standard model such as s-channel resonances that can change the shape of the differential cross section and will show details at Section 1.3. The shape of the rapidity of the $t\bar{t}$ system will be also changed and can be seen excess at central region at the region of s-channel resonances on $m_{t\bar{t}}$. The theoretical prediction for the $t\bar{t}$ system rapidity at NLO is available [16].

1.3 New Particle Search and Top Pair Final States

In some models of new physics beyond the Standard Model, gauge couplings to the third generation are enhanced. These include Kaluza-Klein excitations of graviton and the weak and the strong gauge bosons which couple to top quarks. Such particles can be seen as resonances in the $pp \rightarrow X \rightarrow t\bar{t}$ production and not in other channels like di-jets or di-leptons due to their small couplings to light fermions in this section. We consider the possible effects on the observed invariant mass distribution of the top quark pair system induced by new heavy resonances. We use MadGraph [18] with "topBSM" model which describes top quark pair resonance productions by new physics beyond the Standard Model.

As an example, we discuss a spin-1 resonance production by $q\bar{q}$ annihilations that can be a color singlet or color octet. An s-channel color singlet vector boson, such as Z', in the $t\bar{t}$ production process gives a simple peak in the invariant mass spectrum of the top quark pair. The precise width and height of the peak depends on model parameter of new physics. Assuming the $m_{Z'} = 2$ TeV and the same coupling strength to fermions as the Standard Model Z boson, the mass distribution of the Z' signal as well as the Standard model background are shown in Figure 1.5 with a blue histogram at $\sqrt{s} = 7$ TeV with 4.7 fb^{-1}. If the Standard Model coupling is assumed, we find that expected signal of Z' in the top quark pair resonance search is very small. In Figure 1.5 the signal of a color octet spin-1 particle is also shown as a red histogram at the same energy and integrated luminosity as the color singlet case. We assume that the coupling strength to fermions of a color acted vector particle is equal to the strong coupling constant. Due to the larger coupling to fermions than color singlet case, the larger signal production is expected. We estimate the signal strength for above examples in the highest $t\bar{t}$ mass bin, 950-2700 GeV of our analysis. For the color singlet case, the signal to noise ratio is only ~ 2, and that becomes about for ~ 8 the color octet case. We find that the new physics signal produced with the strength of the standard model electro-weak coupling is rather small in our analysis.
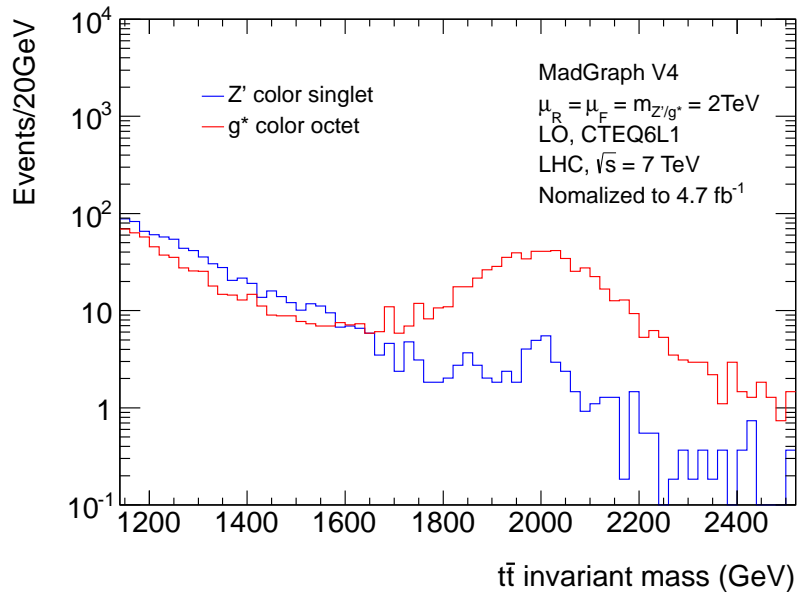
Figure 1.5: The mass of the $t\bar{t}$ system at $\sqrt{s} = 7\,\mathrm{TeV}$ in pp collisions and normalized to 4.7 fb[-1] that corresponds to the collision data for this analysis. The mass of the new particles (color singlet and octet), renormalization scale μ_R and factorization scale μ_F assume 2 TeV and generate the events at LO with MadGraph [18].

Chapter 2

Experimental Measurement of Top Pair Production Differential Cross Section

In this analysis, we measure the differential cross sections of kinematic variables of the $t\bar{t}$ system, $m_{t\bar{t}}$ and $y_{t\bar{t}}$. These variables are obtained by reconstructing the top and anti-top decays from detected objects in selected event samples. Event selection criteria are optimized to select the top quark pair production with subsequent decays into the lepton+hadron channel. Contamination from background processes such as other physics processes and other decay channels of the top quark production are estimated by using real data as well as simulated samples. From observed distributions of the reconstructed variables, $m_{t\bar{t}}$ and $y_{t\bar{t}}$, their differential cross sections are finally obtained by correcting for detector effects using the unfolding technique. In this chapter experimental procedure to measure the differential cross sections is summarized.

2.1 Data

Data used in this analysis was collected by the ATLAS detector at the LHC with $\sqrt{s} = 7$ TeV in 2011. The corresponding integrated luminosity is 4.7 fb^{-1} 2.1. The instantaneous luminosity gradually increased during the data taking in 2011 and reached $\sim 3.65 \times 10^{33}$ cm^{-2}s^{-1} at the end of the year. Figure 2.2 shows the history of the peak luminosity per beam fill during the year of 2011. As shown in this plot, the data taking in 2011 can be divided into several periods and the beam condition of each period is extremely different from each other.

In the high luminosity collisions, events produced by other interactions than hard collisions in the same bunch-crossing are also recorded as a signal event. These events are called "pile-up events". Figure 2.3 shows an example of an event with the high number of multiple interactions. This event has 20 reconstructed vertices. In Figure 2.4 the luminosity-weighted distribution of the mean number of interactions per crossing for 2011 is plotted. During the technical stop of LHC in September of 2011, the β^* has been reduced from 1.5m to 1.0 m. Blue curve shows the distribution before the technical stop, $\beta^* = 1.5$ m, and red curve shows that for $\beta^* = 1.0$ m. Clearly seen from the plot, the mean number of interactions per crossing is increased as the beam
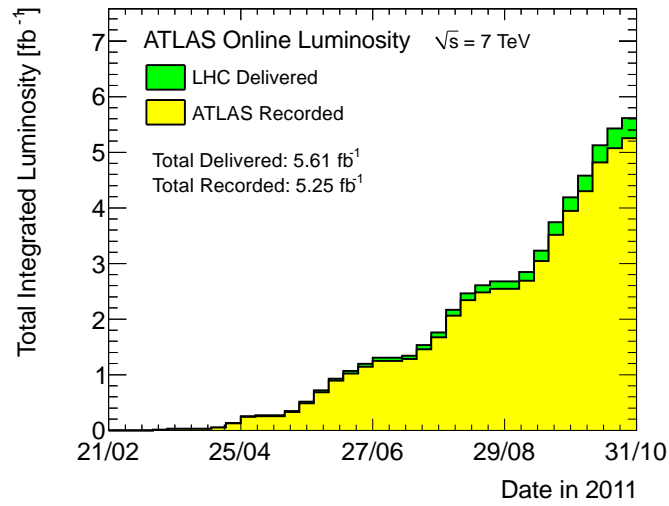
Figure 2.1: LHC integrated luminosity in 2011
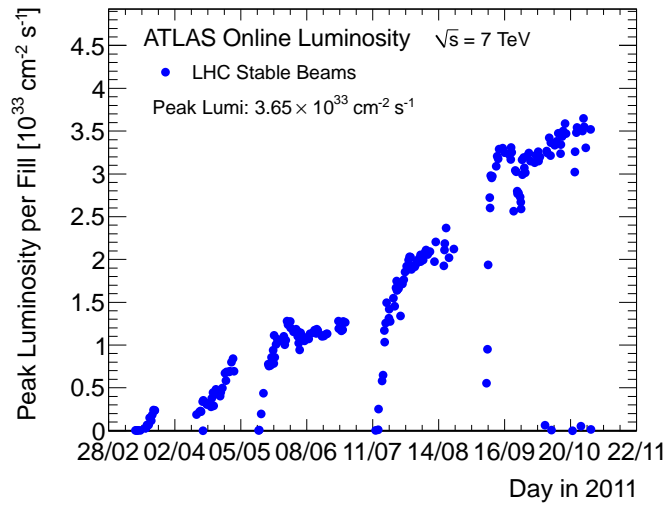
Figure 2.2: LHC peak luminosity in 2011

is squeezed more and the luminosity is increased. As the instantaneous luminosity increased, the number of interactions within the same bunch-crossing also increased.
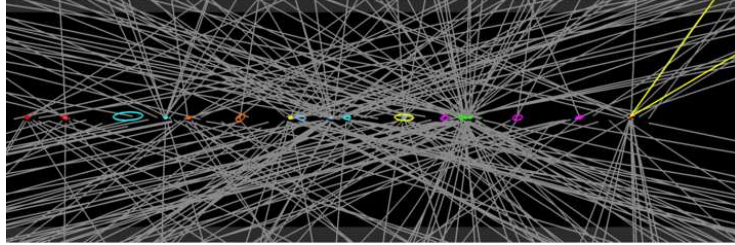
Figure 2.3: High pileup event with 20 reconstructed vertices. For this display the track transverse momentum threshold is 0.4 GeV.
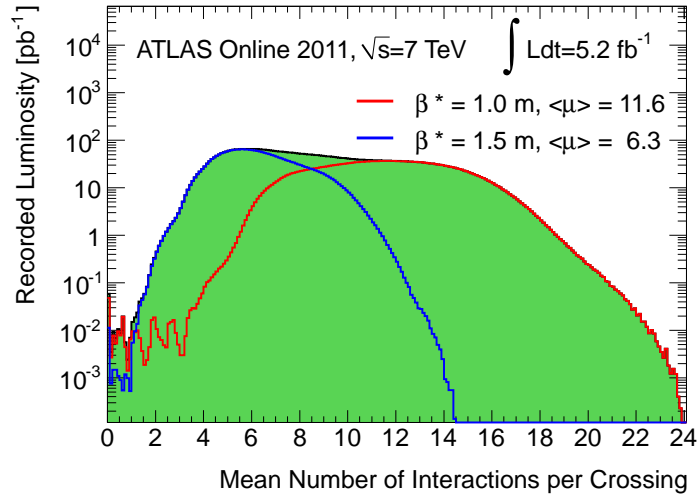
Figure 2.4: The luminosity-weighted $\langle\mu\rangle$ distribution of collision data in 2011. β^* is a characteristic of beam squeeze at the interaction point. Low β^* beam is narrower squeezed and increase the number of collisions.

The performance of the detectors are affected by such soft collision events overlapped on the triggered hard collision event. Especially, due to the relatively long integration time of the calorimeter data, the response of the calorimeter is affected not only by the same bunch crossing but also by several preceding and some following bunch crossing. The effect of such pile-up effect from out-of-time bunch crossing can be seen in Figure 2.5 indirectly. The plot shows the offset in jet transverse energy as a function of the distance from the last empty bunch crossing in the current bunch train, which measures the distance of the bunch crossing from the edge of the current bunch train. The effects of the positive in-time pile-up is canceled by the out-of-time pile-up which has an overall negative effect by signal shaping in the calorimeter data taking.

However, if the bunch crossing is near to the edge of the bunch train, there is insufficient out-of-time pile-up to cancel the in-time pile-up. The plot shows the calorimeter response becomes systematically higher near the edge of the bunch train and the effect becomes larger as the mean number of interactions increases.
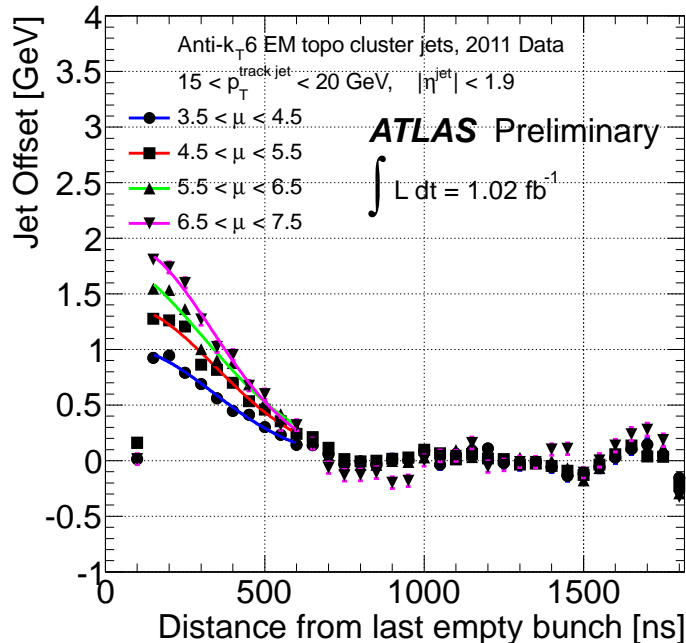
Figure 2.5: Offset in jet transverse energy $E_{T,jet}$ in data as a function of the distance from the last empty bunch (DFE) in the current bunch train

Since we analyze the lepton+jet decay channel of the top quark pair production in this analysis, the isolated high transverse momentum lepton in the final state of this channel fulfills single lepton (electron and muon) trigger conditions of the ATLAS data taking. The trigger conditions also depend on the beam conditions. While the threshold on transverse momentum of μ is constant at 18GeV during 2011, that of electron changes from 20 GeV to 22 GeV as the instantaneous luminosity increases.

2.2 Background

Selected events are contaminated with events from background processes. Figure 2.6 shows diagrams of such processes.

- W+jets

  The process of single W boson production with jets is one of the major background to the signal with lepton+jets decay channel. Leptonic decay of the W boson of this process

produces the same isolated high transverse momentum lepton and missing transverse momentum as the signal process. Background contamination from this process is estimated with the simulation sample. However, because the multi-jet production associated to W boson is not well modeled, the overall normalization of the background is determined from the measurement of the charge asymmetry of W production processes. W+jets events are estimated by using Monte Carlo simulation sample for kinematic shape and collision data for overall normalization since multi-jet production associated to W boson is not well modeled in the Monte Carlo simulation.

- QCD or non-W background

  Leptons from other than the leptonic decay of W boson is another source of background. Since QCD multi-jet production processes have a large cross section, electrons and positrons from pair productions by photons in jets and a charged lepton from semi-leptonic decaying b-quark become a large background. Additionally mis-reconstruction of the energy balance leads apparent missing transverse energy in fake lepton events. As the precise modeling is difficult for this background, the fraction of this type of background in the signal sample is estimated by using real data.

- Z+jets, di-boson and single top productions

  Other backgrounds from electroweak processes such as Z+jets, di-boson and single top production processes are estimated by simulations. Their contamination to the signal are smaller than above two background sources due to the existence of two or more isolated lepton, small missing transverse energy and low jet multiplicities.

- Other decay channels of $t\bar{t}$

  In this analysis the di-lepton decay channel of the $t\bar{t}$ production is a background to the signal and the lepton+jet decay channel with a W boson decaying into τ lepton is also a background too. Contamination from these background sources are estimated by simulations.

  Details of the estimation of background contamination are described in Chapter 7.

2.3 Simulation Samples

In order to estimate the signal efficiency and the background contamination to the signal some simulation samples are prepared for signal and background processes. All simulation samples which are used for this analysis are summarized in Table 2.1.

For the signal process, the top quark pair production process, we use two samples for the analysis. Hard collision process of one sample is generated by MC@NLO (v4.01) [19] with CT10 [8] parton distribution function (PDF). MC@NLO generates hard scattering events according to the next-to-leading-order calculation. The other sample is generated by ALPGEN [20] with CTEQ6L1 PDF [21] with top quark mass of $172.5\,\mathrm{GeV}$ for both samples. ALPGEN is based on the leading order matrix element calculations with emphasis on configurations with high jet multiplicities. Parton showers subsequent to the hard scattering process generated by the above

(a) W+jets

(b) QCD multi-jet

(c) Z+jets

(d) Di-boson

(e) Single top
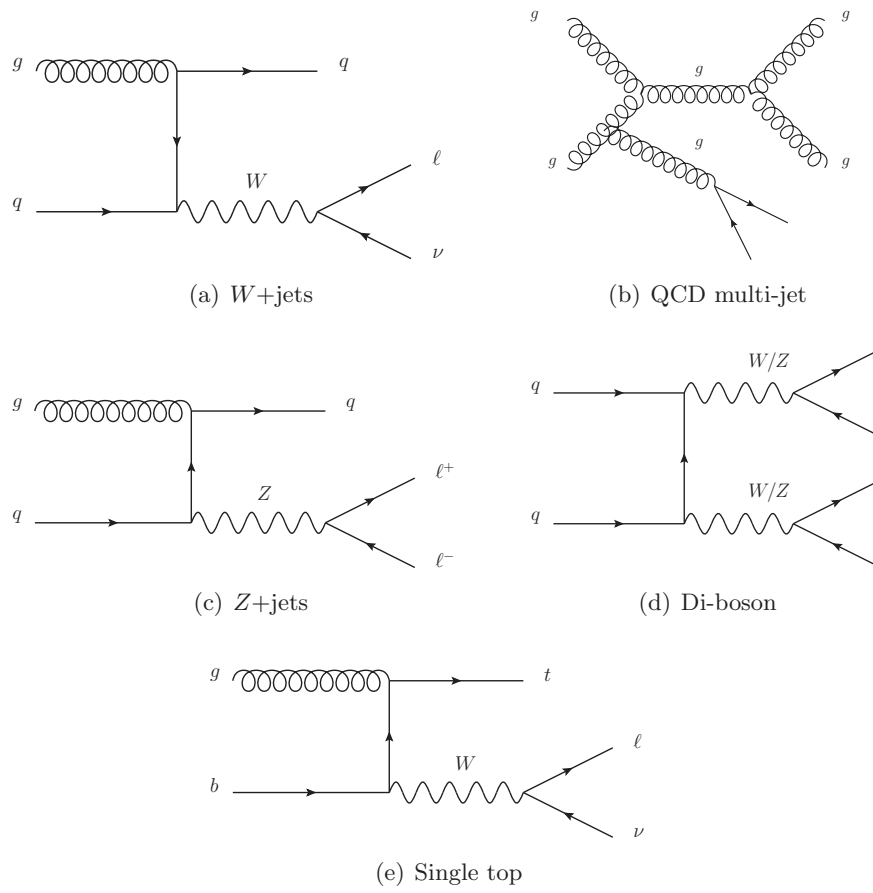
Figure 2.6: The background events for $t\bar{t}$ lepton+jets channel.

13

Table 2.1: Monte Carlo simulation samples

Process	Generator	PS and UL	PDF
$t\bar{t}$	MC@NLO	HERWIG and Jimmy	CT10
$t\bar{t}$	ALPGEN	HERWIG and Jimmy	CTEQ6L1
W/Z+jets	ALPGEN	HERWIG and Jimmy	CTEQ6L1
Single top (s-ch and Wt)	MC@NLO	HERWIG and Jimmy	CTEQ6.6
Single top (t-ch)	AcerMC	PYTHIA	MRST
Di-boson	HERWIG	HERWIG	MRST

two generators are simulated via the interface to the general-purpose generator, HERWIG [22]. For the ALPGEN sample partons after the shower simulation are matched to the partons generated by the matrix element calculations (MLM matching). ALPGEN sample offers the better modeling of the top quark pair production accompanied by multiple jets than that by MC@NLO. Hadronization of partons and particle decays are also taken care by HERWIG.

The underlying event including pile-up event under the high luminosity collisions of LHC is simulated with Jimmy (v4.31) [23] with the parameters tuned by ATLAS, AUET2 [24].

Among the background processes single top events with s-channel and Wt-channel production processes are also generated by MC@NLO with HERWIG and Jimmy. On the other hand those produced via t-channel process are generated by AcerMC [25] (LO generator) with PYTHIA [26] for parton shower, hadronization and decays. AcerMC is another generator based on the LO calculations developed for the generation of the SM background processes based on the matrix element by MadGraph/HELAS.

Background event samples for a single vector boson productions associated with multiple jet, W/Z+jets, are generated by ALPGEN interfaced to HERWIG and Jimmy with CTEL6L1 PDF functions. Background from di-boson productions (WW, WZ, ZZ) are generated by HERWIG with MRST PDFs [27]. HERWIG itself can generate various hard processes of Standard Model and some processes for new physics and generated events are interfaced to its own parton shower, hadronization and decay programs.

All Monte Carlo samples are processed with GEANT4 [28] for simulation of the ATLAS detector responses [29].

In order for the realistic simulation of pile-up events generated simulation events with pile-up are re-weighted to reproduce the $\langle\mu\rangle$ distribution of real data.

Several efficiencies for physics objects such as trigger, reconstruction and identification are derived from both collision data and Monte Carlo simulation to compare the performance between them. Correction factors so-called "scale factor (SF)" apply to Monte Carlo simulation (MC) to reproduce the efficiencies. SFs are determined:

$$SF(x) = \frac{\epsilon(x)_{\text{DATA}}}{\epsilon(x)_{\text{MC}}} \tag{2.1}$$

where x is the kinematic variables of physics objects especially η, ϕ or p_T, to take account of the dependency of the efficiency on η, ϕ and p_T.

2.4   Event Selection

Signal events of the lepton+jets decay channel of the $t\bar{t}$ pair production are selected from data according to the following procedure.

- Trigger condition

  In order to select events with an isolated charged lepton from a W boson decay efficiently, events are required to be triggered by a single charged lepton trigger at the beginning. Trigger threshold for the transverse momentum of the lepton changes depending on the beam condition. Details of triggers are described in Chapter 5.

Physics objects such as electron, muon, jet and missing transverse energy are obtained by reconstructing event data of detectors and applying identification criteria. Detailed definitions of physics objects are described in Section 4.

The following selection criteria are applied to select the signal events. In order to select events with an isolated high transverse momentum lepton from W-boson decays, they are required to have:

- an exactly one isolated charged lepton (e and μ) with high transverse momentum,

- high missing transverse energy, and

- transverse mass calculated with charged lepton and missing transverse energy that satisfies the decay condition of W-boson.

These conditions enhances events with leptonically decaying W boson and suppresses events with fake leptons. Also events with di-leptons such as Z+jets, di-boson productions and di-lepton decay channel of $t\bar{t}$ productions are suppressed.

In order to improve the S/N ratio of the signal, events are required to have:

- at least four jets, and

- at least one b-tagged jet.

These conditions suppress background events from W+jets and single top productions. Details of the selection conditions are described in Chapter 5.

2.5 $t\bar{t}$ event Reconstruction

In order to obtain the kinematic variables of the $t\bar{t}$ system, such as $m_{t\bar{t}}$ and $y_{t\bar{t}}$ the likelihood fit is applied to the objects in the final state of the selected events. In the likelihood the probabilities of produced particles, a charged lepton, a neutrino and quarks, having observed energies of a lepton, missing transverse energy and jets, are included as a transfer function of the energy of produced particles and that of observed objects. The invariant masses of decay products of top, anti-top and W bosons are also taken into account as a shape of Breit-Wigner functions to the likelihood. By maximizing the likelihood value, the kinematics of the $t\bar{t}$ system is reconstructed

from observed objects and the variables, $m_{t\bar{t}}$ and $y_{t\bar{t}}$ for which we measure the differential cross sections, are calculated.

Differential cross sections, σ_i, are calculated by the following formula:

$$\sigma_j = \frac{\Sigma_i M_{ij}^{-1}[N_i^{\text{signal}} - N_i^{\text{BG}}]}{\epsilon_j \mathcal{L}} \tag{2.2}$$

where N_i^{signal} is the number of observed signal events in the i-th bin of the variable, N_i^{signal} is the number of estimated background events in the same bin, ϵ_j is the efficiency for the event of which truth variable falls in the j-th bin, $\mathcal{L}$ is the integrated luminosity and M_{ij}^{-1} is the inverted migration matrix. The migration matrix, which expresses the relation between true and measured values of the variable, is estimated by comparing truth information with measured value using simulated events. In order to obtain the inverted matrix the "Unfolding" technique is adopted. By correcting with the detector efficiencies and the integrated luminosity, the differential cross sections are obtained.

The details of the reconstruction of the kinematics is described in Chapter 6, and that of the method of obtaining the differential cross section is described in Chapter 9.

However to extract true level differential cross section to compare the theoretical predictions and other experimental results, reconstructed $m_{t\bar{t}}$ and $y_{t\bar{t}}$ are transformed to parton level distribution by "Unfolding Technique". The details of this conceptual eq. (2.2) and unfolding technique are explained at Chapter 9.

From the distributions of these variables, the differential cross sections are calculated using the "Unfolding" technique. The distributions of reconstructed variables are corrected with an reversed migration matrix via "Unfolding" technique and are transformed to those of generated variables.

Chapter 3

Accelerator and Detector

The Large Hadron Collider (LHC) is the largest and highest-energy hadron collider among the facilities for high energy physics that are currently in operation. The LHC beam parameters are summarized in Table 3.1. It is a two-ring, superconducting accelerator located at CERN (Geneva, Switzerland), and installed in the 27 km long former LEP tunnel, aiming the discovery of the Higgs boson and the search for new physics beyond the standard model. The LHC was operated at center of mass energy of 7 TeV in 2011, 8 TeV in 2012 with 50 nsec beam crossing and will be operated at 14 TeV with 25 nsec beam crossing. This analysis used the data of the LHC in 2011 The designed value of the peak luminosity is 10^{34} cm^{-2}s^{-1} and the highest peak luminosity in the 2011 operation was 3.65×10^{33} cm^{-2}s^{-1} as shown in Figure 2.2. The delivered integrated luminosity to the ATLAS detector was 5.61 fb^{-1} in 2011 (Figure 2.1). The accelerator complex is shown in Figure 3.1. Protons are supplied to Large Hadron Collider(LHC) from the injector chain: Linac2 (50 MeV) - Proton Synchrotron Booster (PSB, 1.4 GeV) - Proton Synchrotron (PS, 25 GeV) - Super Proton Synchrotron (SPS, 450 GeV). The Linac2 duoplasmatron is the source of protons for the CERN accelerator complex. For the ionization of hydrogen, i.e. production of protons, the electron bombardment ionization is a simple process [30]:

$$
\begin{aligned}
H_2 + e &\Rightarrow H_2^+ + 2e \\
H_2^+ + e &\Rightarrow H^+ + H + e \\
H + e &\Rightarrow H^+ + 2e \\
H_2^+ + H_2 &\Rightarrow H_3^+ + H \\
H_3^+ + e &\Rightarrow H^+ + H_2 + e
\end{aligned}
\tag{3.1}
$$
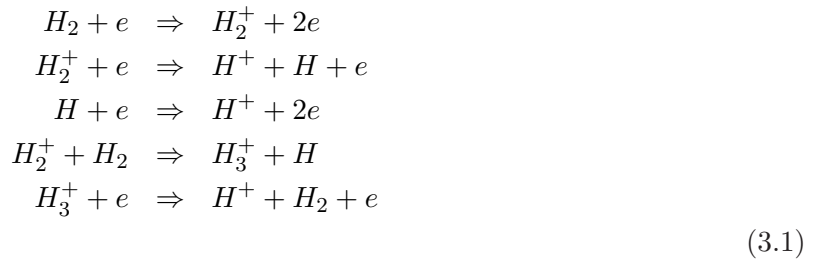
The last two processes are important for the efficient protons production.

3.1 The ATLAS Detector

The ATLAS detector is a general purpose particle detector and consists of the following four major parts: the Inner Detector, the calorimeters, the Muon Spectrometer and the magnet systems as shown in Figure 3.2.

Table 3.1: LHC beam parameters for design and in 2011.

Parameters	Design	2011
Ring circumference	26658.883 m	
Proton energy	7000 GeV	3500 GeV
Peak luminosity	1.0×10^{34}	3.65×10^{33}
Bunch spacing	25 ns	50 ns
Number of bunches	2808	1380
Number of protons per bunch	1.15×10^{11}	1.25×10^{11}
Beam emittance	3.75 μm	2.9 μm
Number of main bends	1232	
Length of main bends	14.3 m	
Field of main bends	8.33 T	4.16 T
RMS bunch length	7.55 cm	8.7 cm
RMS beam size	16.7 μm	34 μm
Half crossing angle	±142.5 μrad	120 μrad
Plane of crossing	vertical (ATLAS)	
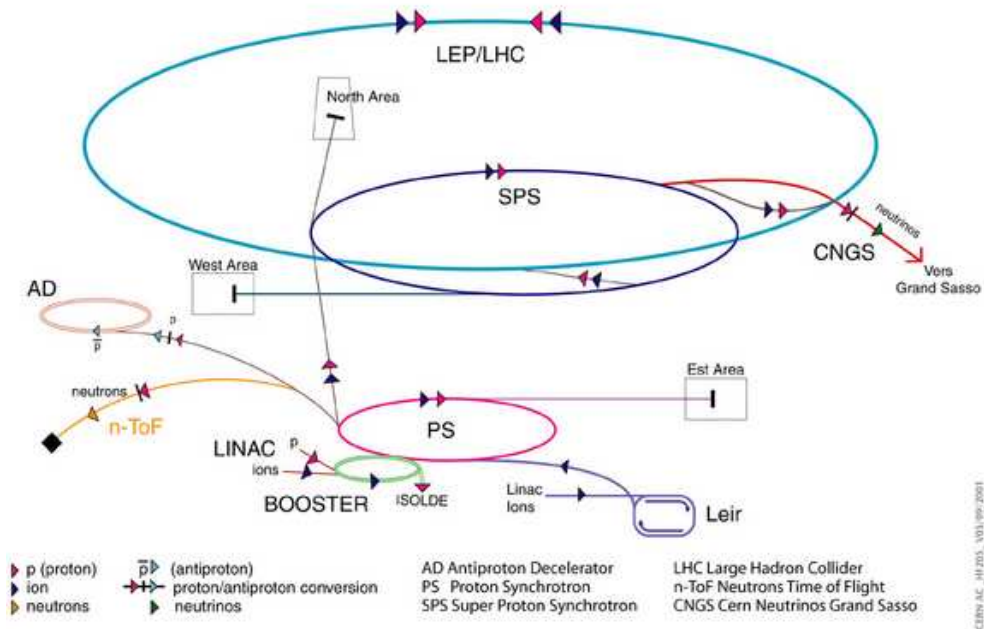
Figure 3.1: LHC accelerator complex
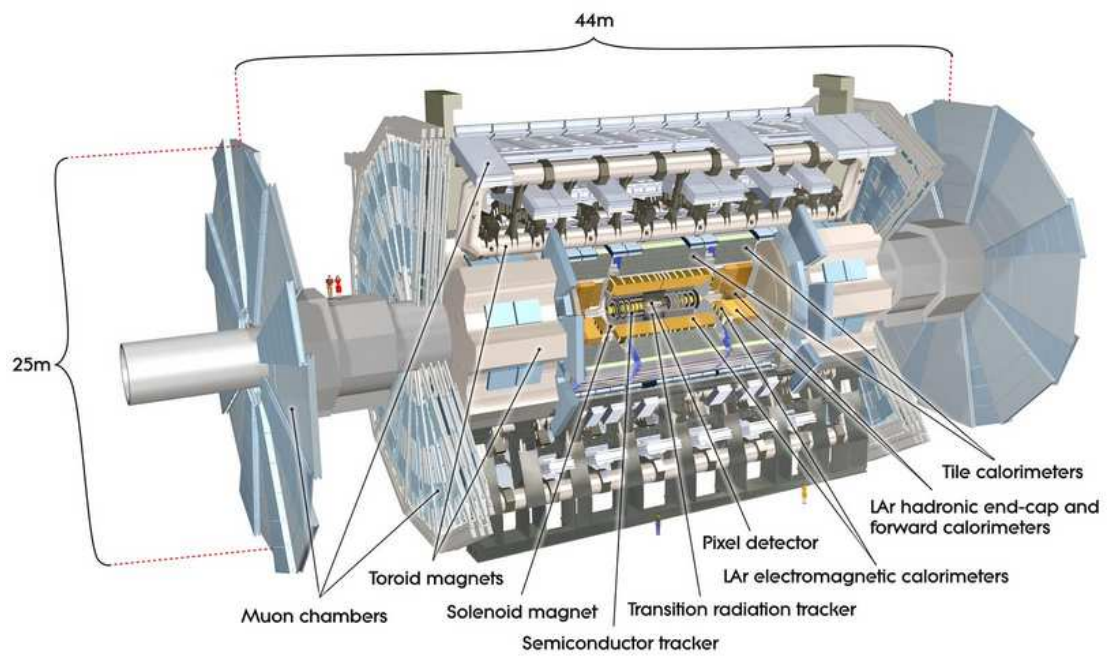
Figure 3.2: ATLAS detector

3.2 Inner Detector

Inner Detector is located at the innermost part of the ATLAS detector. It is designed to detect tracks of charged particles and measure momenta, impact parameters and vertex positions. The Inner Detector system is consists of three sub-detector systems. They are pixel detector (PIXEL) , semiconductor tracker (SCT) and transition radiation tracker (TRT) from the inside of the detector to the outside. Inner two sub-systems: PIXEL and SCT utilize, are semiconductor tracking detectors and provide high-precision measurements of track momenta and vertex with their fine-granularity. On the other hand TRT offers a large number of tracking points with higher average radius. The combination of two types of sub-detector systems gives robust pattern recognition and high precision in both ϕ and z coordinates. The layout of the Inner Detector system is shown in Figure 3.3. It offers full tracking coverage over $|\eta| < 2.5$. All detectors contained in the central solenoid system which provides a nominal magnetic field of 2 T. Parameters of the Inner Detector are also shown in Table 3.2 [31].
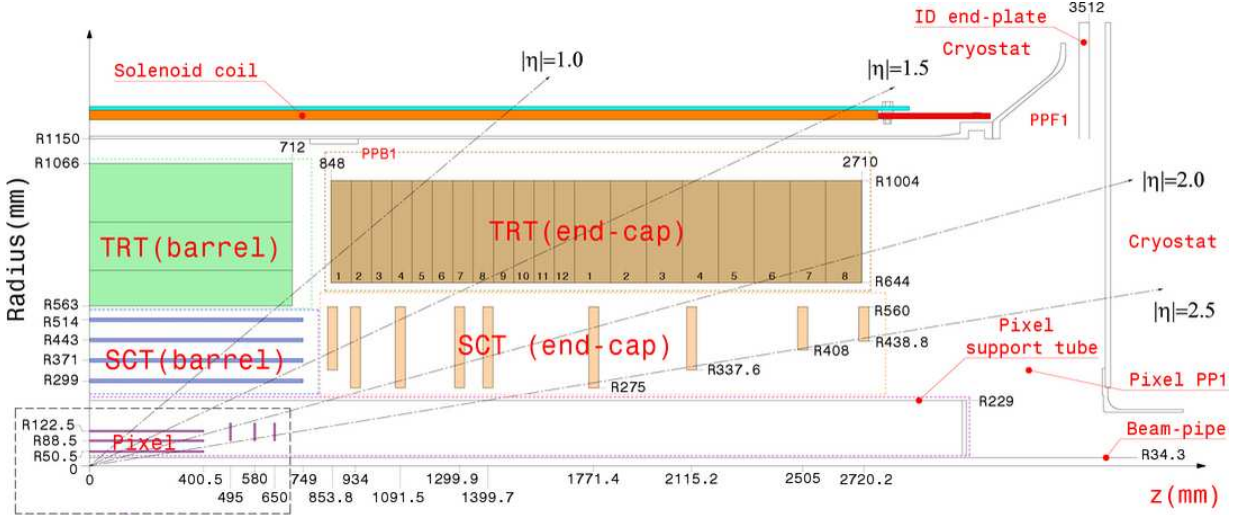
Figure 3.3: Inner Detector

3.2.1 PIXEL detector (PIXEL)

The pixel detector consists of three barrel layers at radii of 4 cm, 10 cm and 13 cm, and five disks perpendicular to the beam axis on each side between radii of 11 and 20 cm. It provides three precision measurements over the full acceptance and contains 140 million detector elements, each 50 μm in $r - \phi$ and 300 μm in z. The pixel modules for the barrel and the end-cap disks are designed to be identical. Each module is 62.4 mm long and 21.4 mm wide with 46080 pixels of 50×400 μm. Thickness of each layer is 280 μm and about 1.7% of a radiation length at normal incidence.

Table 3.2: Parameters of Inner Detector

System	Position	Resolution σ (μm)	η coverage (10^6)
Pixels	1 removable barrel layer	$R\phi = 12$, $z = 66$	± 2.5
	2 barrel layers	$R\phi = 12$, $z = 66$	± 1.7
	5 end-cap disks	$R\phi = 12$, $R = 77$	1.7-2.5
	on each side		
Silicon strips	4 barrel layers	$R\phi = 16$, $z = 580$	± 1.4
	9 end-cap wheels	$R\phi = 16$, $R = 580$	1.4-2.5
	on each side		
TRT	Axial barrel straws	170 (per straw)	± 0.7
	Radial end-cap straws	170 (per straw)	0.7-2.5
	36 straws per track		

3.2.2 Semiconductor Tracker (SCT)

The SCT detector is located outside of the PIXEL and offers high-precision measurements in the intermediate radial range and designed to provide eight precision measurements per track. The barrel part has eight layers of silicon microstrip detectors. One silicon detector module consists of four silicon microstrip detectors. Each silicon detector is 6.36×6.40 cm^2 with 768 readout strips of 80 μm pitch two detectors are wire-bonded together to form a pair and two pairs are glued back to back at 40 mrad angle. The end-cap modules are similar but use tapered strips, with one set aligned radially. The barrel modules form four layers at radii of 30.0, 37.3, 44.7 and 52.0 cm and the end-cap modules are mounted in up to three rings onto nine wheels. The radial range of each end-cap disk is adopted to the η coverage to $|\eta| < 2.5$.

3.2.3 Transition Radiation Tracker (TRT)

The TRT consists of straw detectors with small diameter, which can operate under the very high collision rate of the LHC. Electron identification can be possible due to transition radiation photons created in a radiator between the straws. Each straw is 4 mm in diameter and 144 cm length at maximum in the barrel. The barrel consists of about 50000 straws and the end-caps consists of 320000 radial straws. The spacial resolution per straw is 17 μm. In order to detect transition radiation photons signal of straws can be read with two independent thresholds. The barrel section covers pseudo rapidity region $|\eta| < 0.7$ and the radial range from 56 to 107 cm, and the two end-caps cover $|\eta| < 2.5$ and the radial range from 64 to 103 cm.

3.2.4 Tracking

The ATLAS inner detector tracking is performed following three stages.

1. The hits of the PIXEL and the SCT detectors are converted into clusters. After that space-points on the SCT are formed from the cluster information of behind SCT module using stereo angle. the TRT raw timing information is translated into calibrated drift circles.

2. The track seeds are formed using space-points of the three PIXEL and the first SCT layer. These seeds are extended throughout the SCT to form track candidates. The candidates tracks are then extended into the TRT to associate drift-circle in a road around the extrapolation. Finally the extended tracks are refitted with the full information of all inner detectors.

3. After this track fitting the primary vertices are reconstructed followed by the reconstruction of photon conversions and of secondary vertices.

The momentum resolution of Inner Detector is $\sigma_{p_\mathrm{T}/p} \sim 0.05\% p_\mathrm{T} \oplus 1\%$.

3.3 Calorimeters

A view of the ATLAS calorimeters is shown in Figure 3.4 [32]. The calorimetry consists of an electromagnetic (EM) calorimeter covering the pseudo rapidity region $|\eta| < 3.2$, a hadronic barrel calorimeter covering $|\eta| < 1.7$, hadronic end-cap calorimeters covering $1.5 < |\eta| < 3.2$, and forward calorimeters covering $3.1 < |\eta| < 4.9$.
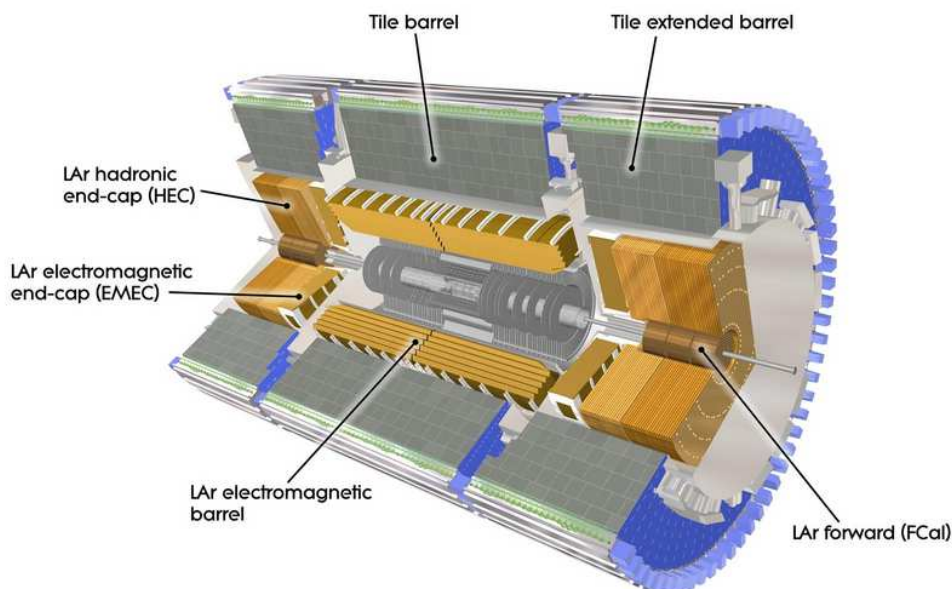
Figure 3.4: Calorimeters layout

3.3.1 Electromagnetic Calorimeter

The EM calorimeter is a lead LAr detector with accordion-shaped Kapton electrodes and lead absorber plates over its full coverage. The accordion geometry provides complete ϕ symmetry without azimuthal cracks. The total thickness of the EM calorimeter is > 24 radiation lengths (X_0) in the barrel and $> 26\ X_0$ in the end-caps. Over the region devoted to precision physics $(|\eta| < 2.5)$, the EM calorimeter is segmented into three longitudinal sections. The strip section, which has a constant thickness of $\sim 6\ X_0$ as a function of η, is equipped with narrow strips with a pitch of ~ 4 mm in the η direction. This section acts as a 'preshower' detector, enhancing particle identification (γ/π^0, e/π separation etc.) and providing a precise position measurement in η. The middle section is transversely segmented into square towers of size $\Delta\eta \times \Delta\phi = 0.025 \times 0.025$. The total calorimeter thickness up to the end of the second section is $\sim 24\ X_0$, tapered with increasing rapidity. The back section has a granularity of 0.05 in η and a thickness varying between $2\ X_0$ and $12\ X_0$.

The electromagnetic calorimeter has the energy resolution of $\sigma_E/E \sim 10\%/\sqrt{E} \oplus 0.7\%$.

3.3.2 Hadronic Calorimeter

The ATLAS hadronic calorimeters cover the range $|\eta| < 4.9$ using different techniques for the widely varying requirements and radiation environment over the large η range. Over the range $|\eta| < 1.7$, the iron scintillating-tile technique is used for the barrel and extended barrel tile calorimeters. Over the range $\sim 1.5 < |\eta| < 4.9$, LAr calorimeters were chose: the hadronic end-cap calorimeter (HEC) extends to $|\eta| < 3.2$, while the range $3.1 < |\eta| < 4.9$ is covered by the high-density forward calorimeter (FCAL). The total thickness is 11 interaction lengths (λ) at $\eta = 0$, including about 1.5 λ from the outer support.

The hadronic calorimeter offers the energy resolution of $\sigma_E/E \sim 50\%/\sqrt{E} \oplus 3\%$.

3.4 Muon Spectrometer
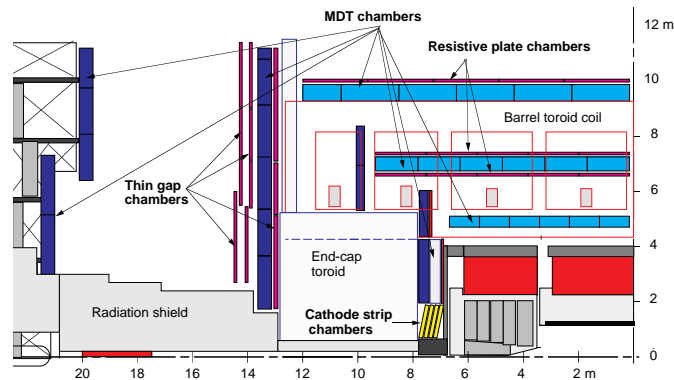
Figure 3.5: Muon Spectrometer layout

Layout of the muon spectrometer is shown in Figure 3.5 [32]. It is based on the magnetic deflection of muon tracks in the large superconducting air-core toroid magnets, instrumented with trigger and high-precision tracking chambers separately. Over the range $|\eta| \leq 1.0$, magnetic bending is provided by the large barrel toroid. For $1.4 \leq |\eta| \leq 2.7$, muon tracks are bent by two smaller end-cap magnets inserted into both ends of the barrel toroid. Over $1.0 \leq |\eta| \leq 1.4$, usually referred to as the transition region, magnetic deflection is provided by a combination of barrel and end-cap fields. In the barrel region, tracks are measured in chambers arranged in three cylindrical layers ('stations') around the beam axis; in the transition and end-cap regions, the chambers are installed vertically, also in three stations.

3.4.1 Monitored Drift Tube Chambers (MDT)

A precision measurement of the track coordinates for most of the η range is provided by Monitored Drift Tubes (MDTs). The MDT chambers are aluminum tubes of 30 mm diameter and 400 μm wall thickness, with a 50 μm diameter central W-Re wire. The tubes are operated with a mixture of 93% Ar and 7% CO_2 and have a total volume of 800 m^3. The MDTs has a single-wire resolution of $\sim 80\mu$m with high gas pressure (3 bar).

3.4.2 Cathode Strip Chambers (CSC)

Cathode Strip Chambers (CSCs) are used in the innermost plane close to the interaction point over $2 < |\eta| < 2.7$. The CSCs are multiwire proportional chambers with cathode strip readout and with a symmetric cell in which the anode-cathode spacing is equal to the anode wire pitch. The cathode strips (5.08 mm pitch) are orthogonal to the anode wires (2.54 mm pitch). The baseline gas is a mixture of 30% Ar, 50% CO_2 and 20% CF_4 with total volume of 1.1 m^3. Measuring the charge induced on the segmented cathode by the avalanche formed on the anode wire provide precision coordinate. The position resolutions is ~ 60 μm. The muon momentum resolution is 2.5% at 100 GeV.

3.4.3 Resistive Plate Chamber (RPC)

The trigger system, Resistive Plate Chambers and Thin Gap Chamber, covers the pseudo rapidity range $|\eta| \leq 2.4$. Resistive Plate Chambers (RPCs) are used in the barrel region ($|\eta| < 1.05$). The RPC is a gaseous detector providing a typical space-time resolution of 1 cm $\times$ 1 ns. The basic RPC unit is a narrow gas gap formed by 2 mm thickness of two parallel resistive Bakelite plates, separated by insulating spacers. The gas mixture is based on $C_2H_2F_4$ with small admixture of SF_6.

3.4.4 Thin gap chamber (TGC)

Thin Gap Chambers (TGCs) is also used for the trigger system of the end-cap regions ($1.05 < |\eta| < 2.4$). The TGCs are similar design to multiwire proportional chambers with the difference that the anode wire pitch is larger than the cathode-anode distance. The dimension of TGCs is cathode-cathode distance of 2.8 mm and a wire pitch of 1.8 mm. A highly quenching gas mixture of 55% CO_2 and 45% $n - C_5H_{12}$ is encapsulated with total volume of 16m^3. Signals from the

anode wires, arranged parallel to the MDT wires, provide the trigger information together with readout strips arranged orthogonal to the wire.

3.5 Magnet System

The ATLAS superconducting magnet system is shown in Figure 3.2 [32]. A central solenoid (CS) is providing magnetic filed for the Inner Detector, surrounded by a system of three large air-core toroids generating the magnetic field for the muon spectrometer. The two end-cap toroids (ECT) are inserted in the barrel toroid (BT) at each end and line up with the CS. The CS provides a central field of 2 T with a peak magnetic field of 2.6 T at the superconductor itself. The peak magnetic fields on the superconductors in the BT and ECT are 3.9 and 4.1 T respectively. The performance of bending power is characterized by the field integral $\int Bdl$ where B is the azimuthal field component and the integral is taken on a straight line trajectory between the inner and outer radius of the toroids. The BT provides 2 to 6 Tm and the ECT contributes with 4 to 8 Tm in the range of $0.0 < |\eta| < 1.3$ and $1.6 < |\eta| < -2.7$.

3.6 Trigger and data-acquisition system

The ATLAS trigger and data-acquisition system (DAQ) is based on three levels of online event selection. Each trigger level refines the decisions made at the previous level and, where necessary, applies additional selection criteria. Starting from an initial bunch-crossing rate of 40 MHz, the rate of selected events must be reduced to ∼100 Hz for permanent storage. A simplified functional view of the Trigger/DAQ system is shown in Figure 3.6 [31].

Events selected by L1 are read out from the front-end electronics systems of the detectors into readout drives (RODs) and then into readout buffers (ROBs). Inter mediate buffers , 'de-randomisers', average the rate of acquired data at the output of the pipeline memories for the available input band width of the RODs. In the ROBS, all the detector data selected by the L1 trigger are kept until L2 trigger decision. The event is accepted by L2, the data is transferred by the DAQ system to Event Filter and this process is called event building. Each event that is constructed with many fragments in each ROBs are stored in a single memory by event building.

3.6.1 Level-1

An initial selection performs at the level-1 (L1) based on reduced-granularity information from detector subsystem. High transverse-momentum (high-p_T) muons are identified using only the trigger chambers (TGCs and RPCs). The calorimeter cluster selections are based on information from all the calorimeters (EM and hadronic). Objects search of the calorimeter trigger are for high-p_T electrons, photons, jets, and τ leptons decaying into hadrons as well as large missing and total transverse energies. Trigger information is provided for a number of sets of p_T thresholds.

3.6.2 Level-2

The level-2 trigger (L2) use 'region-of-interest' (RoI) defined by the L1 position information. This includes information of the position (η and ϕ) and p_T of candidate objects and energy sums.
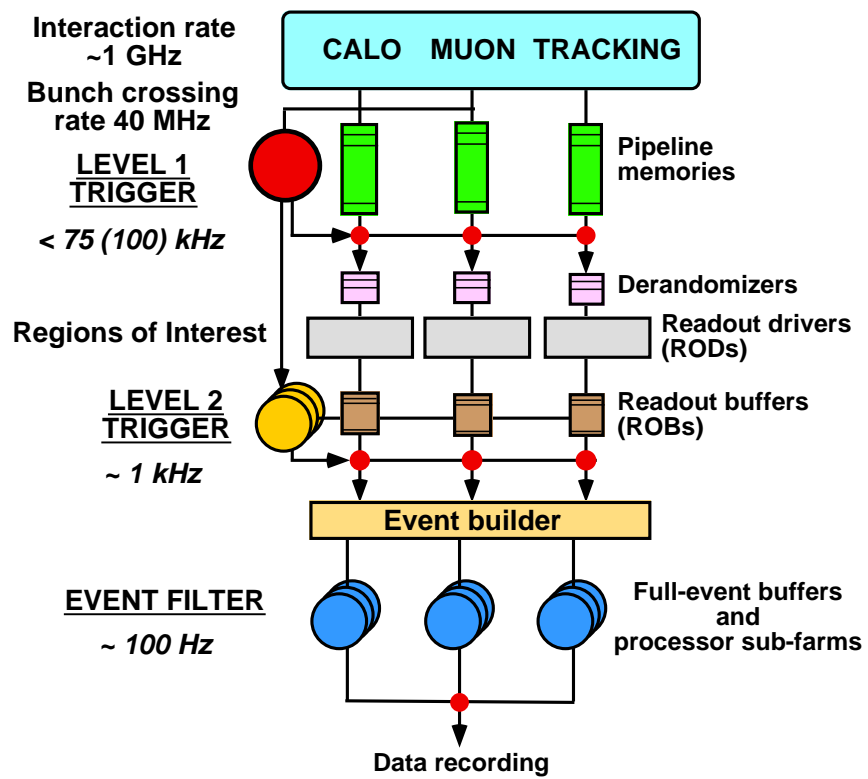
Figure 3.6: Block diagram of the Trigger/DAQ system

The RoI data are sent from L1 to L2 for all events selected by the L1 trigger. Using the RoI information, the L2 trigger accesses data selectively from the ROBs. The L2 trigger access to all of the event data if necessary with the full precision and granularity.

3.6.3   Event Filter

The last stage of the online selection is performed by the Event Filter (EF). It employ offline algorithms and methods that are adapted to the online environment, and use the latest calibration and alignment information and the magnetic field map. The EF makes the final selection of physics events which is written to mass storage for subsequent full offline analysis. The output rate from L2 should be reduced to $\sim$100 Hz, corresponding to an output data rate of $\sim$100 MB/s if the full event data are to be recorded.

Chapter 4

Analysis Objects Reconstruction and Identification

Physics objects, such as electron, muon, jet, b-jet and missing transverse energy, which are used in the selection and analysis of the $t\bar{t}$ events are defined from detector signals through the reconstruction and identification procedures. Their scales, energy and momentum, are determined by applying corrections which are derived from simulations, test beam results and collision data.

4.1 Signal of Physics Objects

Physics objects are reconstructed and identified from the detector signals produced by particles from beam collisions through interactions with detector materials. Figure 4.1 shows how particles interact in the ATLAS detector. Charged particles leave hits in the Inner Detector by the ionization of detector materials and their tracks are reconstructed from these hits. Electrons and photons generate electromagnetic showers in the EM calorimeter and produce large signals in the calorimeter. On the other hand muons do not produce electromagnetic showers due to its larger mass than electrons, penetrate through calorimeter materials and leave hits in the muon spectrometers installed at the outermost part of the detector system. These hits can be used to reconstruct muon tracks and to identify muon objects. Quarks are observed as jets of hadrons due to the confinement nature of QCD. They produce track hits in the inner detector as well as shower signals both in the electromagnetic and hadronic calorimeters.

4.2 Electron

4.2.1 Electron Reconstruction

Electron reconstruction starts from energy deposits (clusters) in the EM calorimeter. To reconstruct the EM clusters, seed clusters of longitudinal towers with total transverse energy above 2.5 GeV are searched with the window of 3×5 longitudinal towers for central region ($|\eta| < 2.47$) in units of 0.025×0.025 in $\eta \times \phi$ space corresponding to the granularity of the calorimeter middle layer (Layer 2) shown in Figure 4.2. In the inner detector, reconstructed tracks are extrapolated
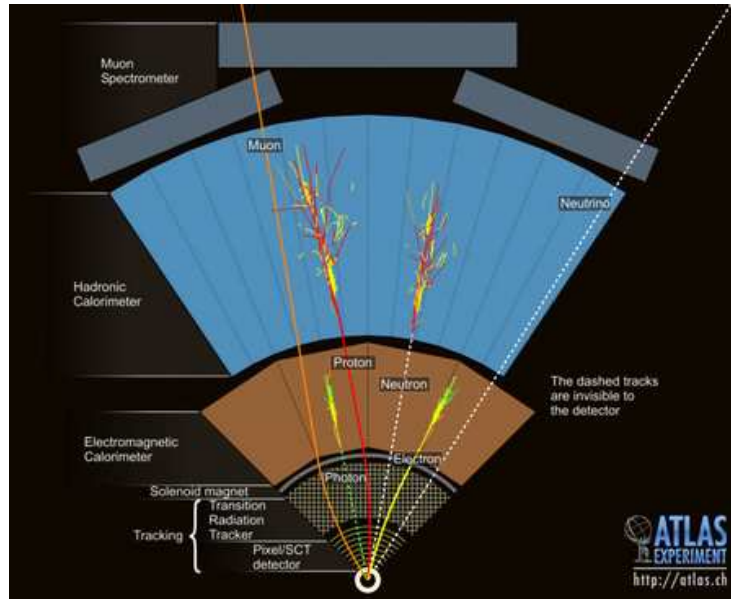
Figure 4.1: How the particles interacts in the ATLAS detector.

Figure 4.2: Longitudinal and transverse segmentation of the LAr EM calorimeter in the central region.

from their last measurement point to the middle layer of the EM calorimeter that are very loosely matched to the seed clusters. The distance between the track and the cluster position is required to satisfy $\Delta\eta < 0.05$. It is reconstructed as electron if at least one track is matched to the seed cluster. In case that several tracks are matched to the same cluster, required to have hits on the silicon detector and the smallest ΔR distance to the seed cluster is chosen.

The electron cluster is rebuilt 3×7 longitudinal towers and the determined the energy by summing four different contributions: (1)the estimated energy deposit in the material in front of the EM calorimeter, (2) the measured energy deposit in the cluster, (3) the estimated external energy deposit outside the cluster (lateral leakage), (4) the estimated energy deposit beyond the EM calorimeter (longitudinal leakage). The four momentum is computed using information from both the final cluster and the best track matched to the original seed cluster. The energy is given by the cluster energy and the directions are taken from the track.

4.2.1.1 Reconstruction Efficiency

Electron reconstruction efficiency are also studied using $Z \to ee$ *Tag & Probe* method described Section 5.1.1.3. The reconstruction efficiency is defined with the electron track reconstruction and track-cluster matching efficiencies. The prove electron having $E_{\mathrm{T}} = 15 - 50$ GeV and satisfying the track quality requirement of hits on silicon detector, $N_{\mathrm{PIXEL}} \geq 1$ and $N_{\mathrm{PIXEL}} + N_{\mathrm{SCT}} \geq 7$ is considered. The reconstruction efficiency SF is also shown in Figure 4.3.
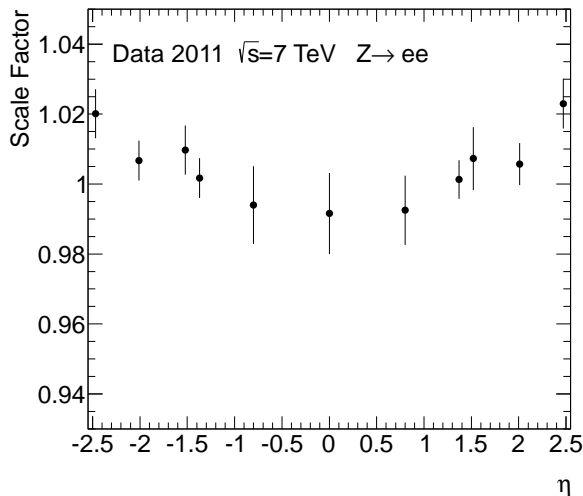
Figure 4.3: Reconstruction efficiency SF measured from $Z \to ee$ *Tag & Probe* method.

4.2.2 Electron Identification

In the standard reconstruction of electrons, a seed electromagnetic tower with transverse energy above ~ 3 GeV is taken from the EM calorimeter and a matching track is searched for all re-

constructed tracks which do not belong to a photon-conversion pair reconstructed in the inner detector. A charged track after extrapolation to the EM calorimeter is required to match the seed cluster within a window of $\Delta\eta \times \Delta\phi = 0.05 \times 0.10$. The ratio, E/p, of the energy of the cluster to the momentum of the track is required to be lower than 10. Various identification techniques are applied to the reconstructed electron candidates, combining calorimeter and track quantities and the TRT information to discriminate jets and background electrons from the signal electrons. A simple cut-based identification procedure is described in Table 4.1 [31]. Tight electrons are required for this analysis.

Table 4.1: Definition for loose, medium and tight electron identification cuts. The cut values are given explicitly only when they are independent of η and p_{T}.

Type	Description
	Loose cuts
Acceptance of the detector	$|\eta| < 2.47$
Hadronic leakage	Ratio of E_{T} in the first sampling of the
	hadronic calorimeter to E_{T} of the EM cluster.
Second layer	Ratio in η of cell energies in 3×7 versus 7×7 cells.
of EM calorimeter	Ratio in ϕ of cell energies in 3×3 versus 3×7 cells.
	Lateral width of the shower.
	Medium cuts (includes loose cuts)
First layer	Ratio of the energy difference between the largest and second largest
of EM calorimeter	energy deposits in the cluster over the sum of these energies.
	Total lateral shower width (20 strips).
Track quality	Number of hits in the pixel detector (at least two hits,
	in the pixel layers, one of the hits in the b-layer).
	Number of hits in the pixels and SCT (at least nine).
	Transverse impact parameter (< 1 mm).
	$\Delta\eta$ between the cluster and the track < 0.01.
	Tight cuts (includes medium cuts)
Track matching	$\Delta\eta$ between the cluster and the track < 0.005.
	$\Delta\phi$ between the cluster and the track < 0.02.
	Ratio of the cluster energy to the track momentum (E/p).
TRT	Total number of hits in the TRT.
	Ratio of the number of high-threshold
	hits to the total number of hits in the TRT.

Additional quality cuts are applied to the tight electron at the offline selection. Electrons are required to have $|\eta_{\mathrm{cl}}| < 2.47$, excluding the transition region of $1.37 < |\eta_{\mathrm{cl}}| < 1.52$ and transverse energy $E_{\mathrm{T}} > 25\,\mathrm{GeV}$ ($E_{\mathrm{T}} = E_{\mathrm{cl}}/\cosh(\eta_{\mathrm{track}})$). To suppress fake lepton background further, tight isolation cuts are imposed on electrons with cone size of $\Delta R = 0.2$ and $\Delta R = 0.3$ for calorimeter and track isolation, respectively. They are corrected for energy leakage into the isolation cone

and for additional energy deposit from pile-up events. For this analysis, the combination of 90% for calorimeter isolation of $\Delta R = 0.2$ and 90% for track isolation of $\Delta R = 0.3$ to suppress fake lepton background and enhance signal lepton effectively. Jets within a cone with $\Delta R = 0.2$ from the electron direction are removed from the event. After this jet-electron overlap removal, if still another jet with $p_T > 20\,\text{GeV}$ is found within cone $\Delta R = 0.4$, the electron is discarded. In addition electrons with $p_T > 15\,\text{GeV}$ are also used for the overlap removal and additional lepton veto. This additional electron definition reduces di-lepton events such as $t\bar{t}$ di-lepton channel, Z boson decaying into two electrons and di-boson events.

4.2.2.1 Electron Identification Efficiency

Electron identification efficiencies including additional quality cuts are derived from the combined measurements using $Z \to ee$ and $W \to e\nu$ samples with *Tag & Probe* method. The isolation cut efficiencies with respect to tight selection are also derived using $Z \to ee$ sample. The dependencies of the isolation cut efficiencies are evaluated with $Z \to ee$, $W \to e\nu$ and top samples shown in Figure 4.5. The systematic uncertainties of isolation cut efficiencies are effects of pileup (1.0%), underlying events ($< 1.0\%$) and difference between top and W/Z electrons.

(a)   (b)
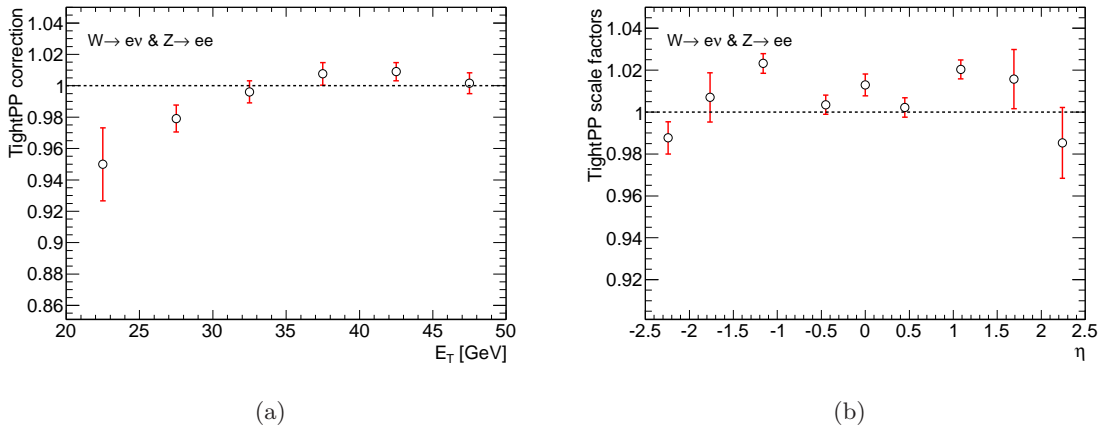
Figure 4.4: Electron identification (tight) efficiency SF.

4.2.3 Electron Energy Resolution and Scale

The electron energy scales are obtained from $Z \to ee$, $J/\Psi \to ee$ and $W \to e\nu$. The energy scale is corrected in data as a function of the electron cluster η, ϕ and E_T and systematic uncertainties are within $\pm(1\text{-}1.5)\%$ for the $|\eta| < 2.47$ region dominated by uncertainties from the detector material and the presampler energy scale. The electron energy resolution determined by calibrated $Z \to ee$ are shown in Figure 4.6. The mass peak resolution are:

- for all candidates in data (MC) 1.76 ± 0.01 GeV (1.59 ± 0.01 GeV)
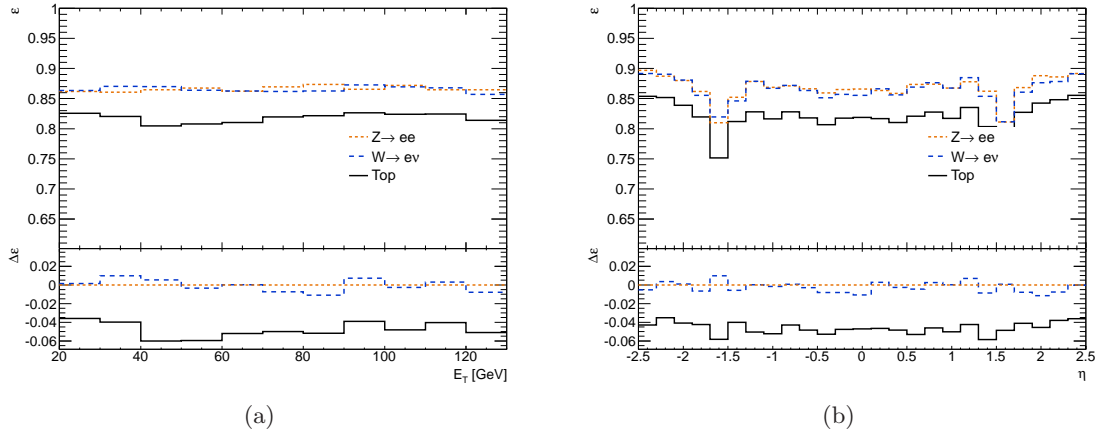
Figure 4.5: Electron isolation cut (for tight) efficiency as a function of E_T and η.

- for pairs with $|\eta| < 1.37$ in data (MC) 1.60 ± 0.01 GeV (1.45 ± 0.01 GeV)

- for pairs with $|\eta| > 1.52$ in data (MC) 1.99 ± 0.02 GeV (1.68 ± 0.01 GeV)
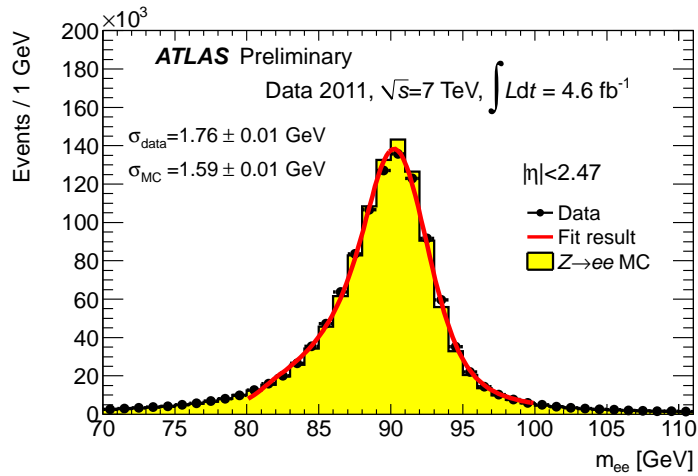
Figure 4.6: Calibrated $Z \rightarrow ee$ invariant mass for all pairs.

4.3 Muon

4.3.1 Muon Reconstruction

The muon object used in this analysis is obtained by combining muon tracks locally reconstructed in the muon spectrometer and charged particle tracks reconstructed in the inner detector. The reconstruction algorithm extrapolates muon tracks in the muon spectrometer back to the beam line and matches them to inner detector tracks by using a χ^2 defined by parameter differences between muon track segments and ID tracks and summed covariance.

A muon trajectory reconstructed in the muon spectrometer is called "Standalone Muon". The algorithm for the "Standalone Muon" builds track segments in each three muon station and combines them as standalone muon tracks. The track parameter of the standalone muon is defined at the first measured point inside the muon spectrometer. The momentum measured in muon spectrometer is corrected with the parametrized energy loss and multiple scattering of the muon in the calorimeter to obtain the muon track parameters and their associated covariance matrix at the closest approach to the beam intersection. The momentum of the standalone muon is combined with the momentum measured in the inner detector. Both muon spectrometer tracks and inner detector tracks are combined by comparing track parameters and their covariance matrices. The following χ^2 variable is used as a measure of the distance between muon tracks and the inner detector tracks. It is defined as:

$$\chi^2 = (\mathbf{T_{MS}} - \mathbf{T_{ID}})^{\mathrm{T}}(\mathbf{C_{MS}} - \mathbf{C_{ID}})^{-1}(\mathbf{T_{MS}} - \mathbf{T_{ID}}) \tag{4.1}$$

where $\mathbf{T}$ is a vector of track parameters expressed at its perigee, $\mathbf{C}$ is its covariance matrix, $\mathbf{MS}$ is the muon spectrometer and $\mathbf{ID}$ is the inner detector.

4.3.1.1 Muon Reconstruction Efficiency

The muon reconstruction efficiencies are determined by the *Tag & Probe* method using $Z \to \mu^+\mu^-$ decays. The sample events are selected by requiring two oppositely charged isolated tracks with an invariant mass near the mass of the Z boson. One of the tracks must be a combined muon and is called the "tag muon". The other track, the "probe", must be an inner detector track and the fraction of probes which can be associated to a combined muon is measured. The conditions in Table 4.2 on the kinematics and isolation are required to "tag muon" and "probe" of $Z \to \mu^+\mu^-$ decays.

Figure 4.7 shows the efficiency for combined muons as a function of η for data and simulation. The scale factor, defined as the ratio between data and simulation, is displayed in the lower panel of the plot.

4.3.2 Muon Identification

The muon object used in the analysis is defined by requiring the following selection criteria to reconstructed combined muons.

- at least one hit on b-layer (the innermost PIXEL detector).

- number of PIXEL hits > 1

Table 4.2: Kinematical conditions to select the tag and probe pairs of $Z \to \mu^+\mu^-$ decays.

	Tag Selection
Kinematics	$p_\mathrm{T} \geq 20\,\mathrm{GeV}\,\&\,|\eta| \leq 2.4\,\&\,|z_0| < 10\,\mathrm{mm}$
Isolation	$\sum_\mathrm{tracks} p_\mathrm{T}^{ID}/p_\mathrm{T} < 0.2$ with tracks inside cone of 0.4 around tag
	Probe Selection
Kinematics	$p_\mathrm{T} \geq 20\,\mathrm{GeV}\,\&\,|\eta| \leq 2.5\,\&\,|z_0| < 10\,\mathrm{mm}$
Isolation	$\sum_\mathrm{tracks} p_\mathrm{T}^{ID}/p_\mathrm{T} < 0.2$ with tracks inside cone of 0.4 around tag

- number of SCT hits > 5

- number of PIXEL holes + number of SCT holes < 3

- denote n = TRThits + TRToutliers

  - for $|\eta| < 1.9$, require $n > 5$ and nTRToutliers/n< 0.9
  - for $|\eta| \geq 1.9$, if $n > 5$ then require nTRToutliers/n< 0.9

Here "hole" is defined as a silicon sensor crossed by a track without generating any associated cluster on the sensor. In the tracking at the Inner detector, the quality of the fitted tracks are compared to the silicon-only track candidates, and hits on track extensions resulting in bad fits are labeled as "outliers". However they are kept as part of the track but are not included in the fit. In addition the muons are required to have $|\eta| < 2.4$ with transverse momentum $p_\mathrm{T} > 25\,\mathrm{GeV}$ (15 GeV for overlap removal and additional lepton veto). The calorimeter energy deposit in a cone $\Delta R = 0.2$ around the muon should be less than $4\,\mathrm{GeV}$. Also the sum of the transverse momentum of tracks in a cone $\Delta R = 0.3$ around the muon is less than 2.5 GeV. The muons are required to be well separated from any high p_T jet requiring $\Delta R(\mu, \mathrm{jet}) > 0.4$ for any jet with $p_\mathrm{T} > 25\,\mathrm{GeV}$ and $|\mathrm{JVF}| > 0.75$. JVF is the jet vertex fraction: a fraction of matched tracks from the hard-scattering compared to the sum of all matched tracks.

4.3.2.1 Muon Identification Efficiency

The muon identification efficiency including additional isolation cuts are derived using $Z \to \mu\mu$ *Tag & Probe* method both data and Monte Carlo sample. The efficiency described from data and its scale factor as function of η and ϕ are shown in Figure 4.8. Muons that satisfy all the requirements shown above are used as tag muon. Probe muons are required that (1) tight muon, (2) $p_\mathrm{T} > 20\,\mathrm{GeV}$, (3) $|M_{tag+probe} - M_Z| < 10\,\mathrm{GeV}$, (4) $\Delta\phi(tag - probe) > 1.5$rad and opposite charge to tag muon.

4.3.3 Muon Momentum Resolution and Scale

The muon momentum resolution and scale are evaluated by invariant mass of di-muon events. The events that have isolated and high transverse momentum muons are well separated from
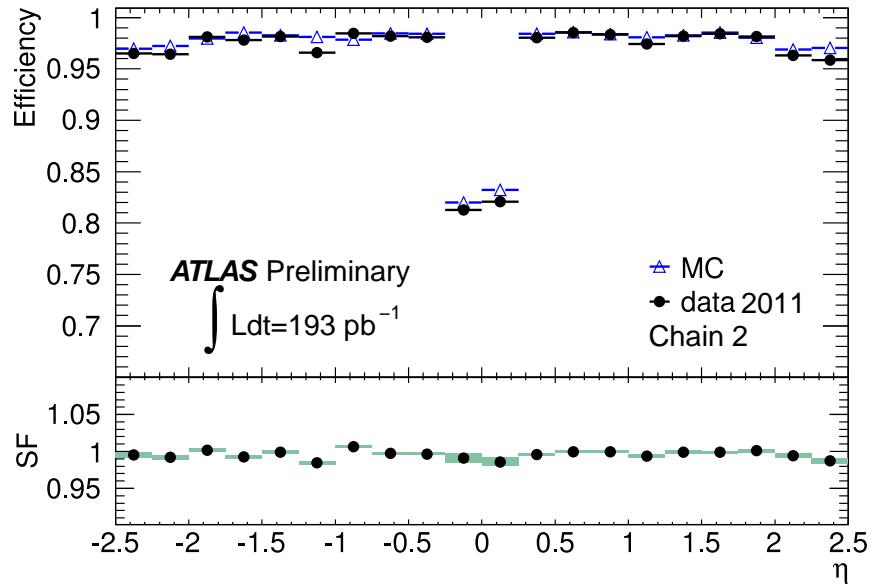
Figure 4.7: Combined muon reconstruction efficiency with respect to the inner tracking efficiency as a function of the pseudorapidity of the muon for muons with $p_\mathrm{T} > 20\,\mathrm{GeV}$. The panel at the bottom shows the ratio between the measured and predicted efficiencies.

(a) Muon identification efficiency
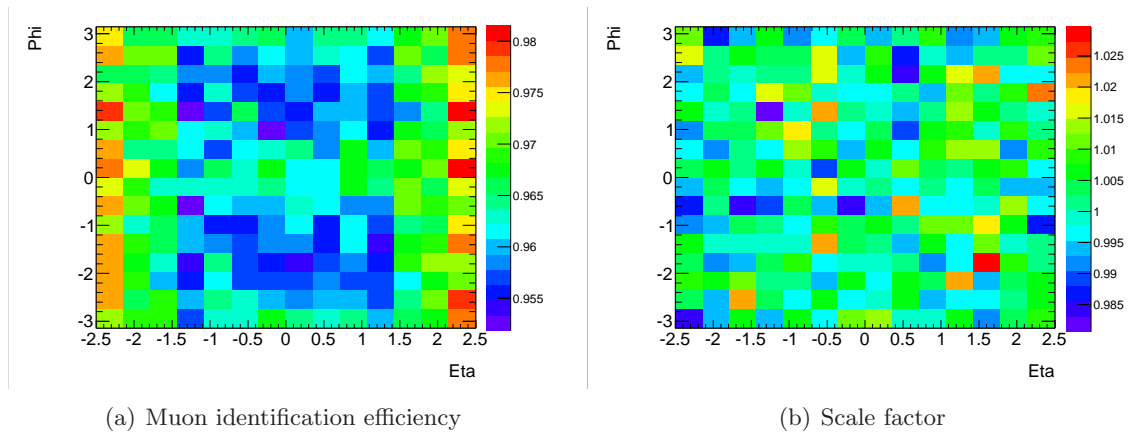
(b) Scale factor

Figure 4.8: Muon identification efficiency and its scale factor on $\eta - \phi$ plane.

background events and clearly can be seen Z boson peak requiring to have opposite charge for both muons. The di-muon invariant mass distribution and its resolution are shown in Figure 4.9. A significant differences are visible between data and Monte Carlo simulation on both plots. Therefore the muon momentum and scale measured at Inner Detector and muon spectrometer in Monte Carlo sample are corrected to match data based on di-muon invariant mass distribution.
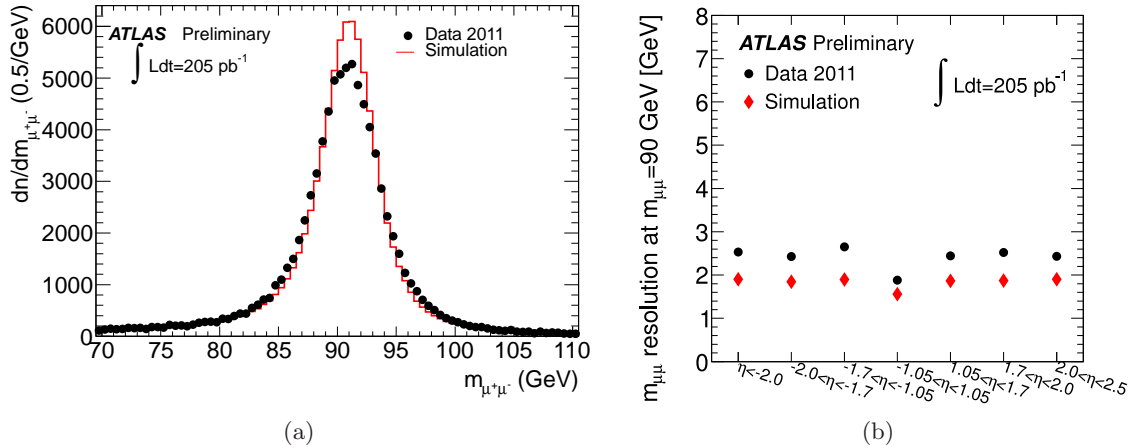
Figure 4.9: Di-muon invariant mass distribution for oppositely charged muon pairs with $p_{\mathrm{T}} > 20\,\mathrm{GeV}$. The muon p_{T} is reconstructed both muon spectrometer and Inner Detector (i.e. combined muon). The muons are required Calorimeter isolation of sum of calorimeter cell energies $< 2\,\mathrm{GeV}$ in a cone of $\Delta R = 0.3$ and $|\eta| < 2.5$. Invariant mass derived from data is compared to Monte Carlo prediction of $Z \to \mu\mu$ generated by Pythia.

4.4 Jet

The jet objects in the analysis are reconstructed from clusters of calorimeter cells with significant energy deposit at the electromagnetic (EM) energy scale. They are clustered by the anti-k_{t} algorithm [33, 34] with a distance parameter of 0.4. Jet finding is performed on clusters at the electromagnetic (EM) scale which accounts for the energy deposited by electrons or photons.

4.4.1 Jet Reconstruction

The electromagnetic and the hadron calorimeter have about 200,000 individual cells and should be combine them as physically meaningful objects for subsequently jet finding algorithm, anti-k_{t}. Clustering of the calorimeter signals are performed topological cell clustering in three-dimension to represent the shower development of each particle in the calorimeter. The clustering starts with seed cells that signal significance $\Gamma = E_{\mathrm{cell}}/\sigma_{\mathrm{noise,cell}}$ exceed the threshold $S_1 = 4$. All cells that are neighbor of seed cells in three dimensions are added into the cluster. Neighbors of neighbors are also added into the cluster if the Γ exceed second threshold of $S_2 = 2$. Finally cells

of the edge of the cluster are also added if significances are above third threshold of $S = 0$. After this initial clustering, a splitting algorithm is applied to the cluster and then analyze local signal maximums to distinguish a number of particles separately. This topological clusters are initially formed using electromagnetic energy scale cells. These clusters can be calibrated to a hadronic energy scale at a classification step that characterize clusters as electromagnetic, hadronic or noise based on their location and shape. Then a correction is applied that is due to energy losses of inactive materials close to or inside the cluster. In addition, calibrations such as pileup, jet direction (point to the primary vertex), jet energy and pseudorapidity to the particle jet scale are applied. Details of jet energy scale is described in section 4.4.3.

From clusters in the calorimeters the jet objects are obtained by the jet clustering algorithm. In the general jet clustering algorithms distances d_{ij} between two entities (clusters or pre-clustered jets) i and j and d_{iB} between entry i and the beam (B). The algorithm searches for the smallest distance and if it is a d_{ij} combines two entities i and j and if it is d_{iB} calls i as a jet and removes it from the list of entities. The clustering is repeated until no entities are left in the list. The following definition of the distance measures is used:

$$d_{ij} = \min(k_{ti}^{2p}, k_{tj}^{2p})\frac{\Delta_{ij}^2}{R^2}, \tag{4.2}$$

$$d_{iB} = k_{ti}^{2p} \tag{4.3}$$

where $\Delta_{ij}^2 = (y_i - yj)^2 + (\phi_i - \phi_j)^2$ and k_{ti}, y_i and ϕ_i are the respectively the transverse momentum, rapidity and azimuth angle of particle i. There are two parameters of the definition: the distance parameter R and a parameter p to control the relative power of the energy and the geometrical distance (Δ_{ij}). In the anti-k_t algorithm $p = -1$ is used. The $d_{1i} = \min(1/k_{t1}^2, 1/k_{ti}^2)\Delta_{1i}^2/R^2$ between a hard particle 1 and a soft particle i is determined by the transverse momentum of the hard particle and the separation Δ_{1i}. Therefore soft particles will tend to cluster with hard ones long before they cluster among them selves.

The jet reconstruction efficiency relative to track jets are measured by *Tag & Probe* method of di-jet event. Track-based jets, track jets, are reconstructed using the anti-k_t algorithm. They are required to be composed of at least two tracks with $p_T^{track} > 500$ MeV and to have hits on silicon trackers, with an impact parameter in the transverse plane and an impact parameter in the z-direction ≤ 1.5 mm. The highest p_T track jet in the event is defined as the tag object. The reconstruction efficiency corresponds to a matching efficiency can be defined by searching for calorimeter jets matched to the probe track jet in a di-jet back-to-back event topology. The determined jet reconstruction efficiency relative to track jets is shown in Figure 4.10.

4.4.2 Jet Identification

The jet quality selection criteria are applied to remove the fake caused from hardware problems, cosmic rays, beam-gas interaction and other sources. A discriminant, jet vertex fraction (JVF) which exploits the fraction of tracks coming from the primary vertex within all tracks associated to the jet to estimate the contribution of multiple interactions. If the jet is produced from the
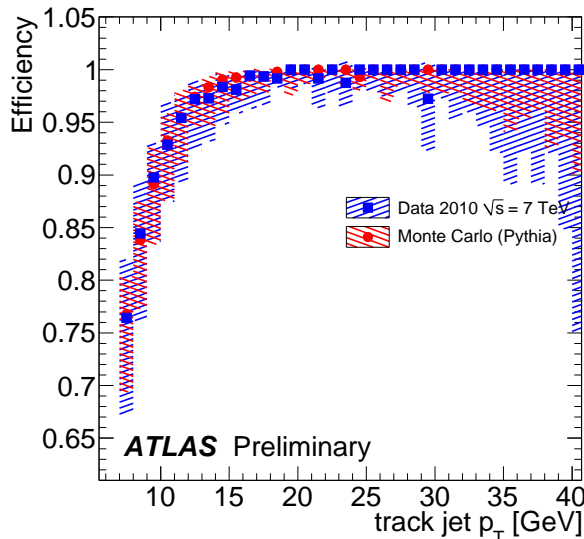
Figure 4.10: Jet reconstruction efficiency relative to track jet [35].

primary vertex, this discriminant variable becomes sufficiently larger. The definition of JVF is

$$\text{JVF}(\text{jet}_i, \text{vtx}_j) = \frac{\sum_k p_{\text{T}}(\text{trk}_k^{\text{jet}_i}, \text{vtx}_j)}{\sum_n \sum_l p_{\text{T}}(\text{trk}_l^{\text{jet}_i}, \text{vtx}_n)} \tag{4.4}$$

where vtx are primary vertices and trk are charged tracks matched to primary vertex inside the jet. It means that the JVF is the track p_{T} fraction from vertex j. A cut on the JVF is applied to further reduce the effect on in-time pile-up. The optimal working point that achieves the best rejection factor for pile-up jets while maintaining an efficient selection of hard scatter jets is $|\text{JVF}| > 0.75$. We require to have the jet with $p_{\text{T}} > 25\,\text{GeV}$ and $|\eta| < 2.5$ but reject if $|\text{JVF}| < 0.75$.

4.4.3 Jet Energy Scale and Resolution

After jet reconstruction using anti-k_{t} algorithm, energy and direction are calibrated. At first, the energy offset that introduced by pileup is corrected. The correction are derived from di-jet event Monte Carlos sample produced by PYTHIA as a function of the number of reconstructed primary vertices (measured from collision data) and the expected average number of interactions μ in bins of jet pseudorapidity and transverse momentum. Second, the jet direction is changed to point to the primary vertex instead of the center of the ATLAS detector. Third, the jet energy is calibrated to apply correction scale that derived simply to compare the reconstructed jet energy and the Monte Carlo (the same as above) truth jet energy. The average energy response $R = E_{jet}^{EM}/E_{jet}^{truth}$ for various jet energies as a function of the jet pseudorapidity is shown in Figure 4.12. After the first jet energy scale calibration step described above, the jet transverse momentum $p_{\text{T}}^{\text{jet}}$ in data

(a) Illustration of JVF

(b) Jet Vertex Fraction
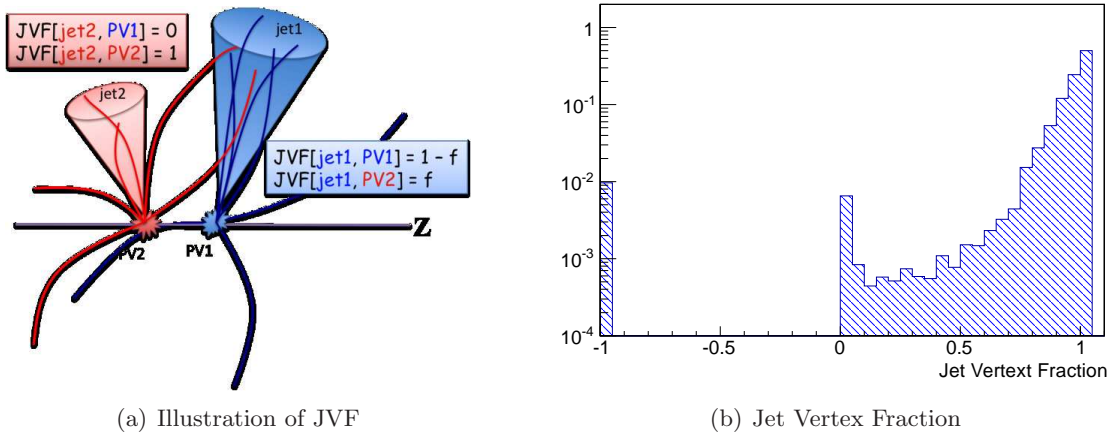
Figure 4.11: Conceptual illustration of Jet Vertex Fraction (JVF) and JVF distribution of selected jet with $p_T > 25\,\text{GeV}$ and $|\eta| < 2.5$. JVF = 1: little or no contributions from pileup to jets, JVF < 1: some additional tracks originate from primary interaction, JVF = 0: all charged tracks originate from pileup, JVF = -1 jets without matched tracks.
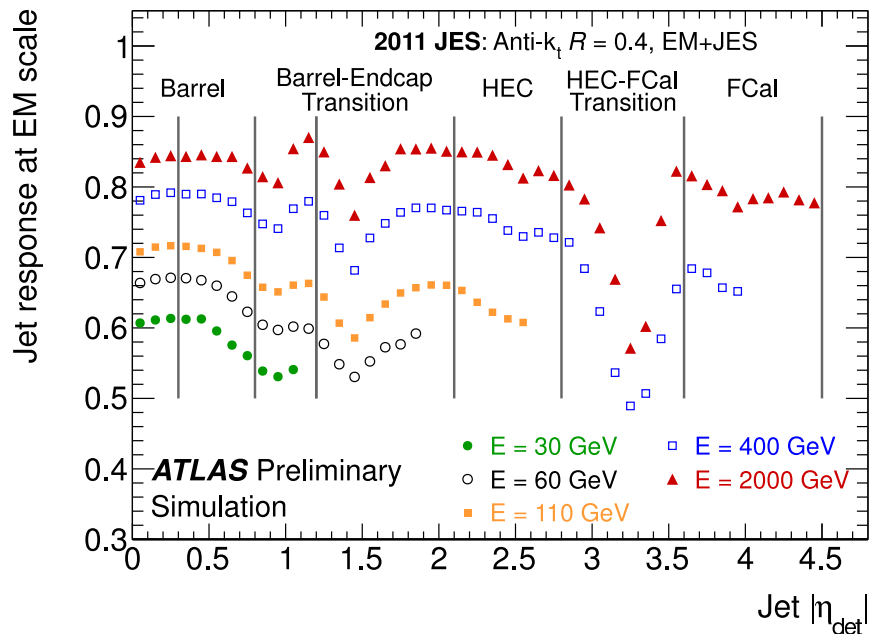
Figure 4.12: Average jet energy response at each calorimeter region as a function of reconstructed jet pseudorapidity [36]. The inverse of this response value is corresponding to the average jet energy scale correction.

is compared to the jet p_T in Monte Carlo simulation using *in situ* techniques that exploit the p_T balance between the $p_T{}^{\text{jet}}$ and the p_T of a reference object $p_T{}^{\text{ref}}$:

$$\langle p_T{}^{\text{jet}}/p_T{}^{\text{ref}}\rangle_{\text{data}}/\langle p_T{}^{\text{jet}}/p_T{}^{\text{ref}}\rangle_{\text{MC}} \tag{4.5}$$

This quantity is the residual *in situ* jet energy correction for the jets measured in data. First the pseudorapidity dependence of the jet response is removed using the p_T balance of di-jet between a central within $|\eta| < 0.8$ and a forward jet within $0.8 \le |\eta| < 4.5$ (denoted as η-intercalibration). After that, the quantity (4.5) is derived by using the p_T of a photon or a Z boson which decay to e^+e^- or $\mu^+\mu^-$ as reference. The jet energy scale correction is obtained from a combination of both methods, Z+jet and γ+jet, and the corresponding uncertainty is determined. Finally, events that a system of low-p_T jets recoils against a high-p_T jet are used to calibrate jets in the TeV regime.

Jet energy resolution is evaluated with the transverse momentum balance of the di-jet events. The fractional jet energy resolution as a function of the average jet transverse momenta is shown in Figure 4.13. Typically the difference of resolution between Monte Carlo (di-jet PYTHIA sample) and collision data is within 10% and there is no additional correction for reconstructed jets energy resolution in the Monte Carlo sample.
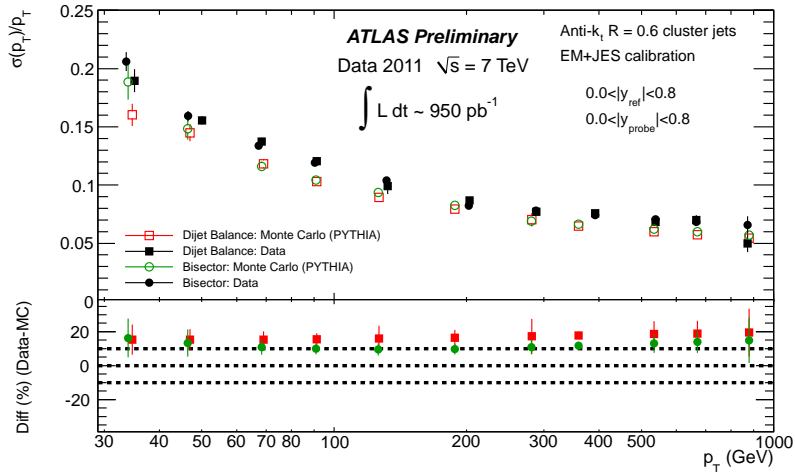
Figure 4.13: Fractional jet energy resolution as a function of the average jet transverse momenta for the di-jet balance techniques [37].

4.5 Missing Transverse Energy

The missing transverse energy E_T^{miss} is calculated as a vector sum of calorimeter cell energies which are calibrated according to the associated high p_T physics objects: electron, jet, soft jets and muons. The ordering of these objects indicate the order of association of the cell to the objects. The energies remaining cells that are not associated to any high p_T objects are included

as a "CellOut" term into the calculation of the missing transverse energy and are calibrated to the EM scale. The $E_{\mathrm{T}}^{\mathrm{miss}}$ is calculated as

$$E_{\mathrm{T}}^{\mathrm{miss}} = \sqrt{\left(E_{\mathrm{x}}^{\mathrm{miss}}\right)^2 + \left(E_{\mathrm{T}}^{\mathrm{miss}}\right)^2} \tag{4.6}$$

where

$$-E_{\mathrm{x,y}}^{\mathrm{miss}} = E_{\mathrm{x,y}}^{\mathrm{Elec}} + E_{\mathrm{x,y}}^{\mathrm{Jet}} + E_{\mathrm{x,y}}^{\mathrm{SoftJet}} + E_{\mathrm{x,y}}^{\mathrm{Muon}} + E_{\mathrm{x,y}}^{\mathrm{CellOut}} \tag{4.7}$$

The electron term uses electrons satisfying the tight electron requirement definition with a $p_{\mathrm{T}} > 10\,\mathrm{GeV}$ where the electron energy scale used in the $E_{\mathrm{T}}^{\mathrm{miss}}$ calculation includes all the electron correction factors. For the jets, there are two criteria: refined jets which are included into the $E_{\mathrm{T}}^{\mathrm{miss}}$ at the EM+JES energy scale; and soft jets which are included at the EM scale. The refined jets are required to have with a $p_{\mathrm{T}} > 20\,\mathrm{GeV}$, while the jets between $7\,\mathrm{GeV}$ and $20\,\mathrm{GeV}$ are included as soft jets. The muon term in the $E_{\mathrm{T}}^{\mathrm{miss}}$ is determined from transverse momenta of muons which is defined by Muid muon algorithm for the full acceptance range of the muon spectrometers of $|\eta| < 2.7$. All combined muons within $|\eta| < 2.5$ are included in the $E_{\mathrm{T}}^{\mathrm{miss}}$. The muon term in the $E_{\mathrm{T}}^{\mathrm{miss}}$ also contains both isolated and non-isolated muons. It requires the tracks to be isolated from all jets with cone size 0.4 by $\Delta R = 0.3$ for isolated muons, and includes the muon energy deposited in the calorimeter in the Cell Out term. Non-isolated muons, the energy deposited in the calorimeter is included in the jet term. On the other hand, its z-component cannot be measured because the z-boost of hard pp collisions cannot be known for hadron colliders.

The resolutions of missing transverse energy is obtained from missing energy in x- and y-axis, denoted E_x^{miss} and E_y^{miss}, with $Z \to \ell\ell$ sample shown in Figure 4.14 as a function of the total transverse energy $\sum E^{\mathrm{T}}$. In $Z \to \ell\ell$, it expect no genuine missing transverse energy. Therefore the resolution of the E_x^{miss} and E_y^{miss} can be measured from collision data directly to assume the true values of them are equal to zero. The resolution as shown in Figure 4.14 is evaluated from the width of the combined distribution of reconstructed E_x^{miss} and E_y^{miss}.

4.6 Bottom Quark Tagging

Because top quarks decay into a b-quark and W boson, we require the existence of b-jets originating from b-quarks in the final state in order to suppress background that are not related to top quark productions. We use the following three algorithms to tag b-jets in this analysis: IP3D, SV1 and JetFitter. They are all based on the long life time of B-mesons which are produced in b-jets and use the reconstructed vertex displace from the primary one and the large impact parameter of charged tracks. The outputs of these three algorithms are used together with the p_{T} and $|\eta|$ of the jet as a discriminant variable of a neural network of MV1-tagger. We choose to require the weight of MV1 at 70% efficiency point.
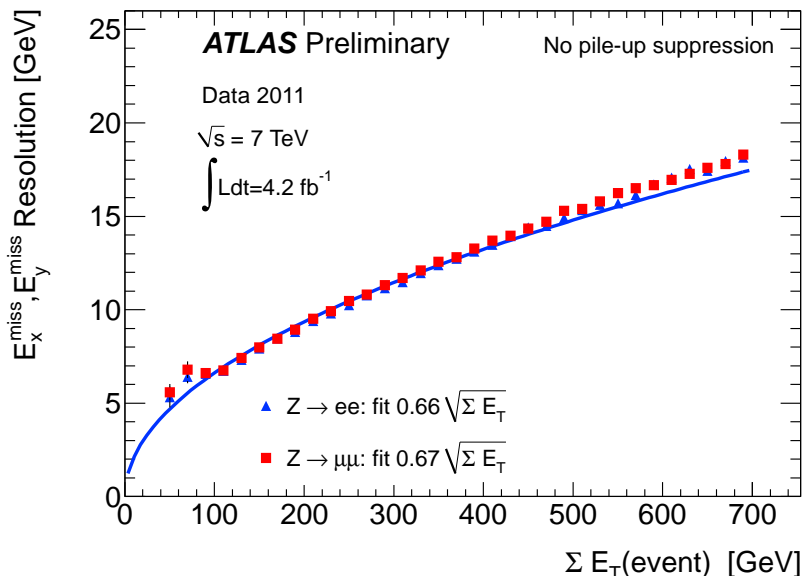
Figure 4.14: The resolution of missing energy on x and y axis [38].

4.6.1 Impact parameter based algorithms (IP3D)

4.6.1.1 Transverse impact parameter

The impact parameter of tracks is computed with respect to the primary vertex candidate. The sign of the impact parameter is defined as positive if the angle between the jet direction and the line joining the primary vertex to the point of closest approach of the track is less that 90°, negative otherwise. The experimental resolution generates a random sign for the tracks originating from the primary vertex while tracks from c- or b-hadron decays tend to have a positive sign. The impact parameter has both transverse (d_0) and longitudinal (z_0) components. The distribution of the signed transverse impact parameter d_0 is shown in Figure 4.15. The significance distribution $S_{d_0} \equiv d_0/\sigma_{d_0}$ which gives more weight to precisely measured tracks is shown in Figure 4.15.

4.6.1.2 IP3D

All impact parameters in the event with $|d_0| < 1$ mm and $|z_0 \sin\theta| < 1.5$ mm whose p_T is larger than 1 GeV are used in the IP3D method. The IP3D employs uses a likelihood ratio technique in which input variables S_i of discriminating variables, here significance of impact parameter S_{d_0} and S_{z_0}, are compared to pre-defined smoothed and normalized distributions for both the b and light jet hypotheses like Figure 4.15(b), $b(S_i)$ and $u(S_i)$ that obtained from Monte Carlo simulation. The ratio of the probabilities $b(S_i)/u(S_i)$ defines the track weight which can be combined into a
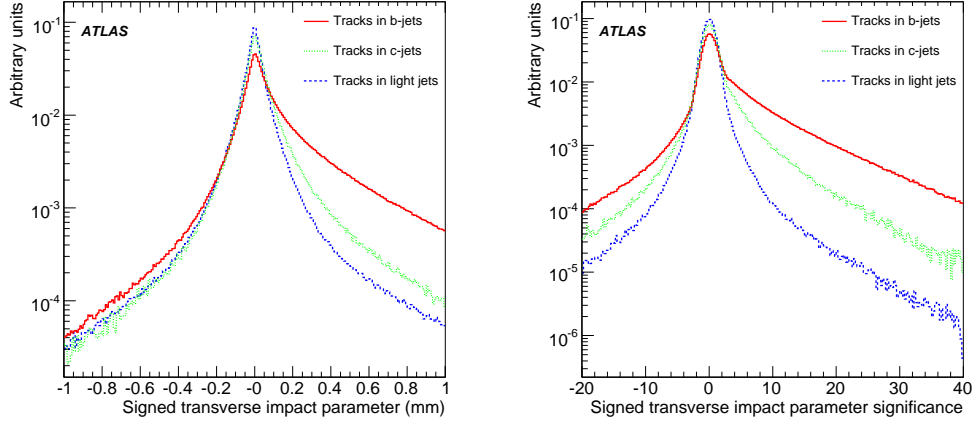
(a) The signed transverse impact parameter d_0 for light jets, c-jets and b-jets.

(b) The signed significance S_{d_0} for light jets, c-jets and b-jets.

Figure 4.15: The signed impact parameter and its significance [39].

jet weight W_{jet} as the sum the logarithms of the N_{trk} individual track weights W_i written in

$$W_{\text{jet}} = \sum_{i=1}^{N_{\text{trk}}} W_i = \prod_{i=1}^{N_{\text{trk}}} \ln \frac{b(S_i)}{u(S_i)} \tag{4.8}$$

and shown in Figure 4.16

4.6.2 Secondary vertex based algorithms (SV1)

In some cases, the secondary vertex of the decay of b-hadrons and also that of subsequent charm hadrons can be reconstructed within a b-jet. The reconstruction of secondary vertices starts by building a two-track pair that forms a good vertex from all tracks in the jet which are not associated to the primary vertex. Once a two-track vertex is formed, other tracks are combined into the vertex iteratively by removing the track which gives the worst χ^2 of the vertex fit.

4.6.2.1 SV1

For the reconstruction of secondary vertices used in the SV1 method, tracks associated to the secondary vertex should have $p_T > 400\,\text{MeV}$, $|d_0| < 3.5$ mm (no cut on z_0), at least one hit in the PIXEL (no requirement on the innermost pixel layer) and no more than one hit on the track shared with another track. The decay length significance of the vertex, $L_{3D}/\sigma_{L_{3D}}$, is measured in 3-dimensionally from the primary vertex and is also signed as the same as the track impact parameter. In order to increase the discrimination power of the SV1 algorithm, the method also takes into account the following three properties of the secondary vertices: the invariant mass of all tracks associated to the vertex, the ratio of the sum of the energies of the tracks in the
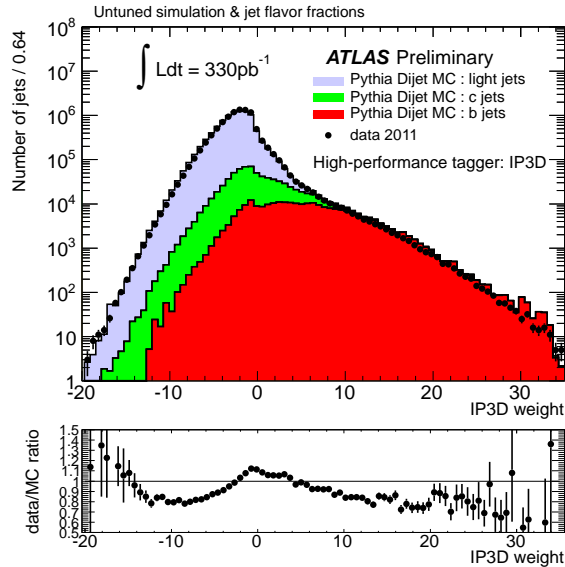
Figure 4.16: IP3D weight [40]

vertex to the sum of the energies of all tracks in the jet, and the number of two-track vertices are shown in Figure 4.17 [31]. These variables are combined using a likelihood ratio technique which is explained in the previous section. In addition the distance ΔR between the jet axis and the line joining the primary vertex to the secondary one is used.

4.6.3 Decay chain reconstruction algorithm — JetFitter

This algorithm exploits the topological structure of weak b- and c-hadron decays inside the jet. It assumes that the b- and c-hadron decay vertices lie on the same line of b-hadron flight path. It can be expected that all charged particle tracks stemming from the b- or c-hadron decay intersect this b-hadron flight path.

4.6.3.1 JetFitter

A Kalman filter [41] is used to find a common line on which the primary vertex, the b- and c-hadron vertices lie as well as their position on this line to give an approximated flight path of the b-hadron.

After finding the decay chain from primary vertex to c-hadron, the b-tagging algorithm of *JetFitter* is based on the separation of b-jets from c- and light jets and give several properties to likelihood function to tag b-jets. The decay topology of b- and c-hadron are described by the following variables:

- Number of vertices with at least two tracks.

- Total number of tracks at these vertices.

45
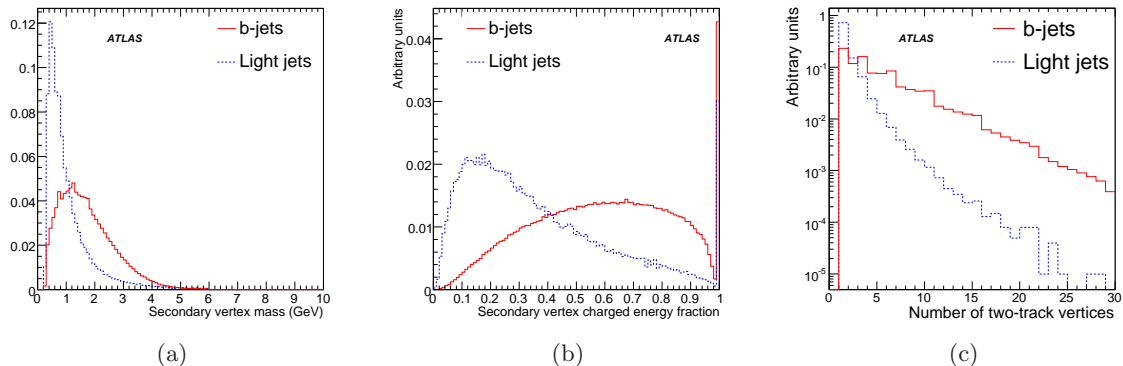
Figure 4.17: The invariant mass of all tracks associated to the vertex 4.17(a), the ratio of the sum of the energies of the tracks in the vertex to the sum of the energies of all tracks in the jet 4.17(b), and the number of two-track vertices 4.17(c).

- Number of additional single track vertices on the b-hadron flight axis

The vertex information are following variables:

- The invariant mass of all charged particle tracks attached to the decay chain.

- The fraction of energy of these particles and the sum of the energies of all charged particles matched to the jet.

- The flight length significance $\frac{d}{\sigma(d)}$

The likelihood function is defined to use probability density functions (PDFs) of these discriminant variable:

$$L_{b,c,l}(x) = \sum_{cat} \text{coeff}(cat) \cdot \text{PDF}_{cat}(\text{mass}) \cdot \text{PDF}_{cat}(\text{energyfrac.}) \cdot \text{PDF}_{\text{cat}} \frac{d}{\sigma(d)} \qquad (4.9)$$

The information about the decay topology of the jet reconstructed by $JetFitter$ is represented by category (denoted by cat) as shown in Figure 4.18 and the vertex information is contained in the PDFs and shown in Figure 4.19. The Coefficient $coeff(cat)$ intends how probable it is to find a certain topology for a given flavor.

4.6.4 MV1

The results of these three algorithms are combined to extract a final tagging discrimination weight for each jet. MV1 tagger takes the output weights of these tagging algorithms with p_T and η of the jet as an input to a neural network to determine a single discriminant variable. The light jet rejection as a function of the b-tag efficiency for the b-tagging algorithms based on simulated $t\bar{t}$ events is shown in Figure 4.21 [43].

Figure 4.18: Category of the decay topology [42]. (1) the number of vertices with at least two tracks, (2) number of total tracks at vertices with at least two tracks and (3) number of additional single tracks.
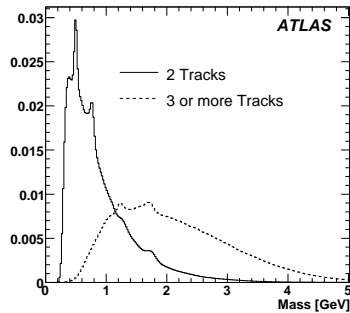
(a) The invariant mass of all charged tracks
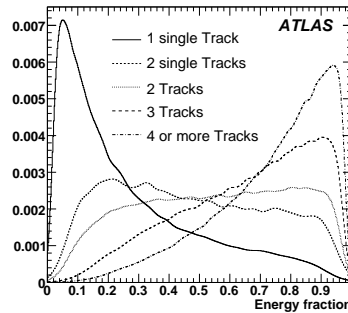
(b) Energy fraction
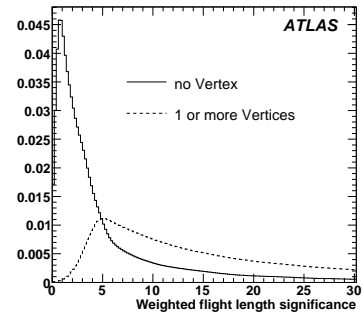
(c) Flight length significance

Figure 4.19: The vertex information of b-jet for likelihood discriminant variable [42]. Here vertices have at least two tracks. Single tracks are considered if there is no vertex with at least two tracks.

b-tagging efficiency and mistag rate of light jet are evaluated by both data and Monte Carlo simulation. The difference between data and Monte Carlo simulation is corrected to apply the scale factor to Monte Carlo according to jet-flavor (truth information of Monte Carlo), transverse momentum and pseudo rapidity of jet. The b-jet tagging efficiency and its scale factor for the *MV1* b-tagger are estimated based on QCD multi-jet event which contains the muon inside the jet (semi leptonic decay of heavy flavor) to enhance the b-jet. The b-tag efficiency scale factor at 70% efficiency point as function of jet transverse momentum p_T are shown in Figure 4.20. The uncertainties are including both statistical and systematic.

In the figure, *pTrel* (p_T^{rel}) and *system 8* methods are based on QCD multi-jet events and the others are based on sample of $t\bar{t}$ lepton+jets or di-lepton channel. For this analysis the combination of p_T^{rel}, *system8*, *KinSel DL* and *KinFit SL* are used. p_T^{rel} is defined as the momentum of the muon transverse to the muon plus jet axis. Templates of p_T^{rel} are constructed for b-, c- and light jets and then these are fit to data distribution to obtain the number of events of each jets. The ratio of number of events of b-jets before and after b-tagging is equivalent to b-tag efficiency. *System 8* solve a system of equations with eight unknowns: the efficiencies for b and non-b jets to pass each of the three selection criteria and the number of b and non-b jets. The kinematic selection method by using $t\bar{t}$ di-lepton channel is denoted as *KinSel DL*. The two leading jets are considered as b-jets. If one of the jet is b-tagged, the b-tagging rate of another jet is measured. The kinematic fit based method by using $t\bar{t}$ lepton+jets channel is denoted as *KinFit SL*. After reconstruction the $t\bar{t}$, the jet assigned as b-jet from leptonically decaying top is used for determination of b-tag efficiency.
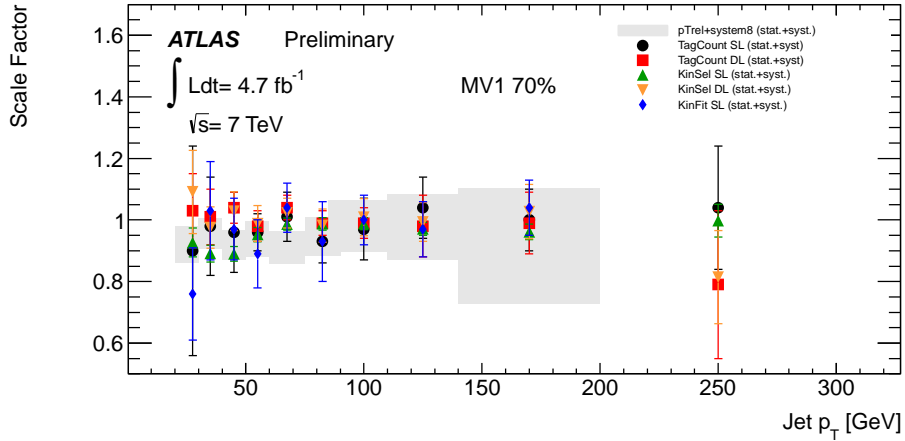
Figure 4.20: Comparison of all $t\bar{t}$ based scale factors with the combined scale factor based on QCD multi-jet event [44].

(a) MV1 weight

(b) Light jet rejection as a function of b-tag efficiency based on simulated $t\bar{t}$ events.
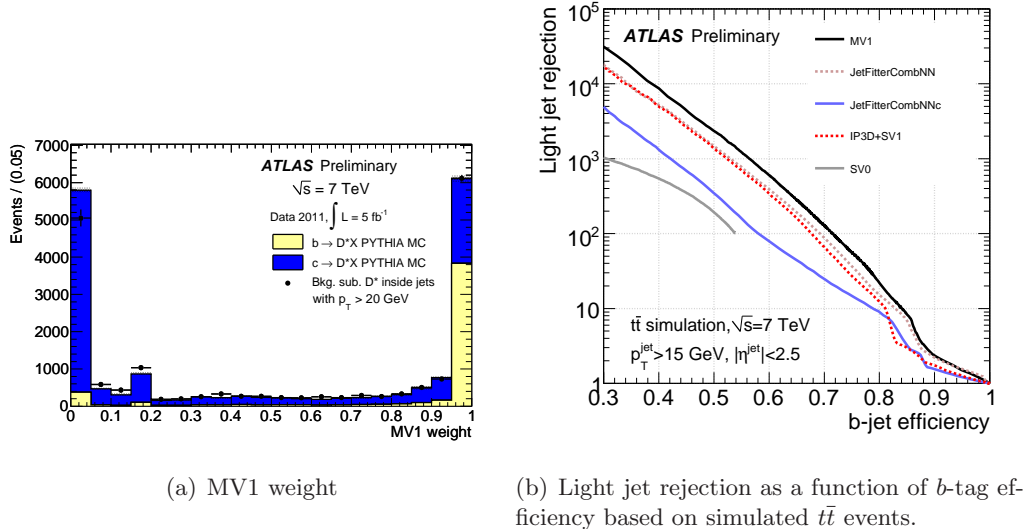
Figure 4.21: *MV1* weight and light jet rejection [42]. For this analysis, 70% efficiency point of *MV1* weight > 0.601713 is required to jets. Light jet rejection is 134 at this point.

4.7 Offline Data Processing

Events that pass through all level of trigger requirements are acquired as intriguing data and copy to Tier-0 grid center at CERN Advanced STORage Manager (CASTOR) as RAW data. The size of RAW data is approximately 1.6 MB/event. The first calibration and reconstruction of collision data is performed at Tier-0 within 36 hours after end of each data taking run. At this level, the RAW data is reconstructed to tracks (and their hits), calorimeter clusters, calorimeter cells and combined reconstruction objects and then stored as Event Summary Data (ESD). Nominal size of ESD is 1 MB/event. ESD is used for mainly the detector performance study to improve the understanding. After process of ESD, using these detector information, the physics objects such as electrons, muons, jets and so on are reconstructed and stored as Analysis Object Data (AOD) for physics analysis. Roughly nominal event size is 100 kB/event. In addition, AOD is merged/skimmed/slimmed as Derived Physics Data (DPD) to derive necessary variables or events based on each physics object performance studies (e/γ, μ, τ, jet etc) or physics analyses channels (Higgs, SUSY, $t\bar{t}$ etc). Nominally 10 kB/event on average. These RAW, ESD, AOD and DPD are distributed to ten of Tier-1 grid centers in the world and take care of a fraction of RAW data forever. At Tier-1, rerun reconstruction with latest calibration, alignment and algorithms a few months after end of data taking period and distribute output to Tier-2 grid centers (~ 35 sites). Tier-2 centers process analysis jobs mainly AOD, DPD and Monte Carlo simulations. Processed AOD and DPD are also distributed to Tier-3 grid centers. Grid resources and local storage can be accessed at Tier-3 for end-user. The data sets including all Monte Carlos simulation which used for this analysis are taken from several Tier-3 grid sites.

Chapter 5

Trigger and Event Selection

5.1 Trigger

5.1.1 Electron Trigger

Events that have high p_{T} electrons within $|\eta| < 2.5$ are recorded by following three levels of single electron trigger.

5.1.1.1 Level-1 Trigger
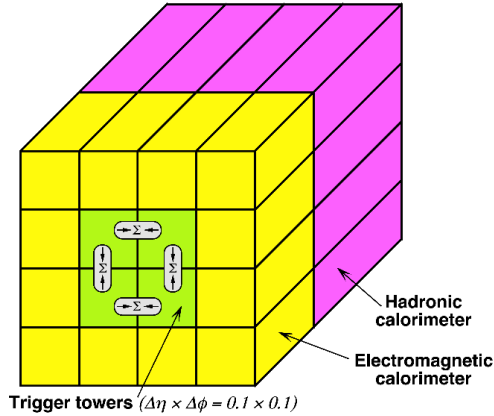
Figure 5.1: Elements for the electron trigger algorithm.

Level-1 (L1) electron trigger utilizes reduced granularity signals covering $\Delta\eta \times \Delta\phi \approx 0.1 \times 0.1$ (*trigger towers*, Figure 5.1) from the calorimeters to identify the positions of Regions of Interest (RoIs) and calculate the transverse energy of electromagnetic clusters with a precision of 1 GeV. The cells of the EM or hadronic calorimeter are summed for each trigger tower except the fourth layer of the hadronic endcap and barrel endcap gap scintillators. EM clusters are formed by identifying local maxima using a sliding window algorithm based on a 4×4 group of trigger

towers. A trigger is satisfied if the window's core-region which is the central 2×2 trigger towers contains one pair of neighboring towers with a combined energy passes the threshold (14 and 16 GeV for this analysis).

5.1.1.2 Level-2 and Event Filter

At Level-2 (L2) electron calorimeter algorithms build cell clusters at the second layer of the EM calorimeter within the RoI ($\Delta\eta \times \Delta\phi \approx 0.4 \times 0.4$) that identified by the L1. The cluster-finding algorithm forms seeds from cluster towers with units of $\Delta\eta \times \Delta\phi = 0.025 \times 0.025$ using sliding window algorithm with a window size of 3×7 ($\eta \times \phi$). In addiction, information from the Inner Detector is available at L2. At the L2, electron are identified by applying requirements on the deposit of energy in the hadronic calorimeter within the RoI , shower shape at middle layer of EM calorimeter and matching between seed and Inner Detector track with $p_T > 5$ GeV.

At the EF, the identification of electron is performed using the offline identification variables and offline selection defined three operating points, *loose, medium and tight*. Details of variables and identification are described at Section 4.2.2. For this analysis we required to fire *e20_medium*, *e22_medium* and *e22vh_medium1* trigger with rising instantaneous luminosity. Corresponding threshold of transverse energy are 20 and 22 GeV. Table 5.1 shows the trigger names and rates of the single electron.

Table 5.1: Electron trigger menu summary used for this analysis.

Trigger Signature	L1 Seed	Lumi Range $(\text{cm}^{-2}\text{s}^{-1})$	L1 Rate (Hz)	L2 Rate (Hz)	EF Rate (Hz)
e20_medium	EM14	up to 2×10^{33}	7300	273	50
e22_medium	EM16	$2\text{-}2.3 \times 10^{33}$	5700	273	45
e22vh_medium1	EM16VH	from 2.3×10^{33}	3600	150	22

5.1.1.3 Trigger Efficiency

The efficiencies of the L2 and EF (HLT) electron selection were measured with respect to offline electrons of $Z \rightarrow ee$ events using a *Tag & Probe* method. For measuring the HLT efficiencies, the tag is defined as the offline electron that match an online electron passing the unprescaled single electron trigger if the distance between them within $\Delta R < 0.15$. The tag electron is also required to have $p_T > 25$ GeV to satisfy the tight offline electron identification, to lie within $|\eta| < 2.47$ excluding the transition region between the barrel and the endcaps and isolated from a jets with $p_T > 10$ GeV, $\Delta R > 0.4$. A second electron with opposite charge to the tag is considered as a probe if the invariant mass of the electron pair is in the range 80 GeV $< m_{ee} <$ 100 GeV. The trigger efficiency is the fraction of probes that match an online electron passing the trigger selection at the HLT and shown in Figure 5.2.
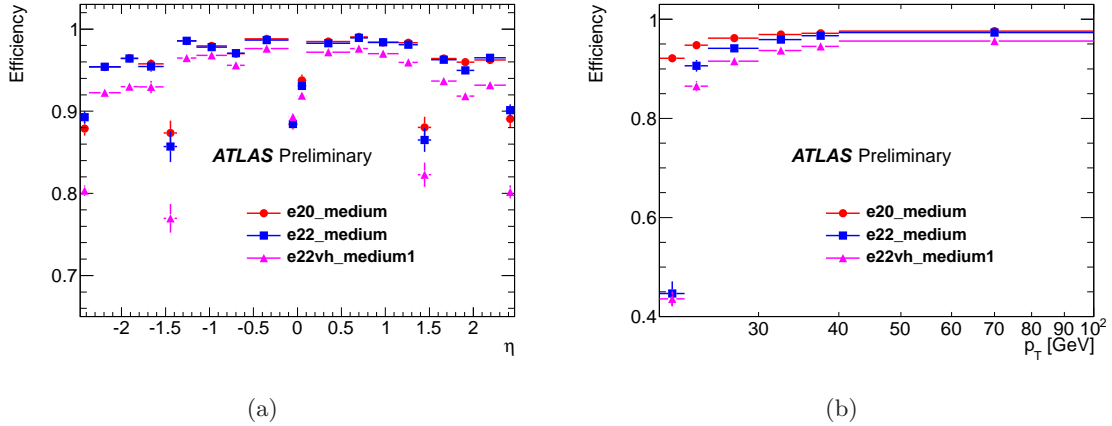
Figure 5.2: Electron trigger efficiency measured with the *Tag & Probe* method for data with respect to *e20_medium*, *e22_medium* and *e22vh_medium* as a function of electron η and p_T.

5.1.2 Muon Trigger

Quarter-section of the muon spectrometers containing the beam axis is shown in Figure 5.3. Three layers of thin gap Chambers (TGC) and three layers of resistive plate Chambers (RPC) provide the muon trigger. Events that have high p_{rmT} muons within $|\eta| < 2.4$ are recorded by following three levels single muon trigger.

5.1.2.1 Level-1 Trigger

A L1 muon trigger signal carries the estimated p_T information of the muon and the position information of the detector region to be analyzed in the HLT. The geometric coverage of the L1 trigger in the end-cap regions (TGC) is about 99% and is about 80% in the barrel region (RPC). Muon candidates are identified that forms a coincidence of hits in layers of trigger chambers. The hit pattern along the muon trajectory that is bent in the magnetic field is used to estimate the muon p_T.

5.1.2.2 Level-2 and Event Filter

At the L2, the candidate from L1 is refined by using the precision data from the MDTs. The L2 muon standalone algorithm constructs a track from the muon spectrometers data within the RoI defined by the L1 seed, and determine the track parameter and p_T. Then reconstructed tracks in the inner detector are combined with the tracks found by the L2 muon and refine the track parameter resolution. At the EF, the full event data are accessible thus the algorithms that are very similar to the offline one are used. First the muon candidate is combined with an inner detector track to form an EF muon combined trigger. This "outside-in" strategy is complemented by another algorithm which starts with inner detector tracks and extrapolate them to the muon detectors to form EF muon "inside-out" triggers. Both outside-in and inside-out algorithms are
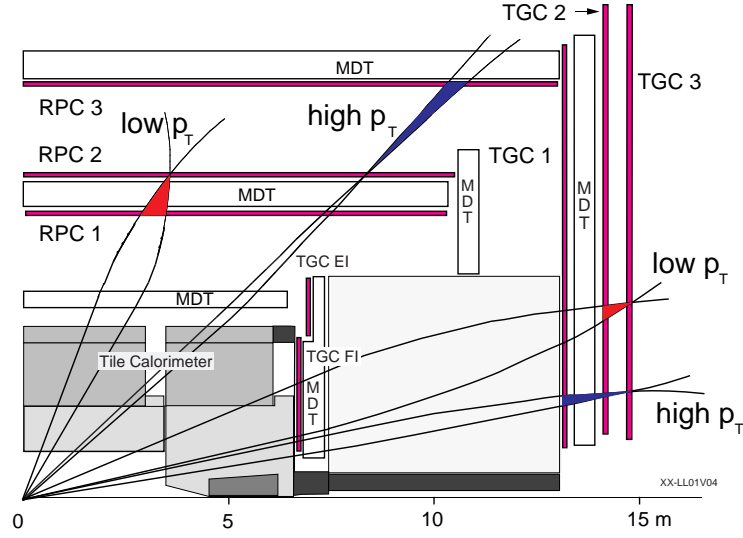
Figure 5.3: Quarter-section of the muon sub-systems.

used in parallel for online muon reconstruction in the EF to minimize the risk of losing events.

During the 2011 data taking, the p_T threshold of the lowest unprescaled single muon trigger chains were kept at 18 GeV They are seeded by the L1 trigger using the threshold of 10 GeV (L1_MU10) and 11 GeV (L1_MU11) and called mu18 and mu18_medium. At the L2, the tracks constructing at the muon spectrometer standalone are required to have $p_T > 6$ GeV and the combined tracks constructing with inner detector are required to have $p_T > 18$ GeV. Summarize the trigger menu that used for this analysis is shown in Table 5.2.

Table 5.2: Summary of the muon trigger menu. The L1_MU10 trigger consists of the two (three) station coincidence trigger in the barrel (endcap) region, and the L1_MU11 trigger composed of coincidences of hits from three stations in both barrel and endcap regions. The L1_MU10 trigger was prescaled while instantaneous luminosity was above 1.9×10^{33} cm^{-2}s^{-1}. The EF rates show only mu18_medium.

Trigger Signature	L1 Seed	Lumi Range (cm^{-2}s^{-1})	L1 Rate (Hz)	EF Rate (Hz)
mu18(_medium) outside-in	L1_MU10 (L1_MU11)	up to $1.9\,(3.0) \times 10^{33}$	24 (8)	109
mu18(_medium) inside-out	L1_MU10 (L1_MU11)	up to $1.9\,(3.0) \times 10^{33}$	24 (8)	111

5.1.2.3   Muon Trigger Efficiency

The muon trigger efficiencies, mu18 and mu18_medium with respect to isolated offline combined muon, are measured using the $Z \to \mu^+\mu^-$ *Tag & Probe* method with collision data and Monte

Carlo events. Figure 5.4 shows measured efficiencies of mu18_medium with data and Monte Carlo sample in the barrel and endcap regions as a function of muon p_T for the outside-in and the inside-out algorithms. The measured scale factor as a function of muon η and ϕ for barrel and endcap regions are shown in Figure 5.5. The uncertainty on the scale factors in typically 1% per bin from the $Z \to \mu^+\mu^-$ event statistics. The systematics uncertainty is typically 1% per bin.

(a)

(b)

(c)

(d)
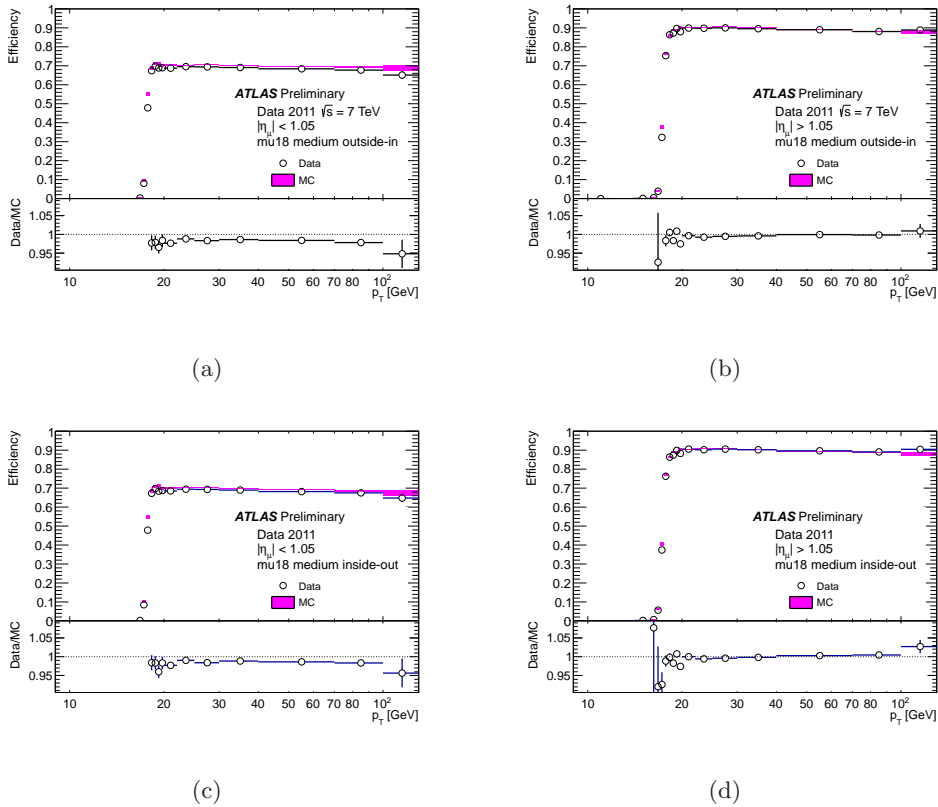
Figure 5.4: Efficiencies of the mu18_medium trigger chains in terms of the offline reconstructed muon p_T. (a) and (b) show efficiencies of the triggers with the muon spectrometer track based algorithm (outside-in) in the barrel and endcap regions. (c) and (d) show the trigger efficiencies using the inner detector track based algorithm (inside-out) in the barrel and endcap regions. The efficiencies includes the geometric acceptance of the L1 trigger chambers [45].

Real data used in this analysis is selected from stable LHC running periods in 2011, corresponding to the integrated luminosity of 4.7 fb^{-1}. Event selection is optimized to select $t\bar{t}$ lepton+jets channel: an isolated high p_T lepton and missing transverse energy are the signature of W boson decaying into a lepton and neutrino. The jet requirements are designed to find the jets from hadronically decaying W boson and hadronization of b-quark from top quark decay directly.
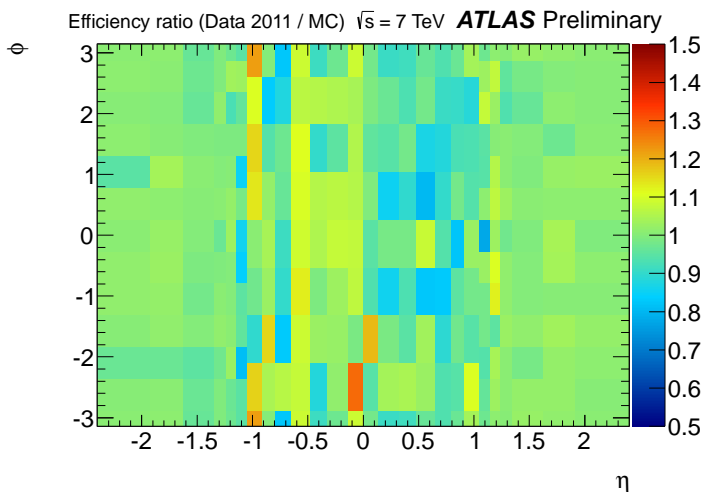
Figure 5.5: The $\eta - \phi$ dependence of the mu18_medium trigger efficiency scale factor with inner detector track based algorithm at EF (inside-out) [45].

5.2 Event Selections

In this section the conditions used to select $t\bar{t}$ signal events from data are listed.

5.2.1 Trigger condition

First the event is required to be triggered by the single-lepton trigger (described Section 5.1.1 and 5.1.2). The trigger threshold at the Event Filter level for electrons is 20 GeV (before period K) and 22 GeV (starting period K) for the data taking in 2011. That for muons is 18 GeV for the whole data taking period.

5.2.2 Primary vertex

The event is required to have a primary vertex. The primary vertex is defined as follows. First charged tracks which are compatible with a beam spot are selected with conditions:

$$p_{\mathrm{T}} \quad > \quad 400\,\mathrm{MeV} \tag{5.1}$$

With selected tracks clusters of tracks in z-impact parameters are searched. For clusters of tracks the vertex fit is applied and vertex candidates are obtained by the iterative improvement of candidates by rejecting tracks. The primary vertex is selected according to the highest $\Sigma p_{\mathrm{T}}^2/N_{\mathrm{track}}$ where p_{T} is a transverse momentum of a track associated to the vertex and N_{track} is the number of tracks. The primary vertex is required to have more than four reconstructed tracks.

5.2.3   High p_{T} isolated lepton

Exactly one good lepton is required to pass the selection criteria described Section 4.2.2 and 4.3.2. The events that have any additional lepton with $p_{\mathrm{T}} > 15\,\mathrm{GeV}$ are rejected to reduce di-lepton events ($t\bar{t}$ di-lepton, $Z \to \ell\ell$, di-boson events etc). In this chapter distributions of physics quantities used in the selection of $t\bar{t}$ are shown for $t\bar{t}$ signal events simulated by ALPGEN (red histogram) and two major backgrounds, W+jets (green) and QCD (black), estimated with data sample (see Chapter 7 for details) after selecting exactly one high p_{T} isolated lepton. All histograms are normalized by dividing the total number of events,

In Figures 5.6(a)-5.6(d) distributions of transverse energy/momentum and pseudorapidity of leptons (electrons/muons) are shown for signal and backgrounds. Distributions of $E_{\mathrm{T}}/p_{\mathrm{T}}$ for $t\bar{t}$ signal events are very similar to those of W+jets backgrounds. On the other hand leptons from $t\bar{t}$ signals are produced in the central pseudorapidity region compared to those from backgrounds.

5.2.4   Lepton and trigger coincidence

The reconstructed lepton is matched to the trigger lepton. The objects that fired the trigger are recorded as trigger objects with their four momentum at each level of trigger system. Here it make sure that the selected lepton is triggered object or not.

5.2.5   Jet and calorimeter energy deposition

Reject events that have any bad jets that are not associated to real energy deposits in the calorimeters but arise from hardware problems, non-collision backgrounds or cosmic-ray showers which make the resolution of missing transverse energy worse.

5.2.6   Number of jets

At least four jets passing the jet selection described Section 4.4.2. Distributions of transverse momentum of the first and the fourth leading jet are shown in Figure 5.7(a) and 5.7(b). The p_{T} spectrum of the fourth leading jet of $t\bar{t}$ event is slightly harder than that of the backgrounds. Also the jet multiplicity is shown in Figure 5.7(c). It can be seen that the jet multiplicity of $t\bar{t}$ event is significantly higher than that of W+jets and fake lepton events.

5.2.7   Large missing transverse energy

Neutrino from the W boson decay produces large missing transverse energy. For the selection of the signal events of lepton+jet channel decay of $t\bar{t}$ the missing transverse energy, $E_{\mathrm{T}}^{\mathrm{miss}}$, of the event is required to be larger than $30\,\mathrm{GeV}$. The distribution of $E_{\mathrm{T}}^{\mathrm{miss}}$ of the selected events is shown in Figure 5.8. Processes, $t\bar{t}$ and W+jets, include W boson in the final states and its leptonic decay makes their $E_{\mathrm{T}}^{\mathrm{miss}}$ larger than that of fake lepton events.

5.2.8   Transverse mass of lepton and missing transverse energy

The transverse mass, m_{T}, calculated from the charged lepton and the missing transverse energy originate from the leptonic decay of W boson has a peak around the W boson mass. For the
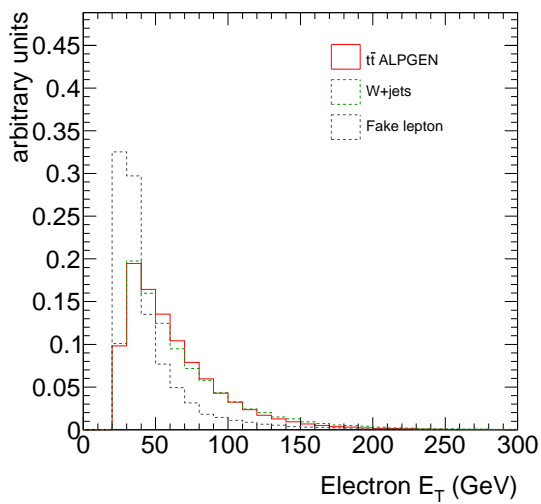
(a) Electron E_{T}
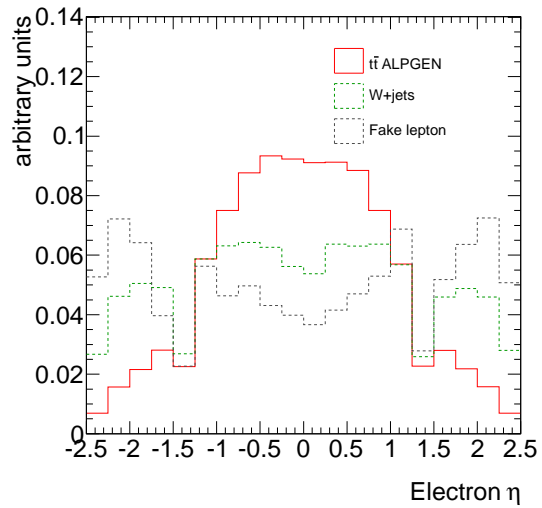
(b) Electron η
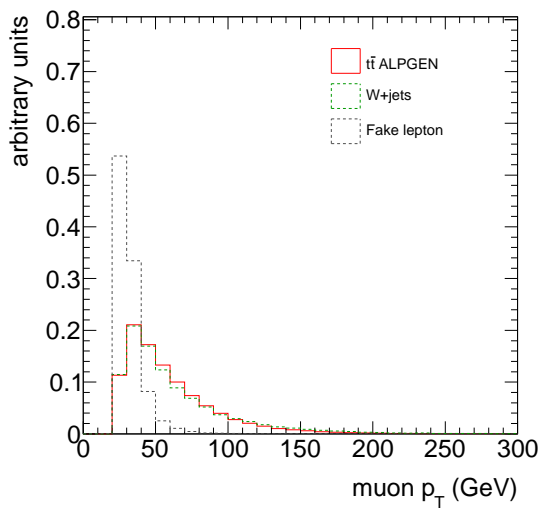
(c) Muonp_{T}
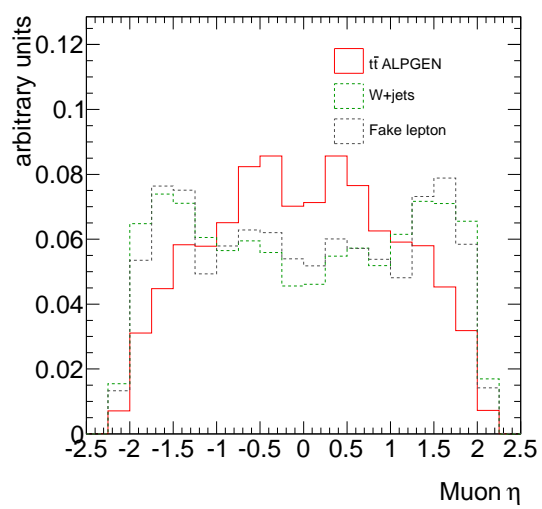
(d) Muon η

Figure 5.6: The basic kinematic variables that are used in the event selection based on discrimination between $t\bar{t}$ and background (W+jets and Fake lepton).
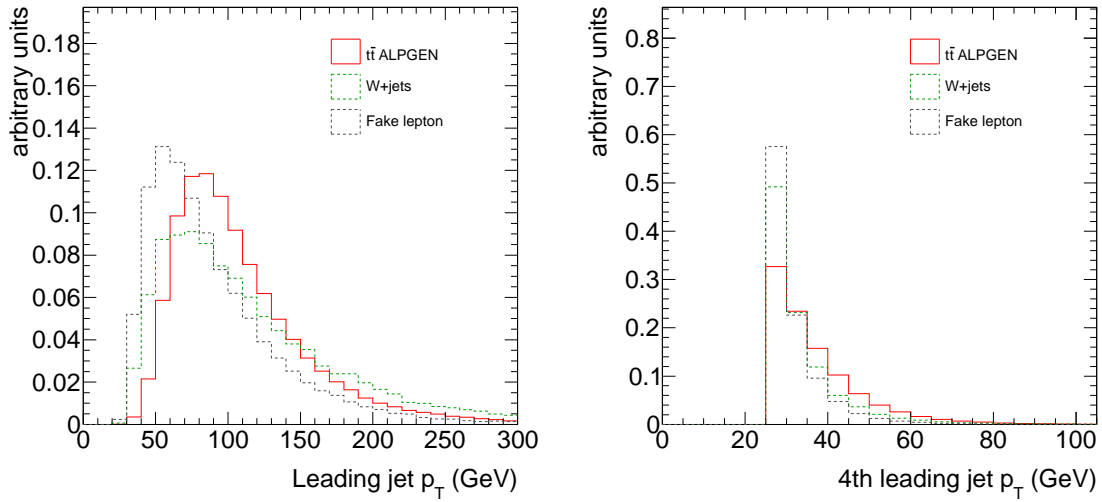
(a) 1st leading jet p_T

(b) 4th leading jet p_T
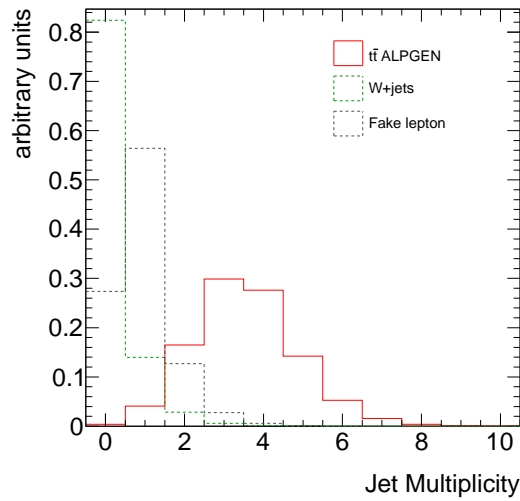
(c) Jet multiplicity

Figure 5.7: The basic kinematic variables that are used in the event selection based on discrimination between $t\bar{t}$ and background (W+jets and Fake lepton).
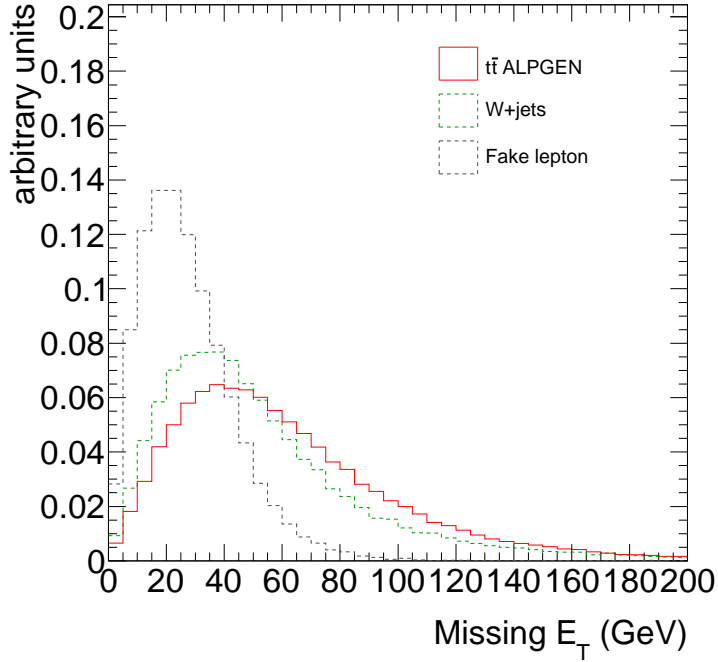
Figure 5.8: Missing E_{T}

leptonic W decay case the transverse mass, $m_{\mathrm{T}}(W)$, is defined as

$$m_{\mathrm{T}}(W) = \sqrt{2p_{\mathrm{T}}^{\ell}p_{\mathrm{T}}^{\nu}(1 - \cos(\phi^{\ell} - \phi^{\nu}))} \tag{5.2}$$

where p_{T}^{ℓ} denotes the transverse momentum of the charged lepton, p_{T}^{ν} denotes the transverse momentum of the neutrino, ϕ^{ℓ} and ϕ^{ν} are their azimuthal angles. The transverse mass from the charged lepton and the missing transverse energy is required to be larger than $35\,\mathrm{GeV}$. In Figure 5.9 the transverse mass distributions of $t\bar{t}$ signal and background processes, W+jets and QCD, are compared. For $t\bar{t}$ and W+jets which include the leptonic W boson decays peaks around the W boson mass are seen.

5.2.9 Number of tagged b-jet

The signal events include two b-quarks originate from the decays of the $t\bar{t}$ pair and are required to have at least one b-jet tagged by *MV1* b-tagger at the 70% efficiency working point. The distributions of the number of b-tagged jets for signal and background simulation samples are shown in Figure 5.10. Events of the $t\bar{t}$ signal has a larger number of tagged b-jets.
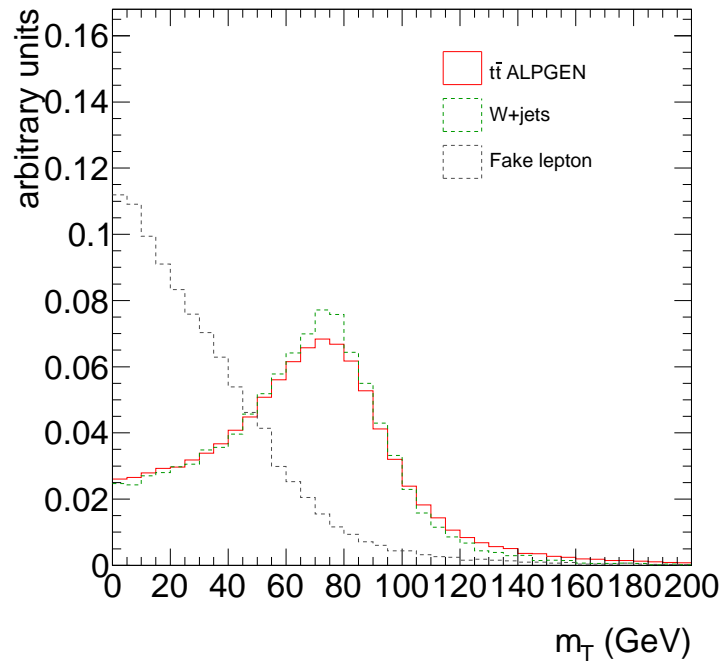
Figure 5.9: W transverse mass
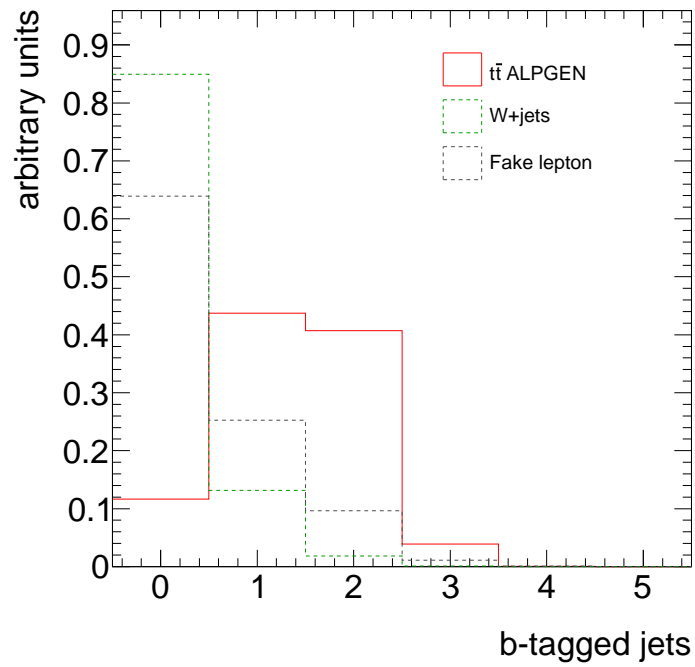
Figure 5.10: Number of b-tagged jets

60

Chapter 6

Top Quark Pair Reconstruction

For the measurement of the differential cross sections of the top quark pair production the kinematics of the final state, top and anti-top quarks, has to be reconstructed from observed objects, e, μ and $E_\mathrm{T}^\mathrm{miss}$, in the selected events. The full reconstruction of the $t\bar{t}$ kinematics is performed by a kinematic fit using likelihood function defined as a product of Breit-Wigner probability density functions and transfer functions. The Breit-Wigner distribution represents the mass distribution of decaying particle. The transfer function maps the measured energy (momentum) of an object to the energy (momentum) of the final state particle. By minimizing the likelihood true energies (momenta) of final state particles including neutrino are obtained with the constraint of Breit-Wigner mass distributions and energy (momentum) transfer functions. In this chapter the detailed procedure of the reconstruction of $t\bar{t}$ final states is described.

6.1   Kinematic Likelihood Fit

As already described in Section 1.2.2, the final state of lepton+jets channel has only one neutrino, hence the kinematics of the $t\bar{t}$ system can be reconstructed assuming that the observed $E_\mathrm{T}^\mathrm{miss}$ originates from one neutrino and the lepton and the neutrino are decay products of a W boson. The full reconstruction of $t\bar{t}$ events is based on a likelihood approach fitting with an emphasis on the non-Gaussian description of the energy resolution of the objects in the final state. Especially we consider $t\bar{t}$ lepton+jets channel for this analysis. In the final state of the lepton+jets, there are four quarks, a high transverse momentum lepton and missing transverse energy. The four quarks are detected as exactly four jets if no jet is lost due to outside of the detector acceptance region or does not pass the selection criteria and if there is no initial or final state radiation (ISR/FSR). In this case there are 24 possible jet permutations for which jets can be associated with quarks in the final state. Since two quarks come from the decay of one of the W bosons, they can not distinguish and only 12 permutations remain. All the permutation could be a combinatorial background except for the correct permutation. This definition also includes permutations which not only come from the four final state quarks but also from ISR/FSR. The likelihood function

is defined as

$$
\begin{aligned}
L \;=\; & BW\{m(q_1 q_2)|M_W, \Gamma_W\} \cdot BW\{m(\ell\nu)|M_W, \Gamma_W\} \cdot \\
& BW\{m(q_1 q_2 b_{\mathrm{had}})|M_t, \Gamma_t\} \cdot BW\{m(\ell\nu b_{\mathrm{had}})|M_t, \Gamma_t\} \cdot \\
& TF(\tilde{E}_{j_1}|E_{b_{\mathrm{had}}}) \cdot TF(\tilde{E}_{j_2}|E_{b_{\mathrm{lep}}}) \cdot TF(\tilde{E}_{j_3}|E_{q_1}) \cdot TF(\tilde{E}_{j_4}|E_{q_2}) \cdot \\
& TF(\tilde{E}_{\mathrm{x}}^{\mathrm{miss}}|p_x^\nu) \cdot TF(\tilde{E}_{\mathrm{y}}^{\mathrm{miss}}|p_y^\nu) \cdot
\begin{cases}
TF(\tilde{E}_\ell|E_\ell) & \text{electron channel} \\
TF(\tilde{p}_{\mathrm{T},\ell}|p_{T,\ell}) & \text{muon channel}
\end{cases}
\end{aligned}
\tag{6.1}
$$

where $BW\{m|M,\Gamma\}$ is the Breit-Wigner probability density function centered around mass M with decay width, Γ, and m denotes invariant mass calculated from quarks or leptons. $TF(\tilde{x}|x)$ is also the probability density function called transfer function where $\tilde{x}$ is the measured energy and x is the true energy and maps the measured energy of the reconstructed object to the true final state particles. The transfer function of the neutrino can be defined as $TF(E_{x,y}^{\mathrm{miss}}|p_{x,y}^\nu)$ by using measured values only in the transverse direction. Parameters used in the kinematic fit are the energies of four quarks, E_i (4 parameters), the energy of the charged lepton, E_ℓ (1 parameter) and the momentum of the neutrino, $\vec{p}_\nu$ (3 parameters). Each parameter is varied within the range around the measured value which is listed below and the z-component of the neutrino momentum is a free parameter in the fit.

- $\max(0, \tilde{E}_i - 7\sqrt{\tilde{E}_i}) < E_i < \tilde{E}_i + 7\sqrt{\tilde{E}_i}$
- $\max(0, \tilde{E}_e - 2\sqrt{\tilde{E}_e}) < E_e < \tilde{E}_e + 7\sqrt{\tilde{E}_e}$
- $E_{x,y}^{\mathrm{miss}} < p_{x,y}^\nu < E_{x,y}^{\mathrm{miss}}$
- $-1000\,\mathrm{GeV} < p_z^\nu < 1000\,\mathrm{GeV}$

All permutations of jets assigned to quarks are tried because a priori assignments are impossible. The logarithmic likelihood, $\ln L$, is maximized by varying parameters for all permutations. If there are more than four jets in the event satisfying all requirements described Section 4.4.2, all subsets of four jets from the five leading jets (60 permutations) in the event are considered for the fit.

6.2 Breit-Wigner distribution

The Breit-Wigner probability distribution function in eq. (6.1) is used to constrain invariant masses of decay particles to the mass of their mother particle. The normalized relativistic Breit-Wigner function is written as

$$
BW(m|M,\Gamma) = \frac{2}{\pi} \frac{\Gamma M^2}{(m^2 - M^2)^2 + \Gamma^2 M^2}
\tag{6.2}
$$

where m is an invariant mass of decay particles and M and Γ are decay parameters, mass and decay width, of the mother particle. For the decays of W bosons $M_W = 80.4\,\mathrm{GeV}/c^2$ and $\Gamma_W = 2.1\,\mathrm{GeV}$ [3] are used and for the decay of top quark $M_t = 172.5$ GeV and $\Gamma_t = 1.5$ GeV are used. The shape of the Breit-Wigner probability distribution functions are shown in Figures 6.1(a) and 6.1(b) for the decays of W boson and top quark, respectively
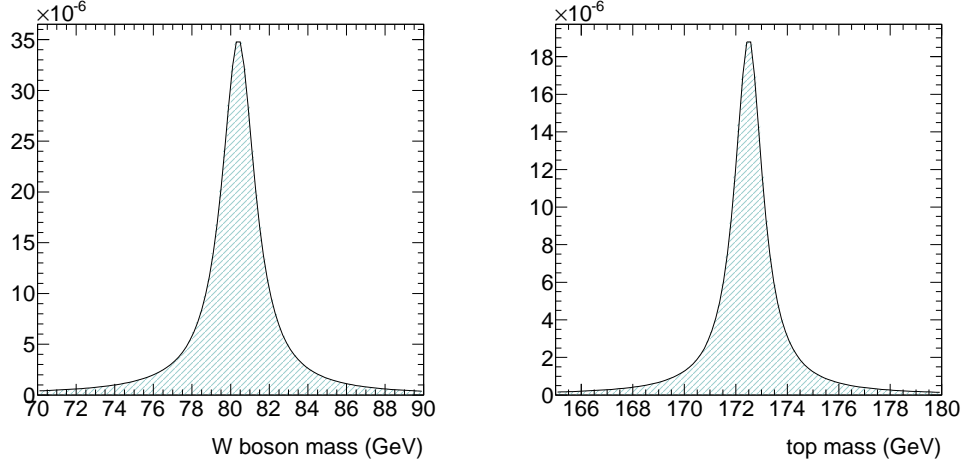
(a) Breit-Wigner distribution for W boson   (b) Breit-Wigner distribution for top quark

Figure 6.1: Breit-Wigner probability density function used in eq. (6.1).

6.3 Transfer Function

The transfer functions used in the likelihood function (6.1) represent the probability of observing a particle generated with energy, E_{true}, as an object with energy, E_{measured}. Transfer functions for jets, a charged lepton and a missing transverse energy are derived using Monte Carlo samples described in Section 2.3. In order to take account of a detector response the transfer function is parametrized with double Gaussian function form:

$$TF(\Delta E) = \frac{1}{\sqrt{2\pi}(p_2 + p_3 p_5)} \left[\exp\left\{ -\frac{(\Delta E - p_1)^2}{2p_2^2} \right\} + p_3 \exp\left\{ -\frac{(\Delta E - p_4)^2}{2p_5^2} \right\} \right] \qquad (6.3)$$

where ΔE is defined as

$$\Delta E = \frac{E_{\text{true}} - E_{\text{measured}}}{E_{\text{true}}}. \qquad (6.4)$$

For parameters in eq. (6.3), p_i their dependence on true energies, E_{true}, is parametrized as follows. The energy dependence of p_2 is written as

$$p_2 = \frac{a_2}{\sqrt{E_{\text{truth}}}} + b_2 \qquad (6.5)$$

and those of other parameters, p_i are parametrized as

$$p_i = a_i + b_i E_{\text{truth}}. \qquad (6.6)$$

Parameters, p_i, in eq. (6.1) and those in the energy dependence, a_i and b_i, are derived from the distributions of relative energy difference, ΔE, obtained with simulation samples as shown in Figure 6.2. First p_i's are obtained by fitting eq. (6.3) to ΔE distributions at several energy

63
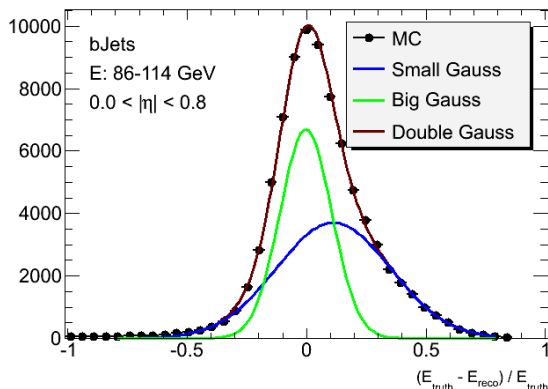
Figure 6.2: Relative difference of b-jet energy obtained from $t\bar{t}$ Monte Carlo sample. The energy region is $86 < E_b^{\text{truth}} < 114$ GeV and the pseudorapidity region is $0.0 < |\eta| < 0.8$. The deviation of relative energy difference is evaluated with two components of Gaussian shown in eq. (6.3). The global fit result is taken as Transfer Function.

Table 6.1: Parameters of Transfer Functions for electron and light jets. The η region is $0.0 < |\eta| < 0.80$ for both.

p_i	Electron		light jet	
	a_i	b_i	a_i	b_i
p_1	0.0047708	-8.31776×10^{-6}	-0.00887444	3.8949×10^{-6}
p_2	0.0551261	1.35272×10^{-2}	0.71723	5.57158×10^{-2}
p_3	0.0344012	8.1357×10^{-5}	0.277892	-4.58276×10^{-4}
p_4	0.0546478	-1.01212×10^{-4}	-0.0342356	5.2632×10^{-4}
p_5	0.0591536	5.04773×10^{-5}	0.256602	-3.81878×10^{-5}

regions of E_{true}. Then a_i and b_i are obtained by fitting eqs. (6.5-6.6) to the energy dependence of p_i's. Table 6.1 shows the determined values of a_i and b_i for electrons and light quark jets. The parametrized transfer function for light jets for the η region of $0.0 < |\eta| < 0.80$ is shown in Figure 6.3 for some sample true energy jet energies.

6.4 Likelihood Cut

After the reconstruction of the $t\bar{t}$ final state it is still necessary to remove badly reconstructed events by using the maximized value of $\ln L$, $(\ln L)_{\text{max}}$. Figure 6.4 shows the distributions of $(\ln L)_{\text{max}}$ of the event for e+jets and μ+jets channels separately. Both include plots for real data and histograms for simulation samples, $t\bar{t}$ signal and backgrounds. The sum of histograms for simulation samples reproduces the plots for data well.

64
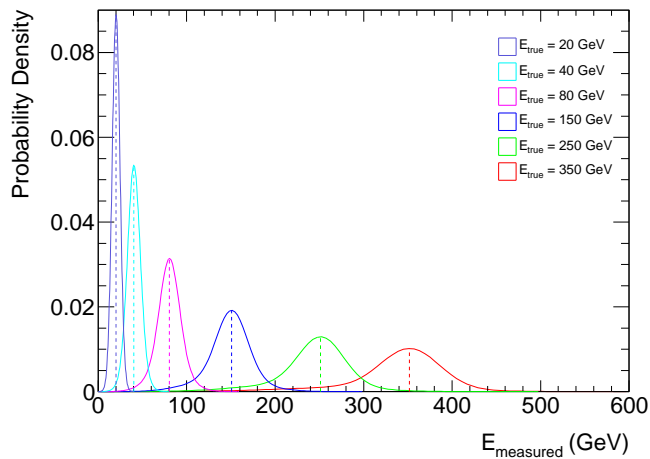
Figure 6.3: The parametrized transfer function for light jet. The truth energy of $E_{\text{true}} = 20$, 40, 80, 150, 250 and 350 GeV are shown respectively. The η region is $0.0 < |\eta| < 0.80$.
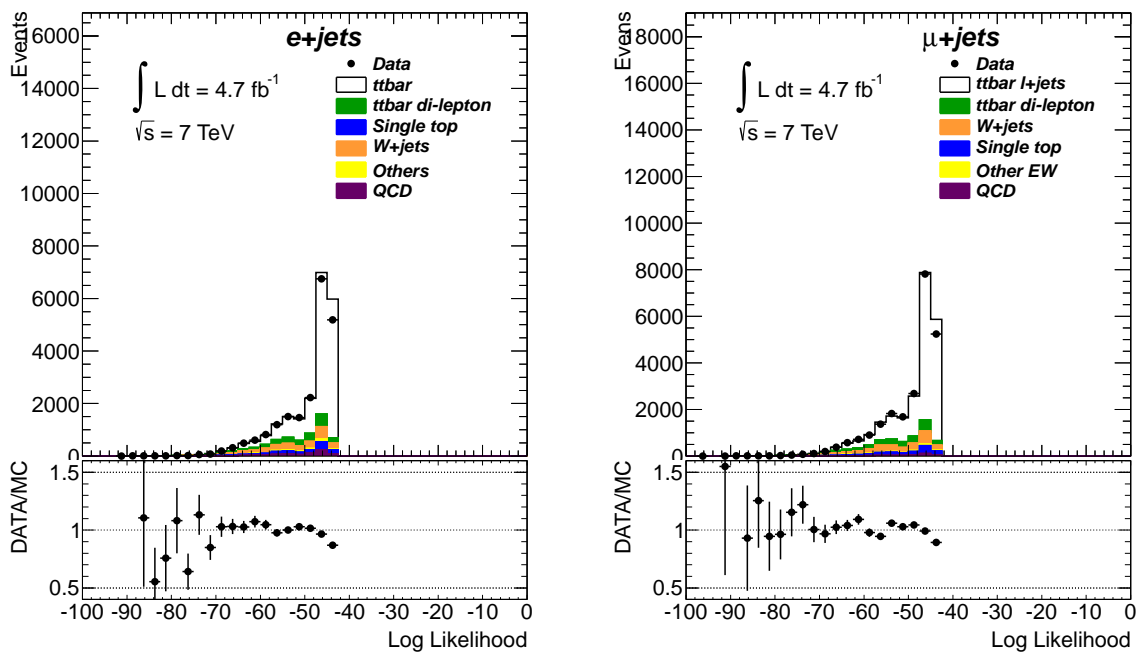
Figure 6.4: Log Likelihood value ($\ln L$). They are filled only maximum likelihood value.

65

In order to separate badly reconstructed events from other correctly reconstructed events we study the correlation between $(\ln L)_{\max}$ and the reconstructed $t\bar{t}$ invariant mass for the events of the $t\bar{t}$ signal sample. First the ratio of the displacement of the reconstructed $t\bar{t}$ invariant mass and its generated true value is defined for the simulated $t\bar{t}$ signal sample as:

$$r_{t\bar{t}} = \frac{m_{t\bar{t}}^{\mathrm{rec}} - m_{t\bar{t}}^{\mathrm{true}}}{m_{t\bar{t}}^{\mathrm{true}}} \tag{6.7}$$

Plots in Figure 6.5 show the correlation between the value of $(\ln L)_{\max}$ and the generated $t\bar{t}$ true invariant mass for the events of the e+jets channel of the $t\bar{t}$ MC sample. The plot in Figure 6.5(a) shows the correlation for the events with $|r_{t\bar{t}}| < 0.5$ and that in Figure 6.5(b) shows the correlation for the events with $|r_{t\bar{t}}| > 0.5$. When the displacement of the reconstructed $t\bar{t}$ invariant mass becomes large, the large fraction of events have small $\ln L$ values. In order to enhance the fraction of correctly reconstructed events we apply a cut on $(\ln L)_{\max}$ at -52:

$$(\ln L)_{\max} > -52. \tag{6.8}$$

In Figure 6.5(b) there is a cluster of badly reconstructed events at the lower $(\ln L)_{\max}$ region.
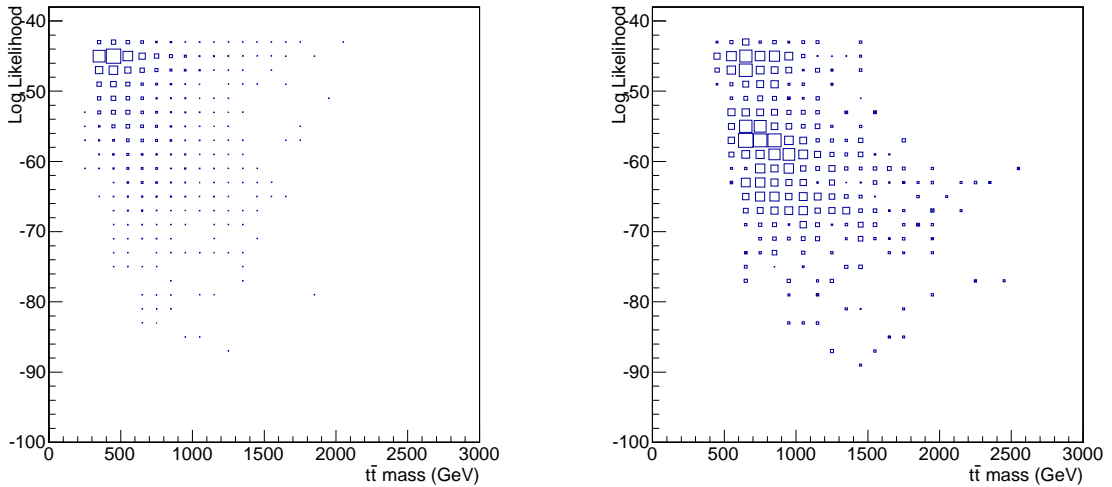
(a) Events with $|r_{t\bar{t}}| < 0.5\%$ of the electron channel.   (b) Events with $|r_{t\bar{t}}| > 0.5\%$ of the electron channel.

Figure 6.5: The correlation between the reconstructed $t\bar{t}$ invariant mass and the maximized log likelihood for events of the electron channel. Figure 6.5(a) shows the plot for events with $|r_{t\bar{t}}| < 0.5$ and Figure 6.5(b) shows that for events with $|r_{t\bar{t}}| > 0.5$

We further study the correlation of other two variable which represent the accuracy of the reconstruction with $(\ln L)_{\max}$. They are the displacements of the direction, $\Delta R_{\mathrm{reco,true}}$, and the energy, $\Delta E_{\mathrm{reco,true}}$, of the reconstructed objects from the true values. The definition of $\Delta R_{\mathrm{reco,true}}$

is

$$\Delta R_{\text{reco,true}} = \sqrt{(\phi_{\text{reco}} - \phi_{\text{true}})^2 + (\eta_{\text{reco}} - \eta_{\text{true}})^2} \qquad (6.9)$$

where η's are pseudorapidities and ϕ's are azimuthal angles. The subscript "reco" denotes the reconstructed value and "true" denotes the generated true value. The definition of $\Delta E_{\text{reco,true}}$ is

$$\Delta E_{\text{reco,true}} = E_{\text{reco}} - E_{\text{true}} \qquad (6.10)$$

where E represents energies or momenta of the reconstructed objects and the subscripts have the same meaning as $\Delta R_{\text{reco,true}}$.

Plots in Figure 6.6 show the correlation between $\Delta R_{\text{reco,true}}$ and $(\ln L)_{\text{max}}$ for the reconstructed electrons, neutrinos and light flavor jets. From these plots it is clear that the cut of $(\ln L)_{\text{max}} > -52$ enhances events with smaller $\Delta R_{\text{reco,true}}$. The direction of electrons is well reconstructed and match to the true direction within $\Delta R_{\text{reco,true}} < 0.1$. The direction of jets are also reconstructed within $\Delta R_{\text{reco,true}} < 0.3$. Even for neutrinos the cut of $(\ln L)_{\text{max}} > -52$ enhances the correctly reconstructed ones. Plots in Figure 6.7 show the correlation between

(a) $\Delta R_{\text{reco,true}}$ for electrons　　(b) $\Delta R_{\text{reco,true}}$ for neutrinos　　(c) $\Delta R_{\text{reco,true}}$ for light quark jets
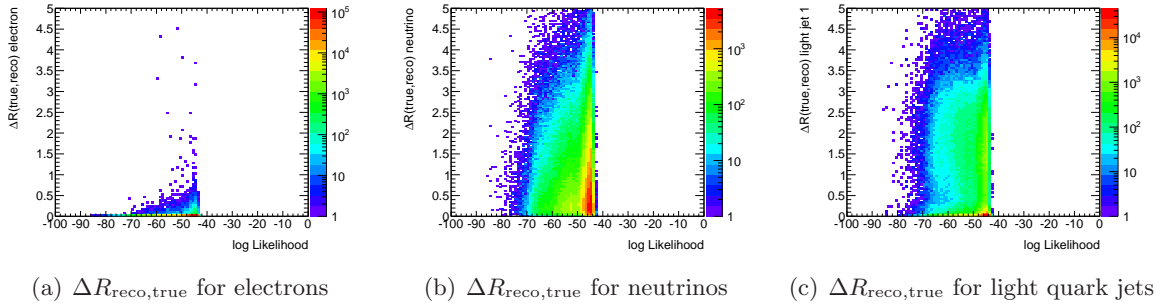
Figure 6.6: The correlation of the displacement of directions, $\Delta R_{\text{reco,true}}$ between true particles (electron, neutrino, light quarks) and their reconstructed objects and $(\ln L)_{\text{max}}$. Permutation of jets obtained from kinematic fitting which correspond to maximum likelihood value.

$\Delta E_{\text{reco,true}}$ and $(\ln L)_{\text{max}}$ for electrons, neutrinos and light flavor jets. Again they show that the cut of $(\ln L)_{\text{max}} > -52$ enhances the correctly reconstructed events.

(a) $\Delta E_{\mathrm{reco,true}}$ for electrons (b) $\Delta p_{\mathrm{x,reco,true}}$ for neutrinos (c) $\Delta E_{\mathrm{reco,true}}$ for light quark jets
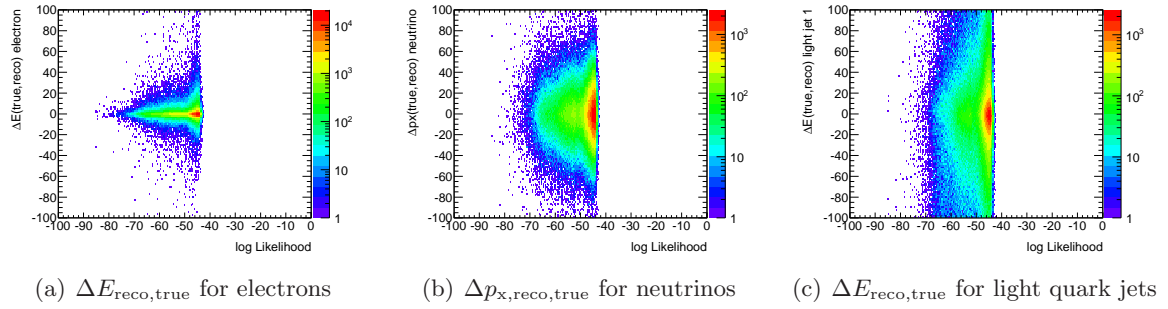
Figure 6.7: The correlation of the displacement of energies, $\Delta E_{\mathrm{reco,true}}$, between true particles (electron, neutrino, light quarks) and their corresponding reconstructed objects. Energy of each object and permutation of jets obtained from kinematic fitting which correspond to maximum likelihood value.

Chapter 7

Background Estimation

The estimations of contamination of background processes in the selected $t\bar{t}$ signal candidate events are described in this chapter. The contaminations of W+jets and QCD multi-jet background events are estimated based on data drive method. Those of other background processes, Z+jets, di-boson single top and $t\bar{t}$ di-lepton channel, are based on the simulated samples.

7.1 W+jets

7.1.1 W+jets **normalization**

We estimate the W+jets background based on the data driven method. The shapes of distributions of kinematic variables and the acceptance of events are estimated by using simulated samples. However, the overall normalization of the background process and the heavy flavor composition are not well modeled especially multi-jet production associated to W boson in the Monte Carlo simulation. "Charge asymmetry method" is used to extract the overall normalization of the background.

At a proton-proton collider like the LHC, there is an overall charge asymmetry in the production of W boson due to differences of the quark and anti-quark parton distribution functions in a proton. The W^+ boson is produced by collisions such as $u\bar{d} \rightarrow W^+$ or $c\bar{s} \rightarrow W^+$ in the leading order and its production cross section depends on the product of PDFs like $u(x_1)\,\bar{d}(x_2)$. On the other hand the cross sections of the production processes of the W^- boson such as $d\bar{u} \rightarrow W^-$ or $s\bar{c} \rightarrow W^-$ depend on the product of PDFs like $d(x_1)\,\bar{u}(x_2)$. Since $u(x)$ is always larger than $d(x)$, there is a charge asymmetry in the W boson productions, hence the charges of leptons from the W boson decay becomes asymmetric, too. The background from W+jets productions is estimated by the following formula:

$$N_{W^+} + N_{W^-} = \frac{N_{W^+}^{\mathrm{MC}} + N_{W^-}^{\mathrm{MC}}}{N_{W^+}^{\mathrm{MC}} - N_{W^-}^{\mathrm{MC}}}(D^+ - D^-) = \left(\frac{r_{\mathrm{MC}}+1}{r_{\mathrm{MC}}-1}\right)(D^+ - D^-) \qquad (7.1)$$

where D^+ and D^- are the total number of selected events of real data with a positively and a negatively charged lepton respectively and r_{MC} denotes the ratio of the production cross sections

of W^+ to that of W^-:

$$r_{\mathrm{MC}} \equiv \frac{\sigma(pp \to W^+)}{\sigma(pp \to W^-)} = \frac{N_{W^+}}{N_{W^0}} \tag{7.2}$$

where N_{W^+} and N_{W^-} are the number of selected events of simulation samples with a positively and a negatively charged lepton respectively. The approximation $N_{W^+} - N_{W^-} \simeq D^+ - D^-$ can be realized since the process $t\bar{t}$, QCD multi-jet background, Z+jets and di-boson productions are charge symmetric. Smaller sources of charge asymmetry in the real data are mostly come from single top production. These further contributions of charge asymmetric processes are estimated by Monte Carlo simulation and subtracted from eq. (7.1). The normalization scale factors of the W+jets Monte Carlo simulation samples which extracted by eq. (7.1) are summarized in Table 7.1.

Table 7.1: The scale factors of the W+jets normalization

No. of jets	Electron	Muon
1 jet	$0.972^{+0.262}_{-0.253}$	$0.998^{+0.220}_{-0.210}$
2 jet	$0.883^{+0.150}_{-0.150}$	$0.919^{+0.092}_{-0.092}$
3 jet	$0.799^{+0.160}_{-0.152}$	$0.832^{+0.133}_{-0.125}$
4 jet	$0.823^{+0.156}_{-0.156}$	$0.889^{+0.142}_{-0.133}$
≥ 5 jet	$0.836^{+0.192}_{-0.184}$	$0.824^{+0.132}_{-0.148}$

7.1.2 W+heavy flavor normalization

In order to improve the estimation of background contaminations from W+jets processes the flavor components of jets should be estimated because p_{T} and η of background leptons should differ depending on their flavor components. In this section the method to determine the flavor components of jets associated with W production is described. In the real data the W+jets events are obtained by subtracting QCD multi-jet background events estimated by data driven method (Section 7.2) and all non-W contribution estimated by Monte Carlo simulation given by

$$N^W = N_{\mathrm{data}} - N_{\mathrm{QCD}} - N_{\mathrm{MC}} \tag{7.3}$$

where N_{MC} is the sum of the number of events from Z+jets, di-boson, single top and $t\bar{t}$ processes.

The quantities F_{bb}, F_{cc}, F_c and F_{light} represent the flavor fractions of the N_{bb}^{pretag}, N_{cc}^{pretag}, N_c^{pretag} and N_{light}^{pretag} events respectively. For each jet multiplicity i, the relation between the tagged and pretagged number of events can be written by

$$N_i^{W,tag} = N_i^{W,pretag} \left(F_{bb,i}P_{bb,i} + F_{cc,i}P_{cc,i} + F_{c,i}P_{c,i} + F_{light,i}P_{light,i} \right) \tag{7.4}$$

70

Table 7.2: W+jets flavor fraction scale factor for events of $W + bb$, $W + c$ and W+light jet.

Channel	K_{bb}/K_{cc}	K_c	K_{light}
Electron	$1.41^{+0.31}_{-0.39}$	$0.73^{+0.39}_{-0.35}$	1.00 ± 0.09
Muon	1.24 ± 0.34	$0.98^{+0.37}_{-0.31}$	$0.97^{+0.07}_{-0.08}$

where $P_{xx,i}$ with $xx = bb, cc, c, light$ represent the b-tagging probabilities for each flavor type of jets and are obtained from Monte Carlo simulation. For each jet multiplicity i, the flavor fractions add up to unity:

$$F_{bb,i} + F_{cc,i} + F_{c,i} + F_{light,i} = 1 \tag{7.5}$$

Using eq. (7.4) of 2-jet tagged events, which is dominated W+jets events, split into two sub-samples of negative and positive prompt lepton, eq. (7.5) for 2-jet pretagged events and combining the cc and bb fractions gives the three unknown flavor fractions, $F^{data}_{bb,2}$, $F^{data}_{c,2}$ and $F^{data}_{light,2}$, that we want to measure from data. F_{cc} is replaced to $k_{cctobb}F_{bb}$ where k_{cctobb} is the ratio between the cc and the bb fractions taken from Monte Carlo. For pretagged events with 2-jets in the final state, eq. (7.5) can be written as

$$F_{bb,2} + k_{cctobb}F_{bb,2} + F_{c,2} + F_{light,2} = 1 \tag{7.6}$$

For tagged events with 2-jets in the final state, eq. (7.5) can be written as

$$N_2^{W,tag\pm} = N_2^{W,pretag\pm}(F_{bb,2}P_{bb,2} + k_{cctobb}F_{bb,2}P_{cc,2} + F_{c,2}P_{c,2} + F_{light,2}P_{light,2}) \tag{7.7}$$

The use of charge asymmetry is denoted as superscript of "$\pm$". The fractions F_{bb}, F_c and F_{light} are determined to require the number of tagged events in Monte Carlo should be equal to data for events with positive and negative lepton, and unity of eq. (7.6). Finally the flavor scale factors $K_{xx,i}$ are defined as the ratio between the flavor fractions in data and those in Monte Carlo simulation:

$$K_{xx,i} = \frac{F^{data}_{xx,i}}{F^{MC}_{xx,i}} \tag{7.8}$$

The determined flavor fraction scale factor is shown in Table 7.2. These are applied to all W+jets Monte Carlo sample according to their true jet flavor.

7.2 QCD Multi-Jet Background Event

The $t\bar{t}$ signal events of the lepton+jets channel are identified by a high transverse momentum lepton in the final state. The lepton is required to fire an appropriate event trigger and to pass through the event selections. Even without including vector bosons, W/Z, which can decay leptonically, in the final state there are some possibilities to observe a high transverse momentum lepton which pass through the requirements of the $t\bar{t}$ lepton+jet channel. The dominant sources of leptons are:

- semi-leptonic decays of b-jets,

- long lived weakly decaying particles such as $\pi^{\pm}$ or K mesons,

- mis-identifications of electromagnetic showers produced by π^0 decays as electrons, and

- mis-identifications of direct photons as electrons due to conversions.

Events with leptons from these processes are denoted as QCD multi-jet background events in total. Although the probability of events with such a lepton passing the event selection criteria is small, the production cross section for QCD multi-jet events is orders of magnitude larger than that of $t\bar{t}$ signal. Since these processes depend on the details of the detector materials, it is rather difficult to simulate such low probability phenomena precisely by the detector simulation program. We exploit the real data to estimate the rate of the QCD multi-jet background events and the efficiency of the signal leptons passing the event selection.

We used a matrix method to estimate the QCD multi-jet background event. The matrix method is based on two different categories of events defined by changing requirements to leptons; loose and tight. They have different efficiencies for high p_{T} signal leptons, coming from W/Z decays and different rates for background leptons. Using these two samples, the rate of backgrounds in events selected with tight lepton requirements are estimated. In the analysis of the lepton+jets channel the number of total events which contain one loose lepton can be written as

$$N^{\mathrm{loose}} = N^{\mathrm{loose}}_{\mathrm{signal}} + N^{\mathrm{loose}}_{\mathrm{bg}} \tag{7.9}$$

where $N^{\mathrm{loose}}_{\mathrm{signal}}$ and $N^{\mathrm{loose}}_{\mathrm{bg}}$ are the number of events containing signal and background leptons which pass the loose requirements for leptons. The number of events after applying tight lepton selection can be written as

$$N^{\mathrm{tight}} = N^{\mathrm{loose}}_{\mathrm{signal}} \times \epsilon_{\mathrm{signal}} + N^{\mathrm{loose}}_{\mathrm{bg}} \times \epsilon_{\mathrm{bg}} \tag{7.10}$$

where $\epsilon_{\mathrm{signal}}$ and ϵ_{bg} are the efficiencies of tight lepton requirements to loose lepton requirements for signal and background leptons, respectively, and are defined as:

$$\epsilon_{\mathrm{signal}} = \frac{N^{\mathrm{tight}}_{\mathrm{signal}}}{N^{\mathrm{loose}}_{\mathrm{signal}}}, \qquad \epsilon_{\mathrm{bg}} = \frac{N^{\mathrm{tight}}_{\mathrm{bg}}}{N^{\mathrm{loose}}_{\mathrm{bg}}} \tag{7.11}$$

where $N^{\mathrm{tight}}_{\mathrm{signal}}$ and $N^{\mathrm{tight}}_{\mathrm{bg}}$ are the number of events containing signal and background leptons which pass the tight requirements for leptons. From (7.9) and (7.10) the number of events with background leptons which pass the tight lepton requirements, $N^{\mathrm{tight}}_{\mathrm{bg}}$, is expressed as

$$N^{\mathrm{tight}}_{\mathrm{bg}} = \frac{\epsilon_{\mathrm{bg}}}{\epsilon_{\mathrm{signal}} - \epsilon_{\mathrm{bg}}} \left(N^{\mathrm{loose}} \times \epsilon_{\mathrm{signal}} - N^{\mathrm{tight}} \right) \tag{7.12}$$

which can be evaluated when the efficiencies of tight lepton requirements for signal and background leptons, $\epsilon_{\mathrm{signal}}$ and ϵ_{bg}, are estimated. This estimation method is validated only in case of the ϵ_{bg} and $\epsilon_{\mathrm{signal}}$ are significantly different. The efficiency of signal leptons, $\epsilon_{\mathrm{signal}}$, is estimated by the *tag & probe* method using the Z boson decays into two leptons. The efficiency of background leptons is estimated from the control regions where the contribution of background leptons is significantly higher. The estimation of both efficiencies are described from the next Section 7.2.1.

7.2.1 Tight Selection Efficiencies for Electrons

7.2.1.1 Signal Electron Efficiency

The measurement of signal electron selection efficiency, ϵ_{signal}, is derived through the *Tag & Probe* method with the sample of $Z \to ee$ events selected from collision data. The signal lepton efficiency ϵ_{signal} is equivalent to the fraction of loose probe electrons passing the tight requirements. The tight electron selection is the same as described in Section 4.2.2 without the cut on E_{T}. The loose electron selection for the background estimation is equivalent to the medium criteria of electron identification described 4.2.2. The events for the estimation are required to have two loose electrons and fire an appropriate trigger (See Section 5.1.1). The tag electron which passes the tight selection is required to match to the object that fire the trigger in order to avoid bias due to the trigger identification requirements on the probe efficiencies. The other electron becomes the probe. The invariant mass of these pair of electron is calculated but pairs of same-sign (SS) and opposite-sign (OS) are considered separately. Different background subtraction methods are considered to extract the signal electron efficiency, ϵ_{signal}, from invariant mass distribution. The following methods have been considered:

- Removal of same-sign events from opposite-sign ones in the Z mass window. This assumes the lepton charges are uncorrelated in background events.

- Side-band method on same-sign events. The side-band method relies on the background having a linear shape over the considered invariant mass region. The invariant mass distributions for SS and OS pairs are divided in three regions A, B and C. The number of background events in region B, i.e. in Z mass window, are estimated from the extrapolation of the side-bands A and C of the same-sign distribution.

- Fit using a model for the signal (Breit-Wigner convoluted with a Crystal-ball function) and for the background components (convolution of a Gaussian and an exponential decay). Two fits need to be performed: one for the probe at loose selection level (denominator) and one for the probe at tight selection level (numerator). Both are shown in Figure 7.1. An extended maximum likelihood formalism on binned dataset is used. The efficiency is then calculated to take the ratio of the estimated number of signal events in the Z mass window in the two selections.

The main systematics on the efficiency measurements are the contamination to the probe sample by background. To estimate the uncertainty of background amount, some variations of the background estimation have been considered:

- The three different methods to extract the background described above

- Different Z mass window: [81-101], [76-106], [86-96] GeV for second method

- Different fit ranges: [60-120], [55-200] GeV for third method

The central value of the signal electron efficiency, ϵ_{signal}, is the average of these variations and its systematic uncertainty is given by the spread of all variations. The signal electron efficiency as a function of η and E_{T} is shown in Figure 7.2.
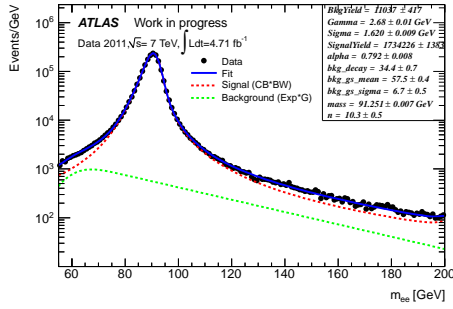
(a) Fit result at loose selection
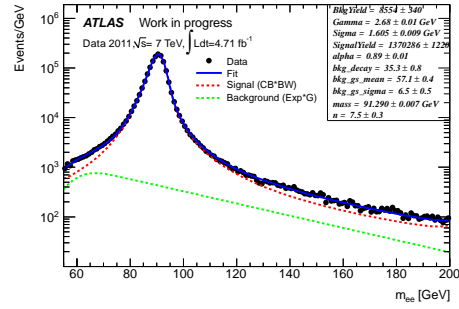
(b) Fit result at tight selection

Figure 7.1: Invariant mass distribution of opposite-sign charge electron pairs for loose selection and tight selection level after the fitting (blue dashed line) with the signal (red dashed line) and the background components (green dashed line). These plots are including whole η and E_T events.
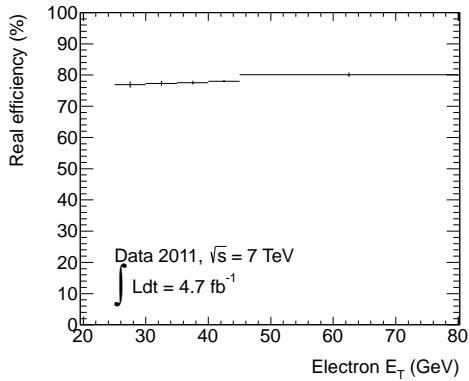
(a) Signal electron E_T
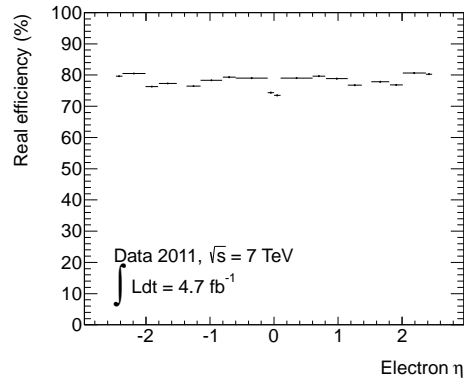
(b) Signal electron η

Figure 7.2: The signal electron efficiency ϵ_signal as a function of η and E_T. The error bar shows the total of statistical and systematic uncertainty.

7.2.1.2 Background Electron Efficiency

The background electron efficiency, ϵ_{bg}, is estimated using a sample which have at least one jet with $p_{\mathrm{T}} > 25\,\mathrm{GeV}$ and exactly one loose electron described in Section 7.2.1.1. A distance between the highest p_{T} jet and electron, $\Delta R(\mathrm{jet, electron}) > 0.7$ is required. The background electron rate, ϵ_{bg}, corresponds to the fraction of loose probe candidates passing the tight selection. It is measured in a control region of low missing transverse energy $E_{\mathrm{T}}^{\mathrm{miss}} < 20\,\mathrm{GeV}$ in order to enhance the background electron sample. The contamination of signal electron from W and Z boson decays in low missing transverse energy region is estimated based on Monte Carlo sample ($t\bar{t}$, single top, W/Z+jets and di-boson) and is subtracted from the number of observed loose and tight electron events in data. The systematic uncertainty is estimated to vary the region of missing transverse energy from 15 to 25 GeV. Since the background electrons come from various sources, their efficiencies are estimated according to their sources individually:

- Leptons from semi-leptonic decaying heavy flavor jets
  Events with at least one jet tagged as b-jet are used. This sub-sample is dominated by $b\bar{b}$ events and is enhanced electrons from b decays.

- Photon conversion
  Events that the electron is close to a conversion vertex are enhanced in conversion electrons. Figure 7.3 shows the conversion radius R in the barrel region for loose selection electron.
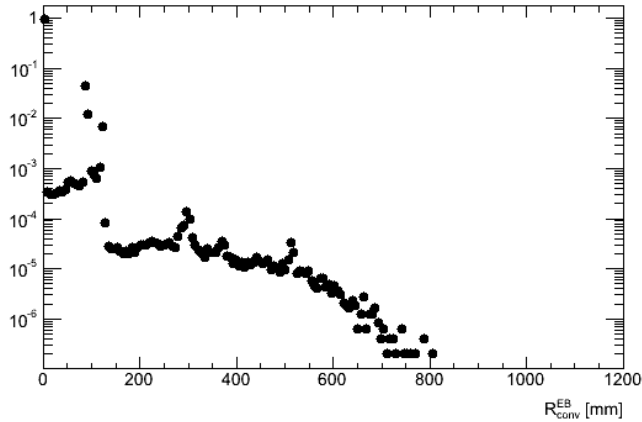
Figure 7.3: Photon conversion radius R in the barrel region for loose selection electrons with a conversion vertex.

- Misidentify light flavor jets as electron
  Events with leptons away from conversion vertices have a higher fraction of background electrons from light jets.

These background electron rates are combined as a function of background electron E_{T} and η as shown in Figure 7.4, and its central value is used for the estimation of QCD multi-jet background events in the signal region.

(a)   (b)
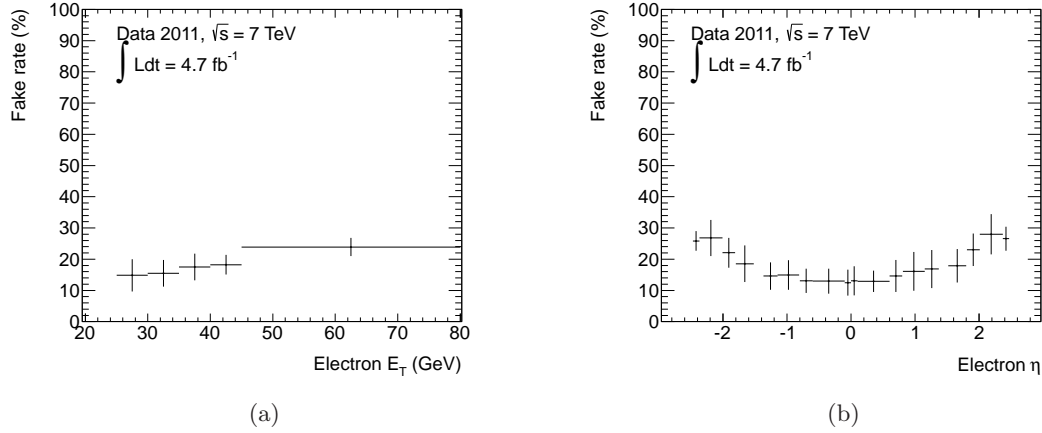
Figure 7.4: The combined background electron rate, ϵ_{bg}, as a function of electron η and E_{T}. The error bar shows the total of statistical and systematic uncertainty.

7.2.2 Tight Selection Efficiencies for Muons

There are two methods, matrix method A and B, for the estimation of QCD multi-jet background events in the analysis of the muon channel. Especially estimation of background muon rate are different between two methods. Matrix method A is based on low m_{T} control region and matrix method B is based on impact parameter significance. Signal muon efficiencies are determined by *Tag & Probe* method with sample of $Z \rightarrow \mu\mu$ events. Matrix method A uses the $Z \rightarrow \mu\mu$ sample from collision data but matrix method B used Monte Carlo sample. Average of two signal muon efficiencies and background muon rates are used for the estimation of QCD multi-jet background events. Details of two methods are described from the next subsections.

7.2.2.1 Signal Muon Efficiency by Matrix Method A

The signal muon efficiency, ϵ_{signal}, is determined by selecting di-muon pairs which invariant mass becomes the Z boson mass peak and applying *Tag & Probe* method. The loose sample selection criteria are the following:

- ≥ 1 jet with $p_{\text{T}} > 25\,\text{GeV}$ and $|\eta| \leq 2.5$

- ≥ 1 loose muon with $p_{\text{T}} > 20\,\text{GeV}$ and $|\eta| \leq 2.5$ where loose muon selection is identical to the Section 4.3.2 except for the muon isolation.

The tight muon selection requires in addition calorimeter and track isolation should be less than 4 GeVand 2.5 GeV respectively. The signal muon efficiencies, ϵ_{signal}, that pass loose selection criteria to pass the tight one for $Z \rightarrow \mu\mu$ events in data as function of leading jet transverse momentum $p_{\text{T,j1}}$ and muon η are shown in Figure 7.5.

76

(a) Leading jet $p_{\mathrm{T,j1}}$ (b) Muon η
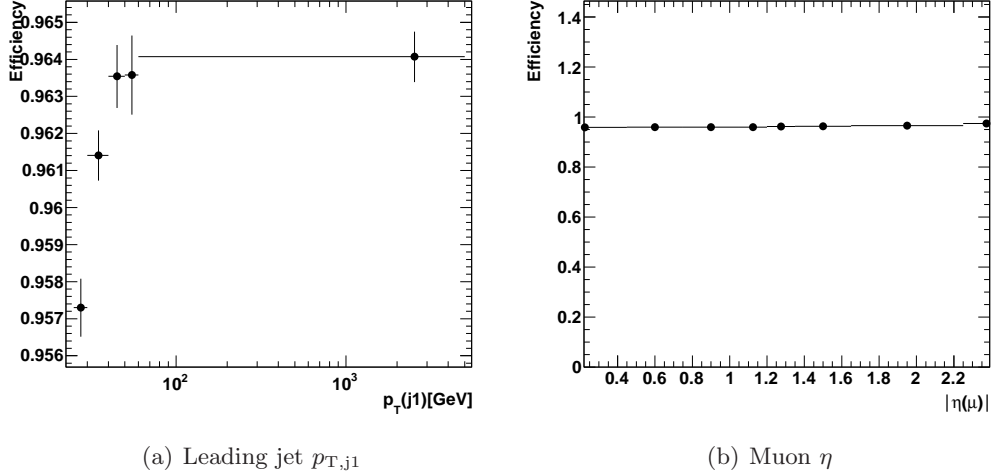
Figure 7.5: The signal muon efficiencies, $\epsilon_{\mathrm{signal}}$, as function of leading jet transverse momentum $p_{\mathrm{T,j1}}$ and η.

7.2.2.2 Background Muon Efficiency Estimated by Matrix Method A

The background muon efficiency, ϵ_{bg}, is determined by using two control regions of low transverse mass $m_{\mathrm{T}}(W)$. The samples which are applied the loose selection criteria and additional inverted cut:

sample 1 $m_{\mathrm{T}}(W) < 20\,\mathrm{GeV}$, $E_{\mathrm{T}}^{\mathrm{miss}} < 10\,\mathrm{GeV}$

sample 2 $E_{\mathrm{T}}^{\mathrm{miss}} + m_{\mathrm{T}}(W) < 60\,\mathrm{GeV}$

are used to obtain QCD multi-jet events dominated sample. Additionally the samples are required to have at least one b-tagged jet for determination of background muon efficiencies, ϵ_{bg}, in b-tagged region. Contamination from signal muons from W and Z decays is subtracted using Monte Carlo simulation. The background muon efficiencies corresponds to the fraction of number of events that passed loose and tight selection criteria. Obtained ϵ_{bg} using different control regions are in excellent agreement with each other. The combined results of ϵ_{bg} as function of muon η and leading jet transverse momentum $p_{\mathrm{T,j1}}$ are show in Figure 7.6.

7.2.2.3 Signal Muon Efficiency by Matrix Method B

The signal muon efficiency, $\epsilon_{\mathrm{signal}}$, is derived from the Monte Carlo sample of $Z \to \mu\mu$ events with *Tag & Probe* method. The loose and tight selection criteria are identical to matrix method A. At least one jet of selected jets is tagged as b-jet is also required to determine the signal muon efficiency, $\epsilon_{\mathrm{signal}}$, in b-tagged region. The fraction of number of events that passed loose and tight selection criteria corresponds to the signal muon efficiency. Determined signal muon

(a) Leading jet $p_{\mathrm{T,j1}}$

(b) muon η
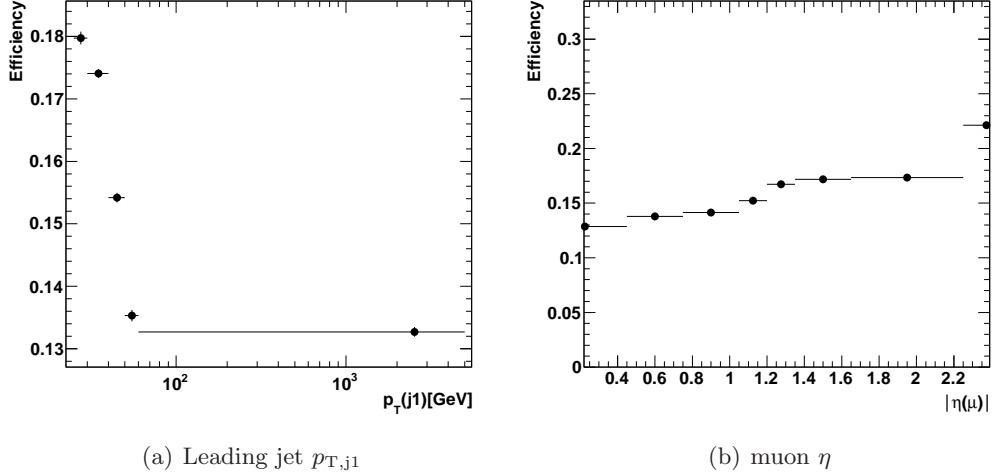
Figure 7.6: The background muon rates, ϵ_{bg}, for b-tagged sample as function of leading jet transverse momentum $p_{\mathrm{T,j1}}$ and η.

efficiency, $\epsilon_{\mathrm{signal}}$, according to jet multiplicity is shown in Table 7.3. The error shown in Table 7.3 is statistical only.

Table 7.3: The signal muon efficiencies, $\epsilon_{\mathrm{signal}}$, according to jet multiplicity. In this Table, "5-jets in." means for the event of 5-jets inclusive.

muon $|\eta|$	1-jet	2-jets	3-jets	4-jets	5-jets in.
0.0-2.5	0.968 ± 0.006	0.960 ± 0.008	0.953 ± 0.010	0.946 ± 0.012	0.935 ± 0.016

7.2.2.4 Background Muon Efficiency by Matrix Method B

Since the QCD multi-jet background to the top quark production in the muon+jets channel is expected to be dominated by heavy flavor jets. The background muon coming from heavy flavor decay usually has large impact parameter with respect to the primary vertex. Based on this characteristic, the background muon rates, ϵ_{bg}, are determined. The loose and tight selection criteria are identical to matrix method A. Additional inverted cut, $m_{\mathrm{T}}(W) < 20\,\mathrm{GeV}$ and $E_{\mathrm{T}}^{\mathrm{miss}} + m_{\mathrm{T}}(W) < 60\,\mathrm{GeV}$ are also applied to obtain QCD multi-jets dominated sample. By counting the tight and loose muons with signed impact parameter d_0 larger than a given threshold x, a loose-to-tight background muon efficiency, ϵ_{bg}, is defined as

$$\epsilon_{\mathrm{bg}}(x) = \frac{\sum_{d_0 > x} N^{\mathrm{tight}}}{\sum_{d_0 > x} N^{\mathrm{loose}}} \tag{7.13}$$

The background muon rates, ϵ_{bg}, as a function of impact parameter d_0 threshold are shown in Figure 7.7. Figure 7.7(a) is derived using the Monte Carlo samples of prompt muon and QCD multi-jet as pseudo-data, referred to as "full MC" in the figure. In 7.7(a), the pseudo-data approaches asymptotically to the QCD multi-jet sample with large d_0 of muon and they are mainly from the QCD events. The true background muon rate to be extracted from the pseudo-data is indicated by the blue square marker at $x = 0$ where all the tight and loose muons in the QCD multi-jet sample are taken into account. To extracted the true ϵ_{bg}, the background muon efficiency function $\epsilon_{\mathrm{bg}}(x)$ from the pseudo-data is parametrized by

$$f(x) = ae^{-bx^2} + cx + d \tag{7.14}$$

assuming that the contributions to $\epsilon_{\mathrm{bg}}(x)$ from prompt and non-prompt muons can be approximated by a Gaussian and a linear function respectively. The dashed curve on Figure 7.7(a) shows the parametrized efficiency function using a χ^2 fit. The background muon rate, ϵ_{bg}, is then derived by extrapolating the linear part of eq. (7.14) to $x = 0$ which is equivalent to the constant term of d in the equation. Figure 7.7(b) shows the background muon rate function $\epsilon_{\mathrm{bg}}(x)$ derived from the collision data and the result of the parametrization. The determined background muon efficiency, ϵ_{bg}, as function of muon η and jet multiplicity after applying the b-tagging is shown in Table 7.4.

| (a) MC samples | (b) Data |
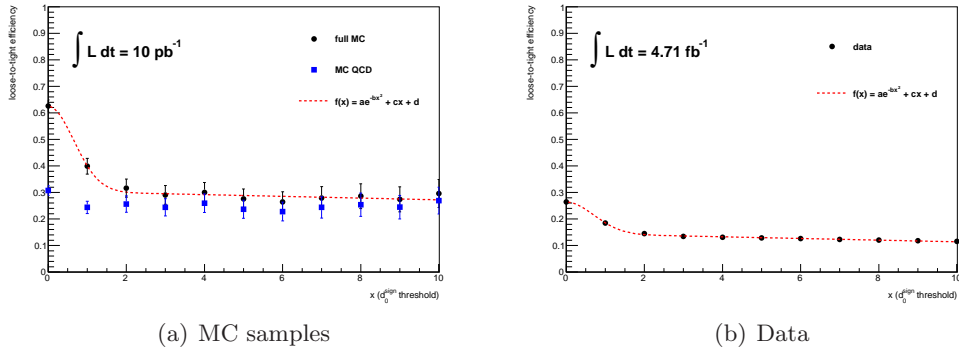
Figure 7.7: The background muon efficiencies, ϵ_{bg}, measured using (a) the Monte Carlo prompt muon samples and QCD multi-jet sample (full MC sample) and (b) the collision data based on impact parameter d_0 threshold.

7.3 Background from Z+jets, di-boson, single top and other decay of $t\bar{t}$

Background contaminations from other electroweak background processes, Z+jets, di-boson and single top production, are estimated by using Monte Carlo simulation samples described in Section 2.3. Their contaminations in the signal region are smaller than W+jets and QCD multi-jet

Table 7.4: The background muon efficiencies, ϵ_{bg}, according to muon η and jet multiplicity for after b-tagging. In this Table, "5-jets in." means for the event of 5-jets inclusive.

muon $|\eta|$	1-jet	2-jets	3-jets	4-jets	5-jets in.
0.0-0.5	0.129 ± 0.001	0.121 ± 0.002	0.114 ± 0.003	0.100 ± 0.007	0.130 ± 0.015
0.5-1.1	0.140 ± 0.001	0.130 ± 0.002	0.125 ± 0.003	0.120 ± 0.006	0.104 ± 0.013
1.1-1.4	0.166 ± 0.002	0.151 ± 0.003	0.155 ± 0.005	0.112 ± 0.010	0.128 ± 0.020
1.4-2.0	0.168 ± 0.001	0.157 ± 0.002	0.145 ± 0.004	0.145 ± 0.008	0.160 ± 0.019
2.0-2.5	0.189 ± 0.002	0.170 ± 0.004	0.168 ± 0.008	0.148 ± 0.016	0.143 ± 0.031
0.0-2.5	0.1508 ± 0.0004	0.141 ± 0.001	0.134 ± 0.002	0.123 ± 0.004	0.130 ± 0.015

backgrounds since these electroweak processes have two or more isolated lepton, small missing transverse energy and low jet multiplicities. After applying the event selection to the simulation samples, each kinematic distributions are normalized by using their production cross section, total number of events before the event selection and integrated luminosity of 4.7 fb^{-1}. The di-lepton channel of the $t\bar{t}$ production is considered as a background process to the signal process of $t\bar{t}$ lepton+jets channel in this analysis. Events that a W boson decays into τ lepton is also treated as background. Contamination of these background to the signal region are estimated by $t\bar{t}$ Monte Carlo sample and normalized after event selection. Only contribution of the $t\bar{t}$ di-lepton channel is subtracted from data when calculating the differential cross sections.

7.4 Combined Background Estimations in the Background Control Region

To check the background estimations, especially W+jets using the charge asymmetry method and QCD multi-jet background events using matrix method for electron+jets and muon+jets, W transverse mass m_{T} distributions of the control region which dominated W+jets and QCD multi-jet background events are shown in Figure 7.8. The events are after required to have exactly one lepton and one jet before applying missing transverse energy cut and b-tagging. The error of 50% and 20% are assigned as normalization uncertainty in QCD multi-jet background events for electron and muon channel respectively. Uncertainties of normalization for W+jets are shown in Table 7.1 and they are about 10% to 25% for each jet multiplicity. QCD multi-jet background events dominate in low m_{T} region of m_{T} and well separated to W+jets events of high m_{T} region. Estimations are in agreement with real data distribution within uncertainty. However, some overestimation of QCD multi-jet background events can be seen in electron channel around low m_{T} region and slightly underestimated W+jets events in both channel according to mean of DATA/MC ratio plots in Figure 7.8. To reduce the systematic uncertainties from normalization of QCD multi-jet background and W+jets events, tighter cuts are applied on missing transverse energy, W transverse mass, jet multiplicity and b-tagging as already described in Chapter 5. Distributions of basic kinematic in signal region are shown in the next Chapter 8.

(a) e+1jet

(b) μ+1jet
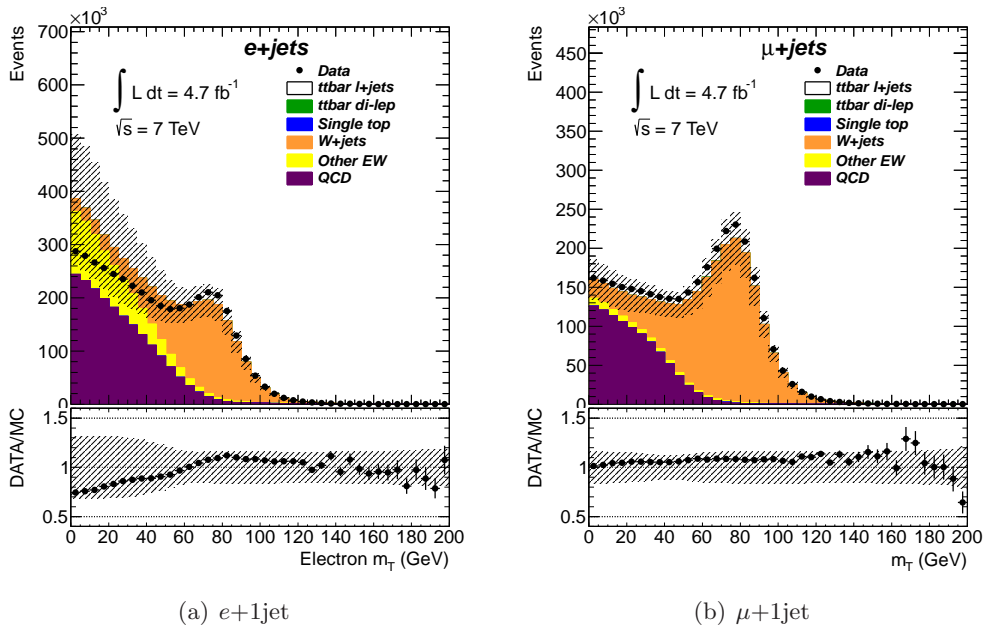
Figure 7.8: W transverse mass. electron+jets and muon+jets channel.

Chapter 8

Kinematic Distributions and Event Yields

8.1 Event Yields

The estimated number of events of signal and background processes and the observed number of events from real data are summarized in Table 8.1 after the event selection (Section 5.2) and likelihood cut (Section 6.4). The number of events of signal and background processes estimated by data driven method are denoted as "DD" and those estimated only by Monte Carlo simulation are denoted as "MC" in the Table. Only statistical uncertainties are shown in the Table. In the data set of 4.7 fb^{-1}, the total number of observed events are 15320 for e+jets channel and 17090 for μ+jets channel. The number of $t\bar{t}$ events evaluated by the Monte Carlo simulation for the standard model $t\bar{t}$ production with $\sigma_{t\bar{t}}^{\mathrm{SM}} = 166.8^{+16.5}_{-17.8}$ pb.

8.2 Kinematic Distributions

The distributions of basic kinematic variables in the signal region, where the jet multiplicity is at least four and the number of b-tagged jet is at least one, for electron and muon channels are shown here. The jet multiplicities are shown in Figure 8.1. The number of b-tagged jets, lepton transverse energy/momentum ($E_{\mathrm{T}}/p_{\mathrm{T}}$), lepton η, the transverse mass of W-boson (m_{T}), leading jet transverse energy (E_{T}) and missing transverse energy ($E_{\mathrm{T}}^{\mathrm{miss}}$) are shown in Figure 8.2 and 8.3 for e and μ+jets channel respectively. For these distributions the likelihood cut is not applied. The invariant mass and the rapidity of the $t\bar{t}$ system after reconstruction by kinematic fitting (Chapter 6) after the likelihood cut are shown in Figure 8.4. These reconstructed distributions are used for the calculation of differential cross sections. Details of measurement of differential cross sections using unfolding technique are described in Chapter 9. The details of the background estimation are describes at Chapter 7.

Table 8.1: Event yields of $t\bar{t}$ signal and background processes in the signal region compared to the observed events for lepton+jets channel after the event selection and likelihood cut.

Process	e+jets	μ+jets
$t\bar{t}$ (MC)	13796 ± 42	15210 ± 45
W+jets (DD)	1111 ± 28	1289 ± 30
QCD multi-jet (DD)	463 ± 23	223 ± 7
Single top (MC)	660 ± 8	731 ± 8
Z+jets (MC)	203 ± 8	124 ± 7
Di-boson (MC)	26 ± 1	26 ± 1
Total expected events (MC+DD)	16259 ± 3206	17603 ± 3088
Observed events (data)	15320	17090

(a) e+jets channel

(b) μ+jets channel
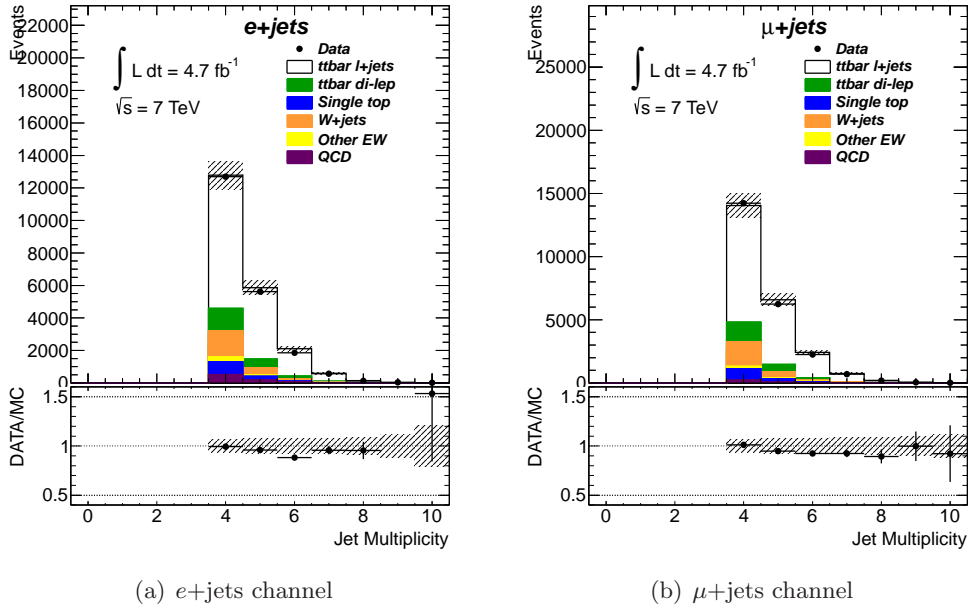
Figure 8.1: The number of selected jets for both electron channel 8.1(a), and muon channel 8.1(b) after the event selection.
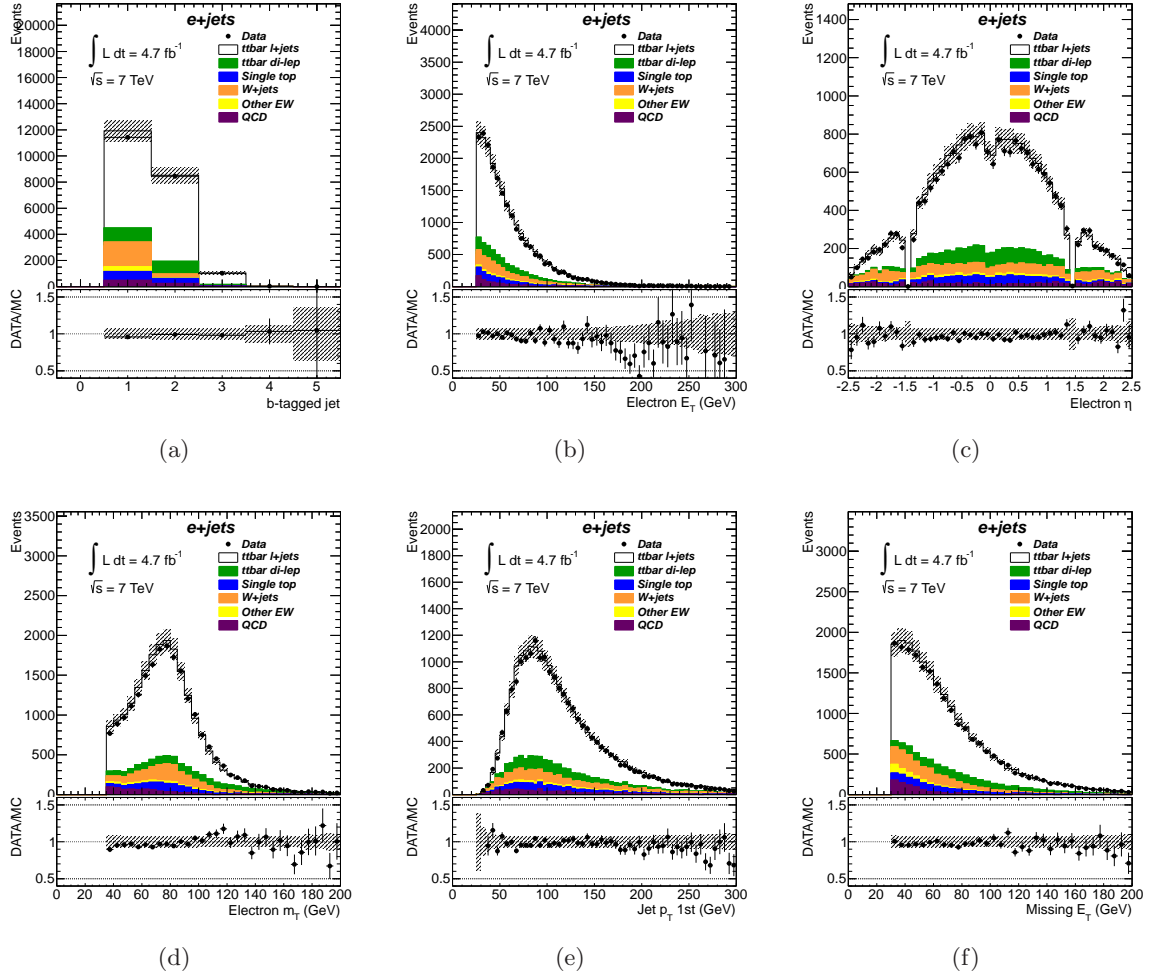
Figure 8.2: Basic kinematic distributions after applying the event selection for electron channel 4 jets inclusive sample, Figure 8.2(a) number of b-tagged jets, 8.2(b) electron transverse energy E_T, 8.2(c) electron eta η, 8.2(d) the W transverse mass of electron and missing transverse energy m_T, 8.2(e) first leading jet p_T and 8.2(f) missing transverse energy E_T^{miss}.

84
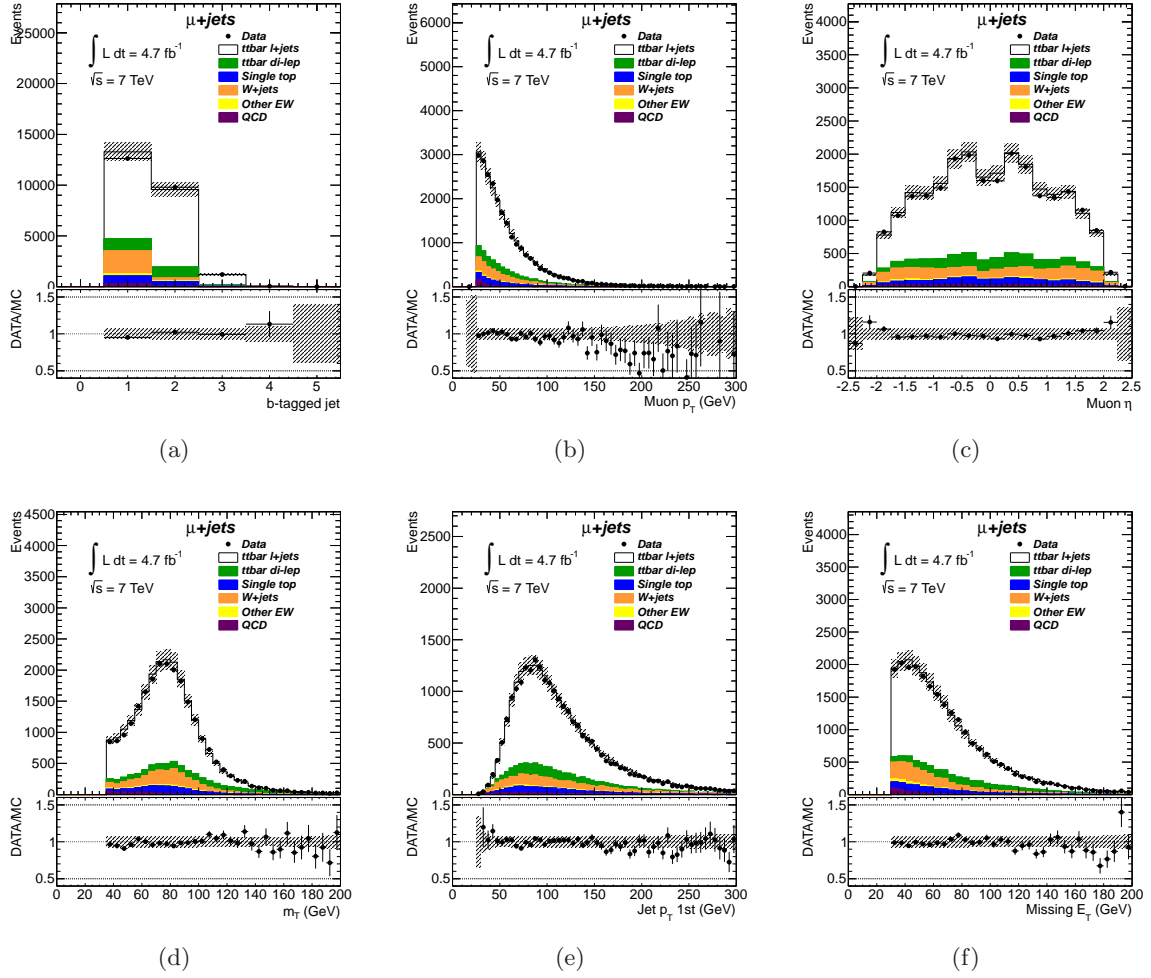
Figure 8.3: Basic kinematic distributions after applying the event selection for muon channel 4 jets inclusive sample. Figure 8.3(a) number of b-tagged jets, 8.3(b) muon transverse energy p_{T}, 8.3(c) muon η, 8.3(d) the W transverse mass of muon and missing transverse energy m_{T}, 8.3(e) first leading jet p_{T}, 8.3(f) missing transverse energy $E_{\mathrm{T}}^{\mathrm{miss}}$.
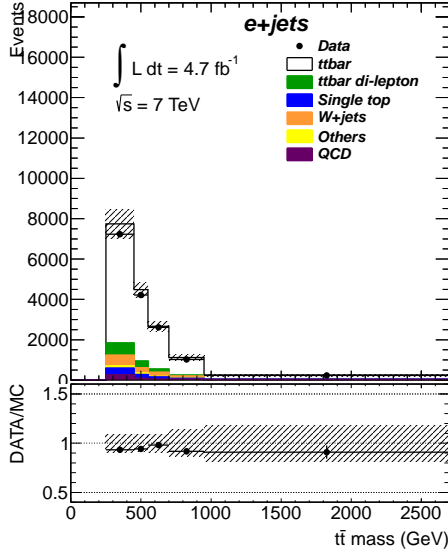
(a) $m_{t\bar{t}}$ e+jets channel
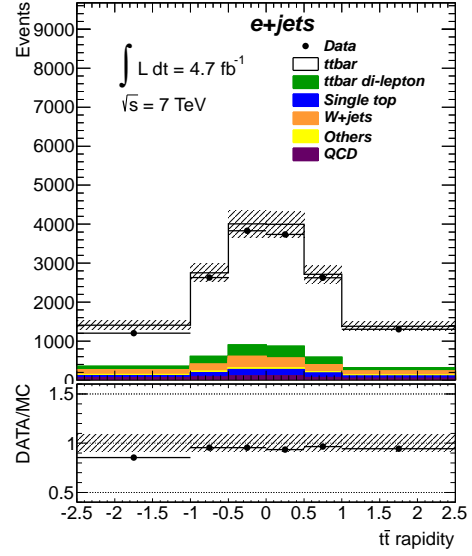
(b) $y_{t\bar{t}}$ e+jets channel
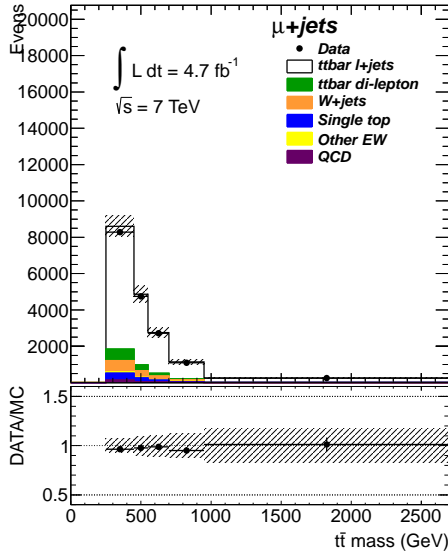
(c) $m_{t\bar{t}}$ μ+jets channel
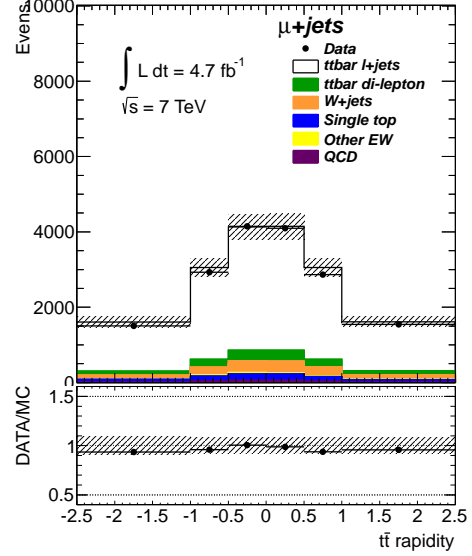
(d) $y_{t\bar{t}}$ μ+jets channel

Figure 8.4: The reconstructed $m_{t\bar{t}}$ and $y_{t\bar{t}}$ after the kinematic fitting and likelihood cut $\log L > -52$.

Chapter 9

Differential Cross Section and Unfolding

9.1 Differential Cross Section

The reconstructed distribution of $t\bar{t}$ system kinematics (N_i) after the event selections can be written in

$$N_i = \sum_j R_{ij} \sigma_j \mathcal{L} + B_i = \sum_j M_{ij} A_j \sigma_j \mathcal{L} + B_i \tag{9.1}$$

where:

- i means i th bin of reconstructed $t\bar{t}$ system kinematics

- j means j th bin of true $t\bar{t}$ system kinematics

- N_i is the observed number of events

- B_i is the estimated number of background events

- $\mathcal{L}$ is the integrated luminosity

- A_j is the efficiency (Figure 9.4)

- M_{ij} is the migration matrix (Figure 9.3)

The differential cross section σ_j is extracted by eq. (9.1)

$$\sigma_j = \frac{\sum_i (M^{-1})_{ji}(N_i - B_i)}{A_j \mathcal{L}} \tag{9.2}$$

and the efficiency A_j, which includes geometrical detector acceptance and $t\bar{t}$ lepton+jets event branch fraction $\mathrm{BR}(t\bar{t} \to \ell + \mathrm{jets}) = 0.438$ taken from the Particle Data Group [3], is extracted as below

$$A_j = \frac{N_j^{\text{after event selection}}}{N_j^{\text{before event selection}}} \mathrm{BR}(t\bar{t} \to \ell + \mathrm{jets}) \tag{9.3}$$

here N_j is the true distribution of $t\bar{t}$ system kinematics obtained from truth information of Monte Carlo simulation.

9.2 Binning

The binning of each variable is optimized using Monte Carlo simulation based on the resolution of the reconstructed distribution in fine bins of the corresponding truth variable. The RMS of difference between reconstructed and true $m_{t\bar{t}}$ (Figure 9.1) is defined as a resolution on each true $m_{t\bar{t}}$. The resolution curve was extracted and fitted with a 2nd-order polynomial show in Figure 9.2. Bin edges were extracted by finding the point where the resolution function evaluated at the midpoint of the bin is equal to the bin width, that is written in

$$m_{t\bar{t}}(n-1) + \frac{\text{SF} \cdot \text{RMS}(\text{m}_{t\bar{t}}(\text{n}))}{2} = m_{t\bar{t}}(n) \tag{9.4}$$

here

$$\text{RMS} = \alpha < m_{\text{true}} >^2 + \beta < m_{\text{true}} > + \gamma \tag{9.5}$$

and Scaling Factor (SF) determines the size of each bin, i.e. it takes fewer number of bins to give larger delta and vice versa. The effect of systematic uncertainties on this binning are also considered. The binning for rapidity of the $t\bar{t}$ system is also considered the same method. The final binning for $m_{t\bar{t}}$ is shown in Table 9.1.
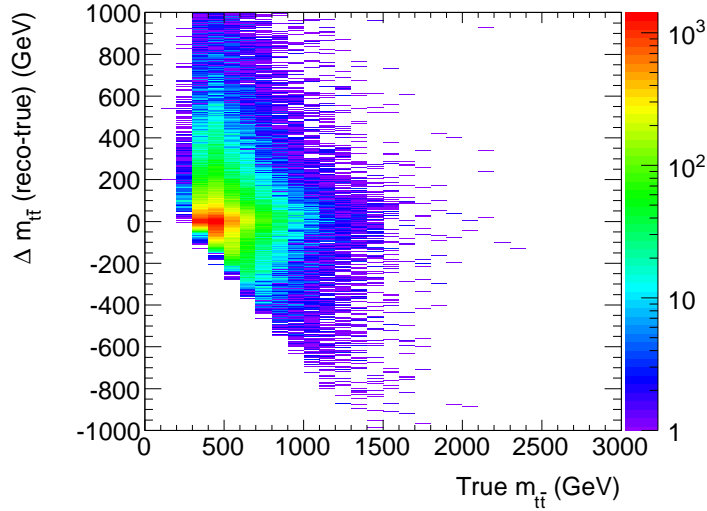
(a)

Figure 9.1: Resolution of $m_{t\bar{t}}$
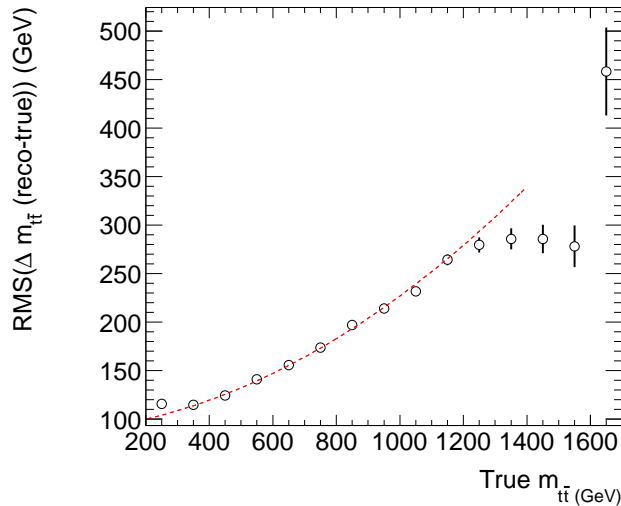
Figure 9.2: Resolution curve for $m_{t\bar{t}}$

9.3 Unfolding procedure

Due to limited detector resolutions and their imperfect acceptance, physical quantities are usually observed as smeared distributions. Their true distributions can be obtained by an "Unfolding Technique" that corrects for the detector effects and estimates the true distributions. To transform to true distribution, it applies response matrix (R_{ij}) to reconstructed distribution in unfolding. Then the response matrix is separated into migration matrix M_{ij} and efficiency A_j shown in eq. (9.1). They are derived from reconstructed and generated true information of Monte Carlo simulation. The migration matrix fold the true distribution into the measured distribution. Therefore by inverting this migration matrix, the measured distribution can be unfolded into the true distribution. To takes into account statistical fluctuation of observed data and relative sys-

Table 9.1: Bin widths for reconstructed $m_{t\bar{t}}$ and $y_{t\bar{t}}$ distributions.

	$m_{t\bar{t}}$ (GeV)	$y_{t\bar{t}}$
Bin1	250 - 450	-2.5 - -1.0
Bin2	450 - 550	-1.0 - -0.5
Bin3	550 - 700	-0.5 - 0
Bin4	700 - 950	0 - 0.5
Bin5	950 - 2700	0.5 - 1.0
Bin6	N/A	1.0 - 2.5

tematic shifts from several sources with pseudo experiment, eq. (9.2) is extended to following form

$$\sigma_j(d_k) = \frac{\sum_i (M^{-1})_{ji}(d_k)[Po(N_i) - B_i(d_k)]}{A_j(d_k)\mathcal{L}(d_k)} \tag{9.6}$$

where $Po()$ is the Poisson smearing and d_k are systematic sources which are normalized to one sigma variation of Gaussian distribution. A cross section is calculated for a given variable ($m_{t\bar{t}}$ and $y_{t\bar{t}}$) from each pseudo-experiment. The median of the results from pseudo-experiment and their 68% interval provide mean of cross section and its uncertainty.

9.4 Unfolding Technique

Several methods have been developed in order to unfold detector effects in data. We consider the following two approaches:

- simple matrix inversion, and

- Singular Value Decomposition (SVD) approach.

9.4.1 Simple Matrix Inversion

Unfolding can be described as a matrix inversion. Assuming a variable of interest can be simulated with the detector response, we can have a true parton level and measured distribution which are defined as v_{true} and v_{meas}. Thus this gives a unique and well defined transformation between the true and measured distribution which is written as

$$\mathcal{M}v_{\mathrm{true}} = v_{\mathrm{meas}} \tag{9.7}$$

where $\mathcal{M}$ is referred to as the migration matrix and fold the true distribution into the measured one. Therefore calculating the inverted matrix, the measured data is unfolded into the true distribution.

9.4.2 Singular Value Decomposition

Although the unfolding method by the matrix inversion is very simple, it is affected by low statistics of data and simulation and also by large systematic uncertainties, and the unfolded result become sometimes unstable. In order to avoid these instabilities we used another way of unfolding based on the Singular Value Decomposition (SVD) [49] of the response matrix. A singular value decomposition of $m \times n$ matrix $\mathcal{M}$ is its factorization of the form

$$\mathcal{M} = USV^T \tag{9.8}$$

where U is an $m \times n$ orthogonal matrix, V is an $n \times n$ orthogonal matrix, S is an $m \times n$ diagonal matrix with non-negative diagonal elements:

$$UU^T = U^TU = I, VV^T = V^TV = I \tag{9.9}$$
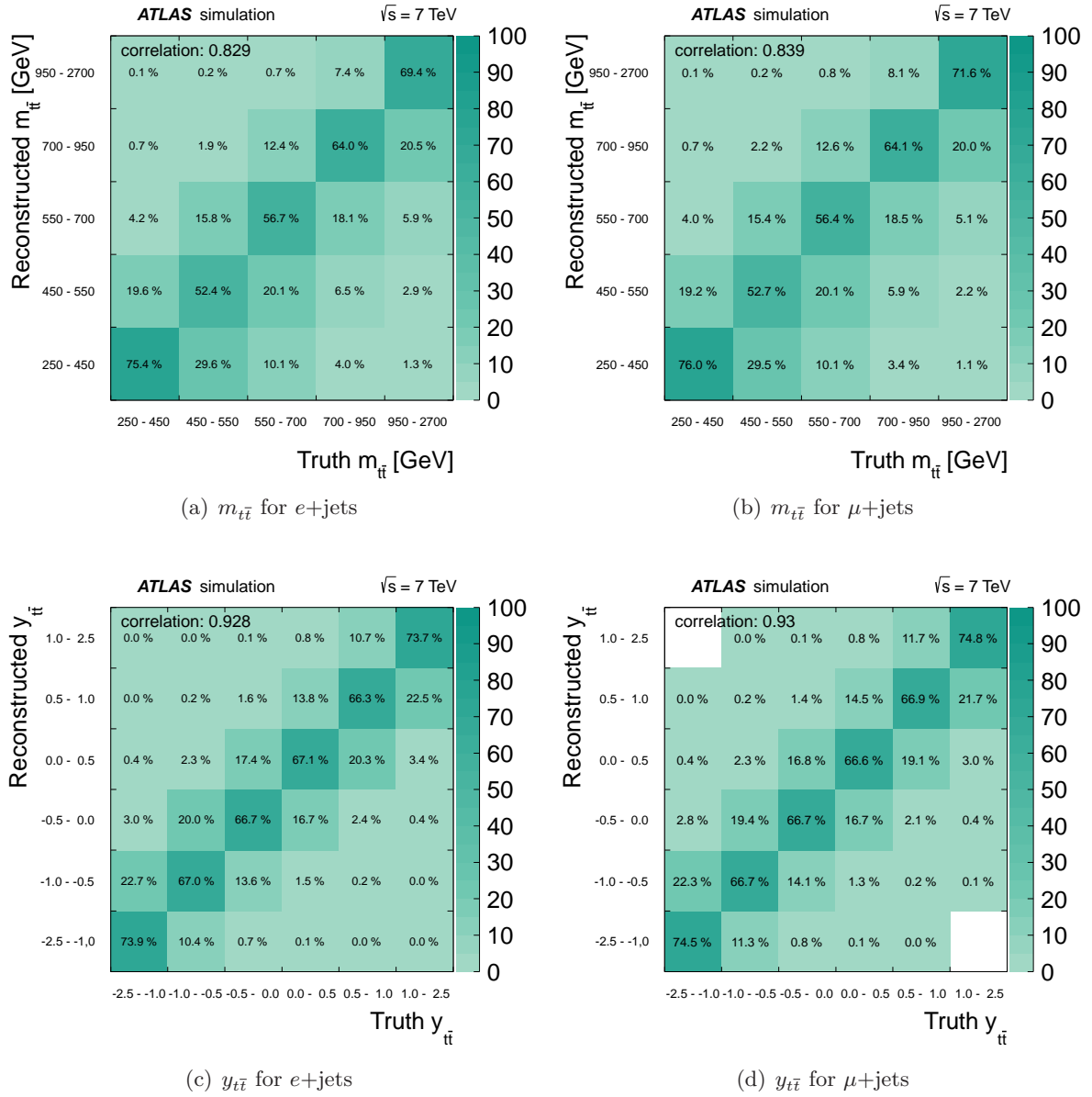
Figure 9.3: Migration Matrices for $m_{t\bar{t}}$ and $y_{t\bar{t}}$.

(a) e+jets

(b) μ+jets
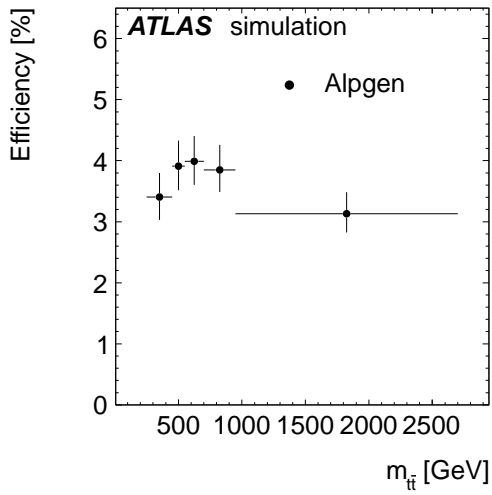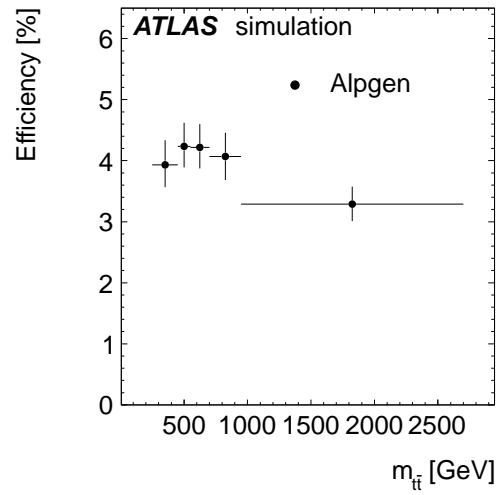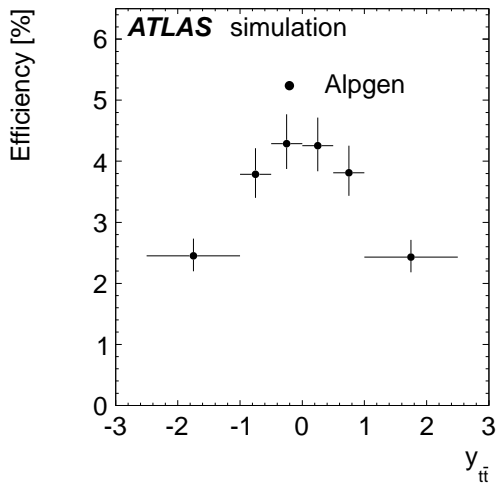
(c) e+jets
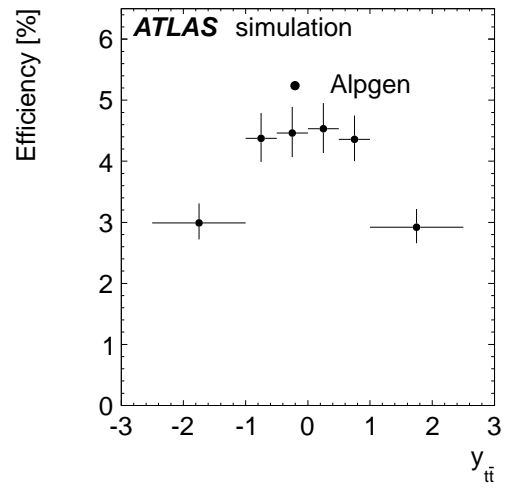
(d) μ+jets

Figure 9.4: Efficiencies for $m_{t\bar{t}}$ and $y_{t\bar{t}}$.

$$S_{ij} = 0 \text{ for } S_{ii} \equiv s_i \geq 0 \qquad (9.10)$$

The quantities s_i are called singular values of the matrix $\mathcal{M}$. The inverted migration matrix is written as

$$\mathcal{M}^{-1} = V S^{-1} U^T \qquad (9.11)$$

By factorizing the response matrix with SVD, the instabilities can be localized and the following regularization and rotation make the unfolding smooth.

9.5 Self Consistency Test

In order to test the validity of the unfolding techniques the self consistency test is performed by comparing unfolded cross sections with true values using simulated $t\bar{t}$ signal samples by ALPGEN. Obtained unfolded cross sections by the SVD approach for e+jet and μ+jet decay channels and the true cross section for the MC sample are compared in Tables 9.2 and 9.3. They are also shown in plots of Figure 9.5. As shown in these tables and plots the SVD unfolding reproduces the generated cross sections very precisely. The same conclusion is obtained for the matrix inversion unfolding, too.

Table 9.2: Obtained cross sections of $m_{t\bar{t}}$ from the simulated signal sample with the SVD unfolding approach for e+jets and μ+jets channels and generated true cross sections.

$m_{t\bar{t}}$ [GeV]	$d\sigma/dm_{t\bar{t}}$[fb/ GeV]		
	e+jets	μ+jets	Truth
250 - 450	432.8 ± 7.1	433.2 ± 6.6	432.9 ± 0.1
450 - 550	443.5 ± 7.1	443.5 ± 6.8	443.4 ± 0.1
550 - 700	162.2 ± 3.7	162.0 ± 3.5	162.3 ± 0.1
700 - 950	37.5 ± 1.3	37.5 ± 1.3	37.47 ± 0.02
950 - 2700	1.26 ± 0.07	1.26 ± 0.07	1.259 ± 0.001

9.6 Combination of Analysis Channels

The unfolded cross sections from the two analysis channels, e+jets and μ+jets, are combined using a weighted mean which includes the full covariance matrix between the two channels. Since the covariance matrix is used in the weighting, the estimate is a best linear unbiased estimator (BLUE) of the cross-section. The covariance matrix is estimated from simulated events using the same pseudo experiment setup described in Section 9.3.
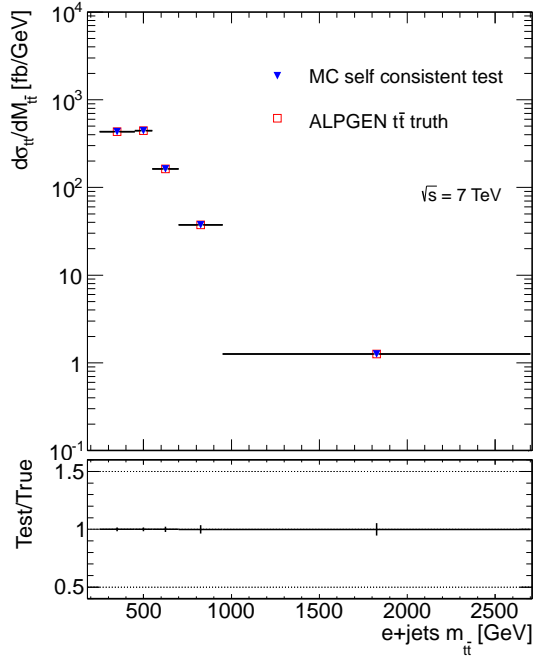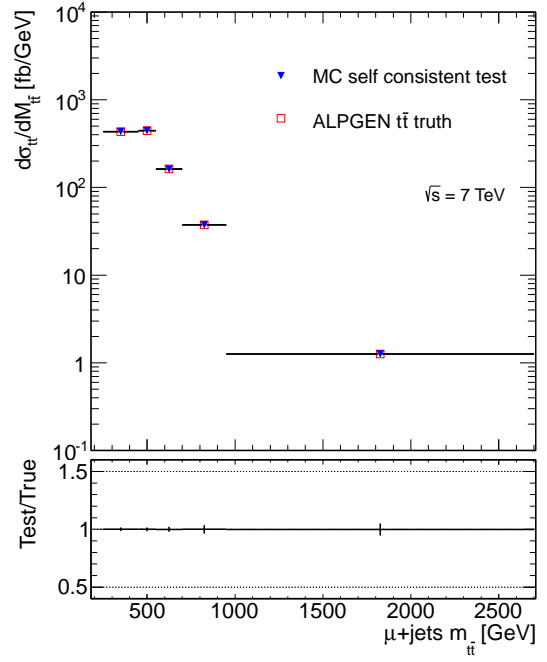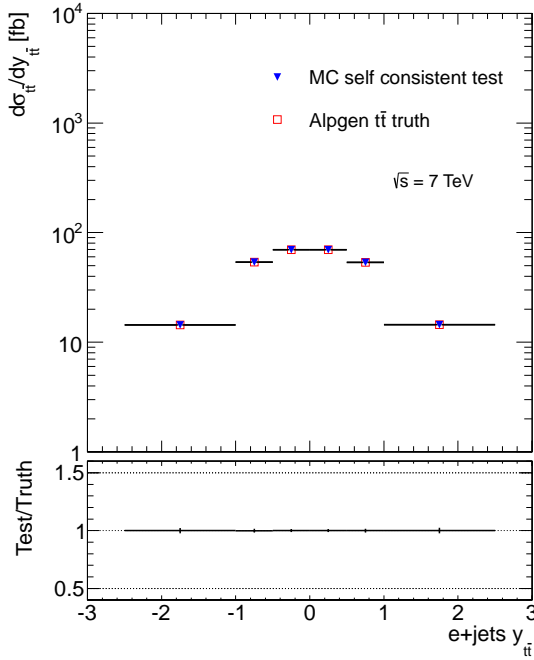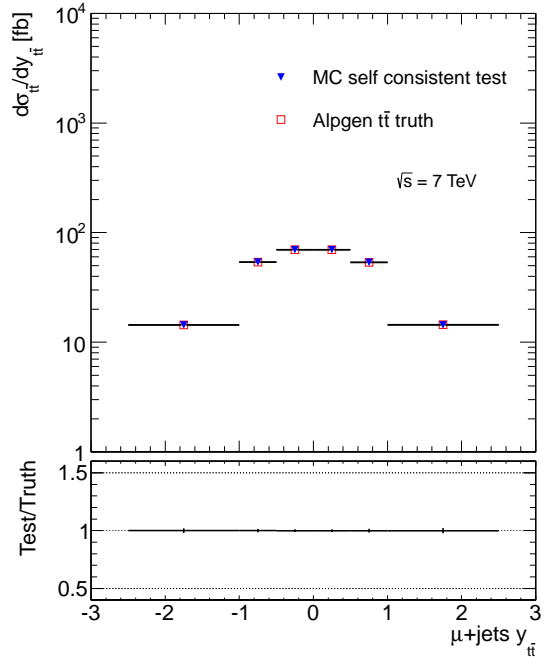
Figure 9.5: Self consistency test of SVD for $m_{t\bar{t}}$ and $y_{t\bar{t}}$.

94

Table 9.3: Obtained cross sections of $y_{t\bar{t}}$ from the simulated signal sample with the SVD unfolding approach for e+jets and μ+jets channels and generated true cross sections.

$y_{t\bar{t}}$	$d\sigma/dy_{t\bar{t}}$ [fb]		
	e+jets	μ+jets	Truth
-2.5 - -1.0	14.4 ± 0.5	14.4 ± 0.4	14.40 ± 0.004
-1.0 - -0.5	53.8 ± 1.0	53.8 ± 0.9	53.80 ± 0.018
-0.5 - 0.0	69.9 ± 1.2	69.9 ± 1.2	69.91 ± 0.020
0.0 - 0.5	69.9 ± 1.2	69.9 ± 1.2	69.91 ± 0.020
0.5 - 1.0	53.6 ± 1.1	53.5 ± 1.1	53.59 ± 0.018
1.0 - 2.5	14.4 ± 0.5	14.4 ± 0.4	14.43 ± 0.004

Chapter 10

Systematic Uncertainties

10.1 Estimation of Systematic Uncertainty

In this chapter systematic effects on the measured cross sections from various modeling aspects are described. The analysis procedure is repeated with the displaced parameters of each source of systematic effect in order to obtain distorted distributions of the variable of interest ($m_{t\bar{t}}$ and $y_{t\bar{t}}$). The obtained distributions are considered as the displacements of measured cross section from the nominal measured value in each bin of $m_{t\bar{t}}$ and $y_{t\bar{t}}$ corresponding to the upward and downward shift of parameters of each systematic effect. If the source of the systematic effects has no nominal distribution as in the case of evaluating the effect by comparing two non-nominal models, the systematic effect is considered to have the same size in both the upward and the downward direction of the measured cross sections in each bin. The nominal distribution and the distorted distributions are handled as the inputs to the pseudo-experiment (see Section 9.3 for details) that performs unfolding and efficiency correction, and enables combination of the e+jets and μ+jets channels.

   In the following sections the procedures to evaluate displaced distributions of the cross sections are described for each source of systematic effects. Obtained systematic effects on the measured cross sections are summarized in Tables of Chapter 11

10.2 Signal and Background Modeling

10.2.1 Signal Modeling

Systematic shifts are evaluated by comparing between simulated $t\bar{t}$ signal samples: the default sample generated by ALPGEN interfaced to HEWIG and the samples by POWHEG interfaced to HERWIG.

10.2.2 Parton Shower Modeling

Effect of parton shower modeling is evaluated by comparing two samples of POWHEG interfaced to HERWIG and PYTHIA.

10.2.3 Initial and Final State Radiation

Effect of initial and final state radiations are evaluated by using AcerMC [25] sample interfaced to PYTHIA. The amount of initial and final state radiation is modified by changing parameters of PYTHIA [26], such as the Λ_{QCD} scale, so that the variations of parameters result in increase or decrease initial or final state radiation.

10.2.4 QCD Multi-jet

QCD multi-jet background is estimated by the data driven method of matrix method as described in Section 7.2. The normalization uncertainty of 50% for electron channel and 20% for muon channel in the event yields is assigned. Shape systematic uncertainties are considered as follows: the difference of real efficiency ϵ_{real} or fake rate ϵ_{fake} between matrix method A and B, $\epsilon^{\mathrm{A}} - \epsilon^{\mathrm{B}}$, are assigned for muon channel. Up and down shift of 1σ are provided for the real efficiency ϵ_{real} and fake rate ϵ_{fake} for electron channel. This shifts are added to mean value of ϵ_{real} and ϵ_{real} in quadrature.

10.2.5 W+jets Process

The normalization of W+jets processes is estimated by the real data and Monte Carlo simulation as described in Section 7.1 and their uncertainty is considered.

10.2.6 Single top and Di-boson Production Cross Sections

The normalization of single top processes takes into account the theory uncertainty of approximate NNLO cross section for each channel (t-, s-channel and Wt [52]). 5% for the normalization uncertainty of di-boson processes is considered.

10.3 Detector Modeling

10.3.1 Lepton Trigger, Reconstruction and Identification Efficiency

The mis-modeling of lepton trigger, reconstruction and identification efficiencies in Monte Carlo simulation is corrected by scale factors derived by measurements of the efficiency in data as described in Section 4.2,4.3,5.1.1 and 5.1.2. Events of $Z \to \mu\mu$, $Z \to ee$ and $W \to e\nu$ production and decay processes are used to obtain each scale factor depending on the transverse momentum and pseudo rapidity of lepton. To derive the distorted distribution, the uncertainties in these scale factors are considered.

10.3.2 Lepton Momentum/Energy Scale and Resolution

The differences of lepton momentum/energy scale and resolution between Monte Carlo simulation and data are corrected by the factors which evaluated by $Z \to \ell\ell$ events to compare to the distributions as described in Section 4.2.3 and 4.3.3. The uncertainties of these correction factors are taken into account in the event selection when the distorted distributions are derived.

10.3.3 Jet Energy Scale

The jet energy scale correction is obtained from a combination of *in-situ* technique of Z+jet and γ+jet, the corresponding uncertainty is determined. The uncertainties from the low-p_{T} jets derived from Z+jet, γ+jet and di-jet p_{T} balance are propagated to high p_{T} jets for calibration of jet energy in the TeV regime. The combined jet energy scale uncertainty as function of jet p_{T} is shown in Figure 10.1(a) and 10.1(b) (denoted as Baseline *in situ* JES). Additional uncertainty on the jet energy scale of b-jets is derived based on Monte Carlo sample and shown in Figure 10.1(c).

Uncertainty contributions due to the quark/gluon composition and response (caused by different calorimeter response depending on the jet flavor) of $t\bar{t}$ lepton+jets event and the effect of nearby jets are also considered. They are especially important for multi-jet environment of top production and its background processes. The estimated uncertainties are shown in Figure 10.1(a) and 10.1(b) (denoted as Flav. composition, Flav. response and Close-by jet).

The pileup effect correction is derived from Monte Carlo simulation and applied to reconstructed jet. The correction to the jet energy is estimated by studying dependence of the difference between the reconstructed jet p_{T} and the truth jet p_{T} on the number of reconstructed primary vertices. The fractional jet energy scale uncertainty due to pileup effect is also shown in 10.1(a) and 10.1(b).

10.3.4 Jet Energy Resolution

The energy resolution of jets is measured in di-jet events and agrees with predictions from Monte Carlo simulations within 10%. The jet transverse momentum in the Monte Carlo samples are smeared according to its kinematics (jet p_{T} and η) within the uncertainty of the jet transverse momentum resolution so that they are derived the varied distribution. The difference between nominal and obtained varied distribution is symmetrized and is applied as systematic uncertainty in the unfolding.

10.3.5 Jet Reconstruction Efficiency

The jet reconstruction efficiency is estimated by use of minimum bias and QCD di-jet events. The observed difference between data and Monte Carlo is applied to Monte Carlo by discarding a fraction of jets randomly within the inefficiency range. The difference between nominal and obtained varied distribution is symmetrized and is applied as systematic uncertainty in the unfolding.

10.3.6 Missing Transverse Energy

The uncertainties from the momentum or energy scale and resolutions of leptons and jets are propagated to the calculation of the missing transverse energy. Additional uncertainties are added as contributions of calorimeter cells not associated to any jets and soft jets ($7\,\mathrm{GeV} < p_{\mathrm{T}} < 20\,\mathrm{GeV}$).

(a) $|\eta_{\mathrm{jet}}| = 0.5$ for $t\bar{t}$ lepton+jets

(b) $|\eta_{\mathrm{jet}}| = 2.0$ for $t\bar{t}$ lepton+jets

(c) $|\eta_{b-\mathrm{jet}}| < 2.5$ for b-jet
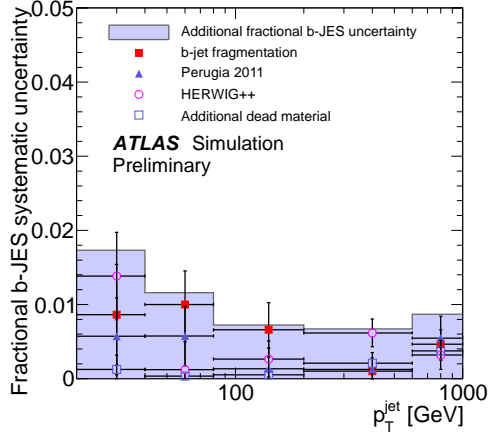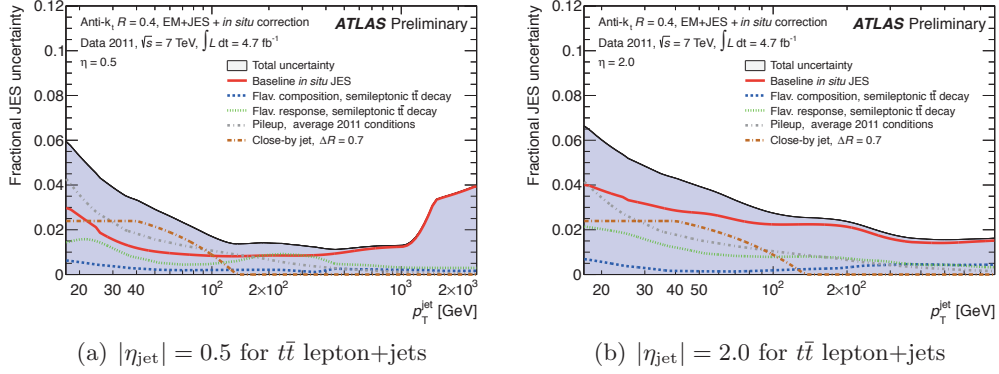
Figure 10.1: Fractional jet energy scale uncertainty as a function of jet p_{T} [36, 53]. The uncertainty shown in Figure 10.1(a) and 10.1(b) applies to $t\bar{t}$ lepton+jets channel to take into account the quark/gluon composition and response. The $|\eta|$ region of jets are $|\eta| = 0.5$ and $|\eta| = 2.0$ respectively. The fractional uncertainty on the jet energy scale of b-jets ($|\eta| < 2.5$) is shown in Figure10.1(c).

10.3.7 b-tagging Efficiency

The b-tagging efficiencies and its scale factor are evaluated by QCD multi-jet event based study of $p_\mathrm{T}^\mathrm{rel}$ and *System 8*, and $t\bar{t}$ event based study of The kinematic selection method in di-lepton channel and the kinematic fit method in lepton+jets channel as described in Section 4.6.4. The c-jet mistag rate is measured based on D^* mesons and the b- and c-jet scale factors are uncorrelated. The scale factors of b-, c- and light jets are varied independently within their uncertainties.

10.3.8 Luminosity

Luminosity is varied within its uncertainty on the measured value from Van der Meer scans (about 1.8%) [54].

Chapter 11

Results and Discussion

11.1 Results

The results of the measurement of the top quark pair production differential cross section as a function of the mass and the rapidity of the $t\bar{t}$ system are presented in this section. The efficiency and migration matrix which are derived from the ALPGEN $t\bar{t}$ sample are used for the unfolding and differential cross section calculation shown in Figures 9.4 and 9.3. Results obtained by two unfolding methods, the matrix inversion and the SVD approach, are presented respectively. To avoid overall normalization uncertainties of the results the final unfolded differential cross sections are divided by the total production cross section and presented as relative differential cross sections. The total production cross section is also measured with the collision data by simple cut and count method as shown in eq. (9.6). The results of the total production cross section is 160 ± 18 pb. Both statistical and systematic uncertainties are included. Predicted standard model $t\bar{t}$ production cross section is 167^{+17}_{-18} pb for top quark mass of 172.5 GeV. This cross section has been calculated at approximate NNLO in QCD with Hathor 1.2 [55] using MSTW2008 PDF [56]. The measured total cross sections are consistent with standard model prediction within error. The final unfolded relative differential cross sections for $m_{t\bar{t}}$ and $y_{t\bar{t}}$ are presented in Tables 11.1 and 12.2 and are plotted in Figures 11.1 and 11.2. All systematic uncertainties are shown in Tables 11.3, 11.4, 11.5 and 11.6. All results presented in this section are obtained by combining e+jets and μ+jets analysis channels and are denoted as ℓ+jets in the tables. The results which are extracted from MC@NLO's efficiencies and migration matrices also presented in Appendix A.

11.2 Discussion

The obtained differential cross sections shown in Tables 11.1 and 11.2 with different unfolding methods are consistent each other within total errors. The measured differential cross sections as a function of $m_{t\bar{t}}$ and $y_{t\bar{t}}$ are consistent with the theoretical predictions based on the standard model. From Tables 11.3, 11.4, 11.5 and 11.6 we find that dominant systematic uncertainties come from the jet energy scale and b-tagging efficiency scale factor. Parton shower modeling and initial and final state radiation modeling (ISR/FSR) also affect on the $m_{t\bar{t}}$ distribution. From the
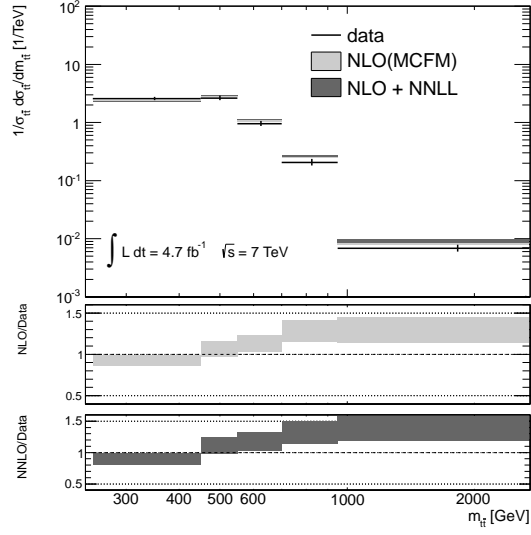
(a) SVD
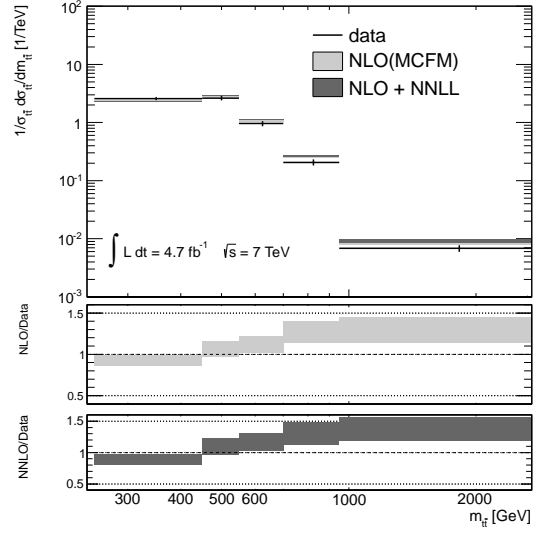
(b) Matrix Inversion

Figure 11.1: Unfolded differential cross section as a function of $m_{t\bar{t}}$ compared to MCFM NLO and Approximate NNLO theoretical predictions.
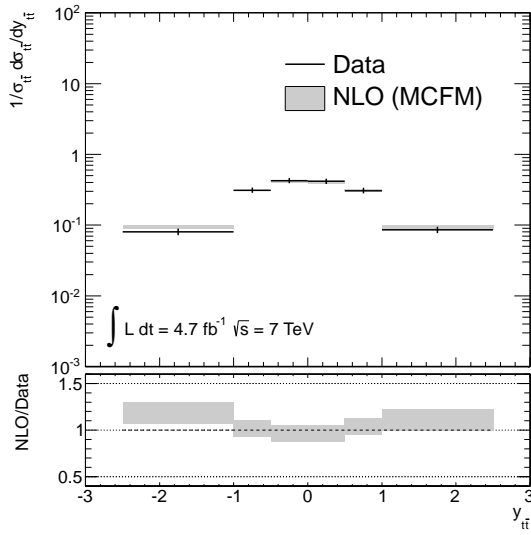
(a) SVD
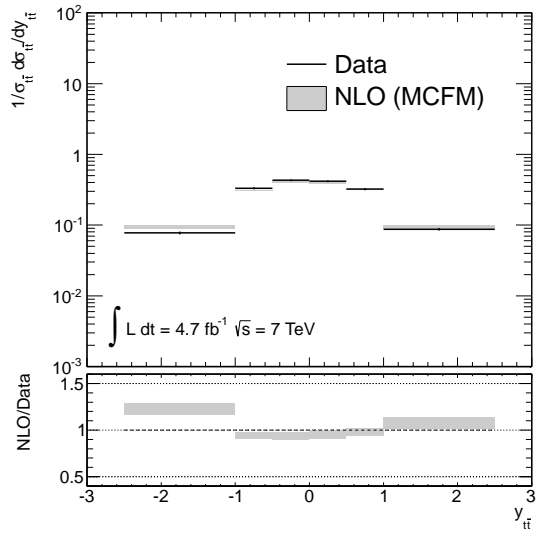
(b) Matrix Inversion

Figure 11.2: Unfolded differential cross section as a function of $y_{t\bar{t}}$ compared to MCFM NLO and Approximate NNLO theoretical predictions.

Table 11.1: Obtained relative differential cross sections for $m_{t\bar{t}}$ used SVD and Matrix Inversion unfolding technique and theoretical predictions at NLO and approximate NNLO assuming the standard model.

$m_{t\bar{t}}$ (GeV)	$1/\sigma_{t\bar{t}} \, d\sigma_{t\bar{t}}/dm_{t\bar{t}}$ (1/TeV)			
	SVD	Matrix Inversion	NLO	approx.NNLO
250 - 450	2.6 +0.2 / -0.1	2.6 ±0.2	2.39 ± 0.04	2.29 ± 0.03
450 - 550	2.6 +0.3 / -0.2	2.6 ±0.2	2.80 ± 0.02	2.91 ± 0.02
550 - 700	1.0 ±0.1	1.0 ±0.1	1.07 ± 0.02	1.12 ± 0.02
700 - 950	0.21 +0.03 / -0.02	0.21 +0.03 / -0.02	0.26 ± 0.01	0.279 ± 0.007
950 - 2700	0.007 ±0.001	0.007 ±0.001	0.0096 ± 0.0009	0.0093 ± 0.0005

measurement we find that the statistical accuracy at high $m_{t\bar{t}}$ regions is not so good. Hence the sensitivity to new physics at the high $m_{t\bar{t}}$ regions is not so high with current statistical significance and also with current systematic errors.

For the future measurement of differential cross section several improvements of the analysis are necessary. For example they are:

- reduction of systematic uncertainties for further precision measurement especially on high mass region of $m_{t\bar{t}} > 950$ GeV,

- development of alternative background estimation for wide area of $m_{t\bar{t}}$ from a few hundred GeV to a few TeV, and

- data driven estimation of W+jets for both normalization and shape due to less statistical of Monte Carlo simulation sample and difficulty of precise modeling of multi jet production associated to W boson.

Table 11.2: Obtained relative differential cross sections for $y_{t\bar{t}}$ used SVD and matrix inversion unfolding technique and theoretical prediction at NLO assuming the standard model.

$y_{t\bar{t}}$	$1/\sigma_{t\bar{t}} \ d\sigma_{t\bar{t}}/dy_{t\bar{t}}$		
	SVD	Matrix Inversion	NLO
-2.5 - -1.0	0.080 +0.009 / -0.008	0.078 +0.003 / -0.004	0.095 ± 0.005
-1.0 - -0.5	0.31 +0.03 / -0.03	0.33 ±0.01	0.313 ± 0.004
-0.5 - 0.0	0.42 +0.04 / -0.03	0.43 ±0.01	0.40 ± 0.01
0.0 - 0.5	0.42 +0.04 / -0.03	0.42 ±0.01	0.40 ± 0.01
0.5 - 1.0	0.31 +0.03 / -0.03	0.32 ±0.01	0.32 ± 0.04
1.0 - 2.5	0.086 +0.009 / -0.008	0.087 ±0.004	0.095 ± 0.005

Table 11.3: Uncertainties for relative differential cross section for $m_{t\bar{t}}$ combined result. SVD unfolding technique is used.

$1/\sigma\mathrm{d}\sigma/\mathrm{d}m_{t\bar{t}}$	ℓ+jets				
Uncertainty (%)	250-450	450-550	550-700	700-950	950-2700
Total[%]	6.7 / -6.5	9.9 / -9.7	10.4 / -9.0	11.5 / -10.6	12.9 / -12.0
Stat. only[%]	3.3 / -3.2	1.4 / -1.4	2.3 / -2.5	3.0 / -2.8	4.0 / -4.1
Syst. only[%]	5.9 / -5.7	9.8 / -9.6	10.2 / -8.6	11.1 / -10.2	12.3 / -11.3
Luminosity[%]	1.0 / -1.3	0.3 / -0.5	0.8 / -0.6	0.8 / -0.8	0.8 / -0.3
JetEnergyScale[%]	3.4 / -3.6	8.9 / -7.2	5.0 / -4.5	5.8 / -5.1	6.4 / -5.5
JetEnergyResolustion[%]	1.8 / -1.9	0.7 / -0.6	1.2 / -0.3	0.7 / -1.0	0.9 / -1.5
JetRecoEfficiency[%]	1.2 / -0.7	0.6 / -0.2	0.8 / -1.0	0.7 / -0.1	1.6 / -0.5
CellOut+SoftJet[%]	1.9 / -1.2	0.5 / -0.4	0.8 / -0.7	0.5 / -0.9	1.2 / -0.5
Pileup[%]	1.0 / -1.5	0.5 / -0.5	1.1 / -1.0	0.6 / -1.3	0.7 / -1.0
b-tag b-jet[%]	3.4 / -3.3	4.7 / -4.2	6.1 / -5.1	7.3 / -5.5	7.6 / -5.5
b-tag c-jet[%]	1.3 / -0.5	0.5 / -0.2	1.0 / -0.8	0.8 / -0.7	0.6 / -1.2
b-tag light jet[%]	0.8 / -1.5	0.1 / -0.6	0.3 / -0.8	0.3 / -0.7	0.5 / -1.5
JVF SF[%]	1.8 / -2.3	1.4 / -1.2	1.8 / -0.8	1.5 / -1.7	2.1 / -1.4
ElectronEnergyScale[%]	1.4 / -1.5	0.5 / -0.5	0.5 / -0.7	0.9 / -0.7	1.1 / -1.2
ElectronEnegyResolution[%]	1.2 / -1.0	0.2 / -0.3	0.7 / -0.8	0.9 / -0.9	1.0 / -1.0
MuonMomentumScale[%]	1.6 / -1.3	0.4 / -0.3	1.0 / -0.4	0.8 / -1.0	0.6 / -0.1
MuIDMomentumSmear[%]	0.9 / -1.1	0.5 / -0.4	0.9 / -0.8	0.9 / -0.4	1.0 / -0.8
MuMSMomentumSmear[%]	0.3 / -1.2	0.4 / -0.1	0.7 / -0.7	1.0 / -1.1	0.5 / -0.5
LeptonSF Trigger[%]	2.2 / -2.4	0.8 / -0.8	1.1 / -0.7	1.1 / -0.5	1.1 / -1.7
LeptonSF Reco[%]	1.1 / -1.1	0.3 / -0.2	1.0 / -0.3	0.2 / -0.4	0.9 / -0.3
LeptonSF ID[%]	1.4 / -1.4	1.4 / -1.4	2.3 / -2.2	1.6 / -1.8	0.9 / -1.9
W+jets Normalization[%]	0.2 / -1.2	0.6 / -0.1	0.8 / -0.6	0.7 / -1.0	0.5 / -1.1
QCD Normalization[%]	1.3 / -0.8	0.6 / -0.4	1.6 / -0.5	1.4 / -2.5	2.3 / -3.2
QCD real eff.[%]	0.4 / -1.8	0.6 / -0.5	0.9 / -1.0	1.0 / -1.0	0.2 / -1.0
QCD fake eff.[%]	0.8 / -1.5	0.6 / -0.3	1.1 / -0.5	0.8 / -1.9	1.2 / -2.5
QCD shpae[%]	1.4 / -1.4	0.4 / -0.3	0.8 / -0.8	0.4 / -1.0	1.4 / -0.5
Singletop, di-boson cross section[%]	0.8 / -1.6	0.5 / -0.6	0.8 / -0.8	1.1 / -1.2	0.6 / -0.9
Parton shower Model[%]	2.6 / -2.3	1.2 / -1.3	3.5 / -4.2	4.6 / -6.1	5.5 / -7.1
ISR/FSR[%]	2.0 / -1.0	3.1 / -3.1	4.6 / -3.9	4.8 / -4.2	3.9 / -3.3
MC stat.[%]	0.8 / -1.2	0.7 / -0.3	1.3 / -0.5	0.4 / -1.5	1.6 / -1.8

Table 11.4: Uncertainties for relative differential cross section for $m_{t\bar{t}}$ combined result. matrix inversion unfading technique is used.

$1/\sigma \mathrm{d}\sigma/\mathrm{d}m_{t\bar{t}}$	ℓ+jets				
Uncertainty (%)	250-450	450-550	550-700	700-950	950-2700
Total	6.4 / -6.0	9.2 / -8.6	9.6 / -9.6	12.1 / -10.8	12.4 / -12.0
Stat. only	3.4 / -3.4	1.4 / -1.5	2.5 / -2.5	3.1 / -3.0	4.1 / -4.0
Syst. only	5.4 / -4.9	9.1 / -8.5	9.2 / -9.2	11.7 / -10.4	11.7 / -11.3
Luminosity	0.7 / -0.6	0.6 / -0.5	1.0 / -0.2	0.5 / -1.1	0.6 / -1.4
JetEnergyScale	2.1 / -2.4	7.4 / -6.3	4.6 / -3.7	4.4 / -4.6	6.0 / -6.6
JetEnergyResolustion	0.8 / -1.5	0.8 / -0.5	0.2 / -0.6	0.5 / -1.1	0.5 / -0.5
JetRecoEfficiency	0.9 / -0.5	0.0 / -0.1	0.3 / -1.0	1.1 / -0.3	0.4 / -1.1
CellOut+SoftJet	0.4 / -1.0	0.4 / -0.4	0.5 / -1.1	0.8 / -0.7	1.1 / -1.0
Pileup	0.8 / -1.1	0.4 / -0.1	0.1 / -0.5	0.6 / -0.2	1.4 / -0.4
b-tag b-jet	3.6 / -2.7	4.9 / -4.3	6.2 / -5.0	7.9 / -6.3	7.1 / -5.1
b-tag c-jet	0.6 / -1.0	0.5 / -0.4	0.4 / -0.1	1.3 / -0.8	0.5 / -0.9
b-tag light jet	0.3 / -1.4	0.5 / -0.4	0.6 / -0.5	0.2 / -0.6	0.9 / -0.4
JVF SF	1.3 / -1.2	1.4 / -1.3	1.0 / -1.3	1.3 / -1.4	1.7 / -1.3
ElectronEnergyScale	0.9 / -1.0	0.1 / -0.2	0.6 / -1.1	0.3 / -0.3	0.9 / -1.2
ElectronEnegyResolution	0.9 / -1.0	0.2 / -0.4	0.6 / -0.6	0.6 / -0.5	1.2 / -0.7
MuonMomentumScale	0.7 / -0.6	0.7 / -0.3	0.9 / -0.9	0.8 / -0.6	1.7 / -1.2
MuIDMomentumSmear	0.6 / -0.9	0.4 / -0.6	1.1 / -0.7	0.7 / -0.7	0.9 / -0.9
MuMSMomentumSmear	0.4 / -0.9	0.2 / -0.5	0.6 / -0.8	1.2 / -0.3	0.2 / -0.8
LeptonSF Trigger	2.2 / -1.8	0.8 / -0.6	0.5 / -0.5	0.9 / -1.1	1.3 / -0.7
LeptonSF Reco	1.5 / -1.2	0.8 / -0.0	1.0 / -0.4	0.4 / -0.7	1.4 / -1.4
LeptonSF ID	0.5 / -0.8	1.9 / -1.7	2.4 / -2.0	1.8 / -1.5	1.6 / -1.5
W+jets Normalization	0.7 / -0.9	0.4 / -0.4	0.4 / -0.5	0.4 / -0.5	0.8 / -1.1
QCD Normalization	0.4 / -0.4	1.3 / -0.8	1.1 / -1.1	1.6 / -2.8	2.6 / -2.4
QCD real eff.	0.9 / -0.8	0.2 / -0.5	1.0 / -0.9	1.5 / -0.7	1.0 / -1.2
QCD fake eff.	0.7 / -0.5	0.8 / -0.5	0.7 / -0.8	1.2 / -2.2	2.1 / -1.8
QCD shpae	1.0 / -0.6	0.3 / -0.5	0.5 / -0.7	0.6 / -0.5	0.7 / -1.2
Singletop, di-boson cross section	0.7 / -0.7	0.3 / -0.5	0.9 / -0.3	0.1 / -0.4	0.3 / -0.2
Parton shower Model	2.7 / -1.7	1.3 / -1.1	3.1 / -4.5	4.4 / -6.6	5.8 / -7.5
ISR/FSR	0.9 / -1.3	3.3 / -3.1	4.4 / -3.6	4.7 / -4.3	3.6 / -2.9
MC stat.	0.7 / -1.1	0.3 / -0.5	0.7 / -0.8	1.3 / -1.5	2.0 / -2.6

Table 11.5: Uncertainties for relative differential cross section for $y_{t\bar{t}}$ combined result. SVD unfolding technique is used.

$1/\mathrm{d}\sigma\ \mathrm{d}\sigma/\mathrm{d}y_{t\bar{t}}$	ℓ+jets					
Uncertainty (%)	-2.5 - -1.0	-1.0 - -0.5	-0.5 - 0.0	0.0 - 0.5	0.5 - 1.0	1.0 - 2.5
Total	11.5 / -10.4	9.4 / -8.1	8.8 / -7.3	8.7 / -7.9	9.6 / -8.3	11.2 / -9.7
Stat. only	2.8 / -2.8	3.9 / -3.7	3.3 / -3.2	3.1 / -3.1	2.8 / -2.6	2.5 / -2.7
Syst. only	11.1 / -10.0	8.6 / -7.2	8.2 / -6.5	8.2 / -7.3	9.1 / -7.9	10.9 / -9.3
Luminosity	0.5 / -1.0	0.8 / -1.4	0.7 / -1.2	0.2 / -0.6	0.6 / -0.5	0.4 / -0.6
JetEnergyScale	9.3 / -9.5	6.9 / -6.1	4.5 / -4.8	6.0 / -5.8	7.4 / -6.1	9.8 / -8.5
JetEnergyResolustion	0.7 / -0.4	1.6 / -1.3	0.7 / -1.6	0.4 / -0.7	1.2 / -1.8	1.0 / -0.9
JetRecoEfficiency	0.6 / -0.3	0.7 / -1.3	0.6 / -0.4	0.6 / -0.5	0.4 / -0.8	0.6 / -0.4
CellOut+SoftJet	0.7 / -0.5	1.0 / -0.8	1.3 / -0.9	0.7 / -0.8	0.5 / -0.8	0.3 / -0.7
Pileup	0.4 / -0.3	0.3 / -1.0	1.0 / -0.8	0.9 / -1.1	0.6 / -0.5	0.4 / -0.7
b-tag b-jet	5.0 / -4.6	4.9 / -4.3	4.9 / -4.2	4.7 / -3.6	4.5 / -3.5	4.4 / -3.4
b-tag c-jet	0.9 / -0.6	1.2 / -0.8	0.5 / -0.4	1.1 / -0.7	1.1 / -0.5	0.8 / -0.9
b-tag light jet	0.6 / -0.3	1.1 / -1.1	1.1 / -1.0	0.7 / -0.7	0.9 / -1.1	0.5 / -0.6
JVF SF	1.7 / -1.0	1.8 / -0.9	1.7 / -0.6	1.9 / -1.5	1.4 / -1.8	1.6 / -1.1
ElectronEnergyScale	0.1 / -0.5	1.2 / -0.4	0.7 / -0.4	1.2 / -0.3	0.7 / -0.6	1.1 / -1.3
ElectronEnegyResolution	0.6 / -1.0	0.9 / -0.8	0.4 / -0.7	0.3 / -1.1	1.1 / -0.6	0.7 / -1.2
MuonMomentumScale	0.8 / -0.3	0.6 / -0.9	0.6 / -0.5	0.5 / -1.0	1.2 / -1.2	0.5 / -0.6
MuIDMomentumSmear	0.6 / -0.2	1.1 / -0.4	1.3 / -0.3	0.4 / -1.0	0.4 / -0.3	0.6 / -1.1
MuMSMomentumSmear	0.7 / -0.9	0.5 / -0.8	0.5 / -1.2	0.8 / -0.3	0.4 / -0.8	0.7 / -0.8
LeptonSF Trigger	1.2 / -0.7	1.5 / -2.1	1.6 / -1.3	1.6 / -1.7	1.3 / -1.9	1.2 / -0.5
LeptonSF Reco	0.7 / -0.4	0.6 / -0.4	0.2 / -0.8	0.0 / -0.5	1.0 / -0.8	0.5 / -0.6
LeptonSF ID	1.0 / -1.2	1.2 / -1.0	1.1 / -0.2	0.9 / -0.7	0.4 / -0.3	1.4 / -0.6
W+jets Normalization	1.0 / -0.4	0.6 / -0.3	0.6 / -1.2	0.6 / -0.5	0.9 / -1.2	0.9 / -1.3
QCD Normalization	0.6 / -0.8	0.6 / -1.0	0.9 / -0.5	0.9 / -0.7	0.7 / -0.6	1.1 / -1.0
QCD real eff.	1.0 / -0.4	0.4 / -0.8	1.2 / -1.3	0.4 / -0.4	0.9 / -1.0	0.3 / -0.4
QCD fake eff.	0.8 / -1.1	1.0 / -0.9	1.1 / -0.5	0.5 / -1.0	0.4 / -0.2	0.5 / -0.6
QCD shape	0.3 / -0.6	0.6 / -0.7	1.2 / -0.6	0.8 / -0.9	0.2 / -1.0	0.6 / -1.0
Singletop, di-boson cross section	1.0 / -0.5	0.9 / -1.1	1.1 / -0.9	0.6 / -0.5	0.5 / -0.9	0.3 / -0.8
Parton shower Model	0.8 / -1.5	0.4 / -0.5	1.0 / -0.2	1.3 / -1.3	0.6 / -1.6	0.7 / -0.1
ISR/FSR	2.6 / -2.6	1.9 / -2.2	2.5 / -2.6	2.1 / -1.7	0.4 / -1.3	1.6 / -0.9
MC stat.	1.0 / -0.4	0.5 / -1.8	0.7 / -0.8	1.0 / -0.6	1.0 / -1.2	1.0 / -0.9

Table 11.6: Uncertainties for relative differential cross section for $y_{t\bar{t}}$ combined result. matrix inversion unfading technique is used.

$1/\mathrm{d}\sigma \ \mathrm{d}\sigma/\mathrm{d}y_{t\bar{t}}$	ℓ+jets					
Uncertainty (%)	-2.5 - -1.0	-1.0 - -0.5	-0.5 - 0.0	0.0 - 0.5	0.5 - 1.0	1.0 - 2.5
Total	4.5 / -4.9	3.4 / -3.6	3.0 / -3.1	3.4 / -3.2	3.8 / -3.9	4.4 / -4.3
Stat. only	3.8 / -3.8	3.2 / -3.1	2.7 / -2.9	2.8 / -2.8	3.2 / -3.1	3.8 / -3.4
Syst. only	2.4 / -3.1	1.3 / -1.8	1.4 / -1.2	2.0 / -1.4	2.1 / -2.4	2.3 / -2.6
Luminosity	0.3 / -0.7	1.1 / -0.9	0.2 / -0.6	0.3 / -0.9	0.5 / -0.8	0.7 / -0.8
JetEnergyScale	2.2 / -2.8	1.2 / -0.2	0.9 / -0.6	0.5 / -0.8	0.4 / -1.3	1.4 / -1.9
JetEnergyResolustion	1.8 / -1.1	0.6 / -1.0	0.5 / -0.5	1.8 / -1.8	2.1 / -2.1	1.4 / -1.0
JetRecoEfficiency	0.3 / -0.7	0.7 / -0.9	0.6 / -1.0	0.3 / -0.7	1.4 / -0.2	0.8 / -1.5
CellOut+SoftJet	1.2 / -0.6	0.9 / -0.7	0.6 / -0.8	1.0 / -0.8	0.4 / -1.4	1.1 / -0.3
Pileup	0.6 / -0.9	1.0 / -0.8	0.2 / -1.3	0.8 / -0.6	0.4 / -0.9	1.5 / -1.2
b-tag b-jet	1.4 / -1.1	0.4 / -0.5	0.5 / -0.9	1.2 / -0.7	0.8 / -1.4	0.9 / -1.8
b-tag c-jet	1.5 / -0.7	0.8 / -0.1	0.5 / -0.8	0.6 / -0.5	0.4 / -0.4	0.4 / -1.3
b-tag light jet	1.6 / -1.3	0.3 / -0.8	0.5 / -1.0	0.7 / -0.7	1.6 / -1.1	1.4 / -1.2
JVF SF	1.2 / -1.7	0.9 / -0.7	0.5 / -0.6	0.5 / -0.4	0.8 / -0.6	0.6 / -0.9
ElectronEnergyScale	1.7 / -0.7	0.2 / -1.1	0.7 / -1.0	0.9 / -0.4	1.0 / -0.9	0.9 / -1.4
ElectronEnegyResolution	1.5 / -1.8	0.6 / -0.6	0.3 / -1.2	1.0 / -0.4	1.3 / -1.5	0.8 / -1.0
MuonMomentumScale	0.4 / -1.6	0.6 / -1.2	0.9 / -1.2	0.2 / -0.2	1.1 / -1.7	0.8 / -1.2
MuIDMomentumSmear	1.0 / -1.1	0.3 / -1.1	0.5 / -0.9	0.8 / -0.2	0.6 / -1.0	1.2 / -1.1
MuMSMomentumSmear	1.2 / -0.4	0.9 / -0.7	0.4 / -0.9	0.4 / -0.8	0.3 / -1.4	0.7 / -1.3
LeptonSF Trigger	0.3 / -0.2	0.8 / -0.8	1.1 / -0.8	1.0 / -0.5	1.1 / -1.2	1.3 / -1.5
LeptonSF Reco	1.1 / -0.9	0.7 / -0.6	0.6 / -1.0	0.8 / -0.7	1.0 / -1.5	1.4 / -0.4
LeptonSF ID	0.7 / -0.6	1.2 / -0.2	0.6 / -1.3	0.3 / -0.4	1.2 / -0.6	0.8 / -1.5
W+jets Normalization	0.6 / -0.8	0.7 / -0.7	0.5 / -1.1	0.2 / -0.9	0.7 / -1.2	1.4 / -0.9
QCD Normalization	1.8 / -1.4	1.0 / -1.2	0.8 / -0.5	0.6 / -0.2	1.7 / -1.2	1.5 / -1.6
QCD real eff.	0.9 / -1.1	0.7 / -0.7	0.5 / -0.5	0.2 / -0.4	1.0 / -1.1	0.6 / -1.0
QCD fake eff.	1.6 / -1.7	0.7 / -0.6	0.5 / -0.6	0.6 / -0.6	0.2 / -1.1	0.7 / -1.3
QCD shape	0.4 / -1.1	0.9 / -1.0	0.7 / -0.9	0.4 / -1.2	1.1 / -1.5	1.1 / -0.3
Singletop, di-boson cross section	1.0 / -1.6	0.5 / -0.9	0.4 / -0.9	1.1 / -0.1	1.1 / -1.1	1.3 / -1.2
Parton shower Model	1.6 / -1.1	1.1 / -0.1	0.5 / -0.9	0.9 / -0.6	1.0 / -1.3	1.5 / -1.4
ISR/FSR	0.5 / -0.1	0.7 / -0.4	0.4 / -1.0	0.4 / -0.6	1.4 / -1.1	0.5 / -1.3
MC stat.	1.1 / -0.8	0.8 / -0.7	0.4 / -1.1	0.6 / -0.8	0.7 / -0.5	1.3 / -1.2

Chapter 12

Summary

The measurement of the relative differential cross sections of the top quark pair production as a function of the mass and the rapidity of the $t\bar{t}$ system in pp collisions at $\sqrt{s} = 7\,\mathrm{TeV}$ are presented. The objectives of this analysis are the verification of the standard model of the elementary particle physics and the search for the new physics beyond the standard model which couples to the top quark directly. This is the first measurement of the differential cross sections of the $t\bar{t}$ productions by the ATLAS experiment with full data of 4.7 fb[-1] in 2011. The measurement is based on the analysis of the lepton+jets decay channel of $t\bar{t}$ with b-tagging algorithm. For the measurement of the cross sections the final state of $t\bar{t}$ is reconstructed by the use of the likelihood fit with observed objects: a charged lepton, jets, b-tagged jets and missing transverse energy. The likelihood function for the kinematic fitting is constructed from the Breit-Wigner probability density function for resonance masses and the transfer function for observed energies/momenta. Expectations of the kinematics of the final states with simulated samples including background estimations are compared with data and we find that they agree each other. With the two different methods of the unfolding, the matrix inversion and the SVD approach, the differential cross sections at the generated parton level are obtained. By the test with simulated samples we confirm that both unfolding methods reproduce the original parton level distributions and their results are consistent with each other. The obtained differential cross sections are divided by the total production cross section of $t\bar{t}$ to avoid the systematic uncertainty in the overall normalization and are compared with the theoretical expectations. The cross section is also measured with the collision data as 160 ± 18 pb. The observed relative differential cross sections are compared with the higher order theoretical predictions, NLO and approximate NNLO based on the standard model, and are consistent with them within total errors. Since there is not enough statistics of data for high invariant mass region ($m_{t\bar{t}} > 950$ GeV), the sensitivity of the $m_{t\bar{t}}$ differential cross section measurement to new physics beyond the standard model is not enough with the current statistics of data and also with the current systematic errors of the measurement. Hence, no significant evidence of new physics is observed in this analysis.

The study of properties of the $t\bar{t}$ production processes is very important for the top quark associated Higgs boson production, $t\bar{t}H$, and for the search for SUSY and other new physics. The ATLAS detector already collected collision data of 22 fb[-1] at $\sqrt{s} = 8\,\mathrm{TeV}$ in 2012. We need to analyze this data with the higher statistics at the higher energy collision and to inspect the

new knowledge of the standard model or new physics at TeV scale.

Appendix A

Results of using signal sample MC@NLO

The results of the measurement for the top quark pair production differential cross section as a function of the mass and the rapidity of the $t\bar{t}$ system are shown. The efficiency and migration matrix derived from MC@NLO $t\bar{t}$ sample are used for unfolding and calculation of differential cross section. These are shown in Figure A.2 and A.1. The measurement that are used two unfolding technique of matrix inversion and SVD are presented respectively. To reduce total uncertainty for differential cross section, especially systematic uncertainty, the final unfolded differential cross sections are divided by the total production cross section and shown as relative differential cross sections. The total production cross section is measured with collision data of 4.7 fb^{-1} by eq. 9.6 and obtained result is 175 ± 21 pb. Both statistical and systematic uncertainties are included. Predicted standard model $t\bar{t}$ production cross section is 167^{+17}_{-18} pb for top quark mass of 172.5 GeV. This cross section has been calculated at approximate NNLO in QCD with Hathor 1.2 [55] using MSTW2008 PDF [56]. The measured total cross sections are consistent with standard model prediction within error. The final unfolded relative differential cross sections for $m_{t\bar{t}}$ and $y_{t\bar{t}}$ are shown in Figure A.3 and A.4 while tables are shown in Table A.1 and A.2. All results are after combining e+jets and μ+jets channel (denoted ℓ+jets).

(a) e+jets

(b) μ+jets
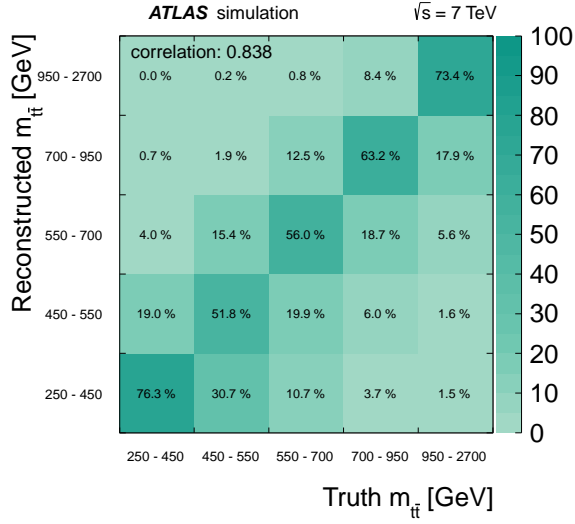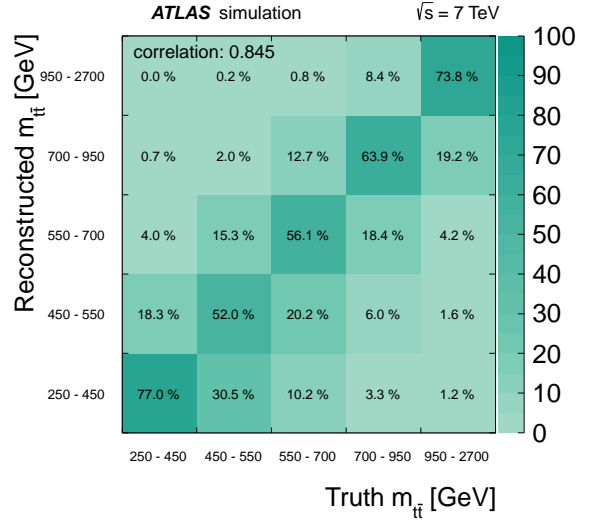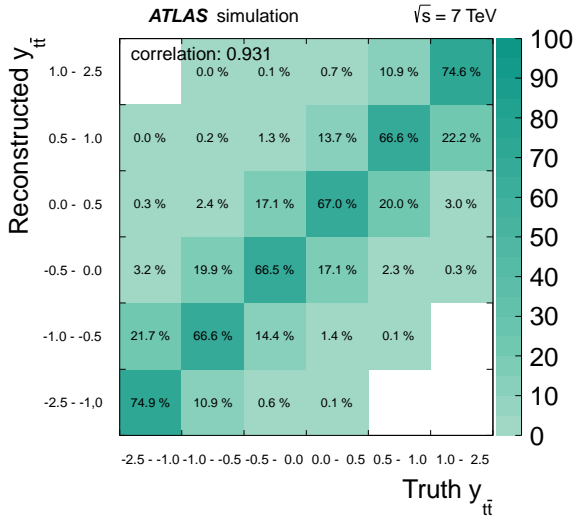
(c) e+jets
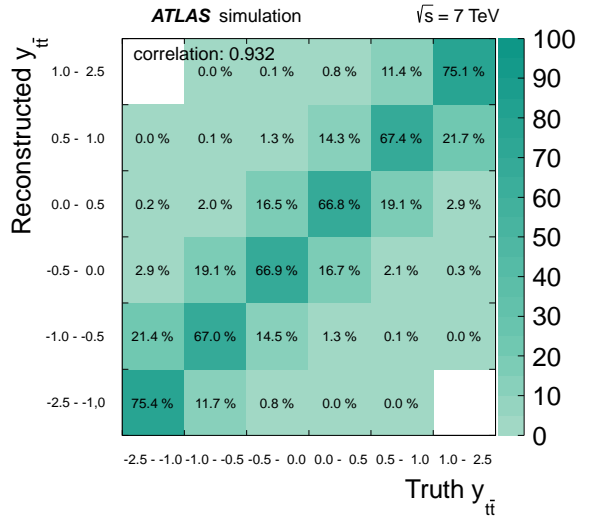
(d) μ+jets

Figure A.1: migration matrices for $m_{t\bar{t}}$ (A.1(a) and A.1(b)) and $y_{t\bar{t}}$ (A.1(c) and A.1(b)) derived from simulated $t\bar{t}$ events of MC@NLO passing all selection criteria and likelihood cut. The unit of the matrix elements is the probability for an event generated at a given value to be reconstructed at another value.

(a) e+jets

(b) μ+jets
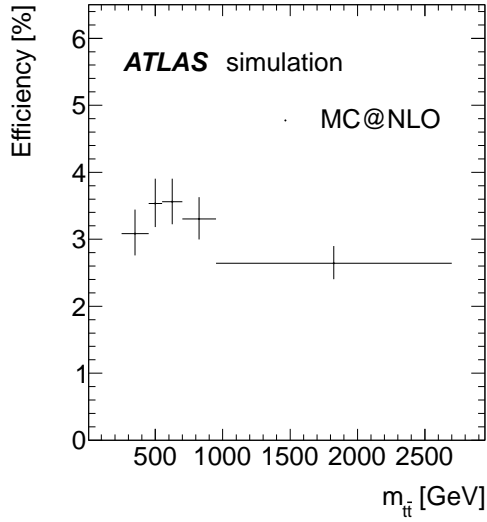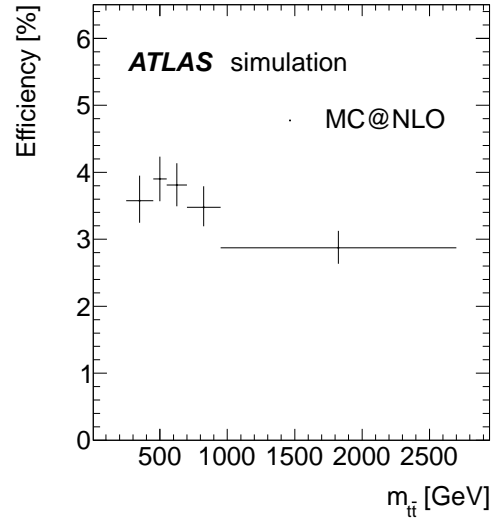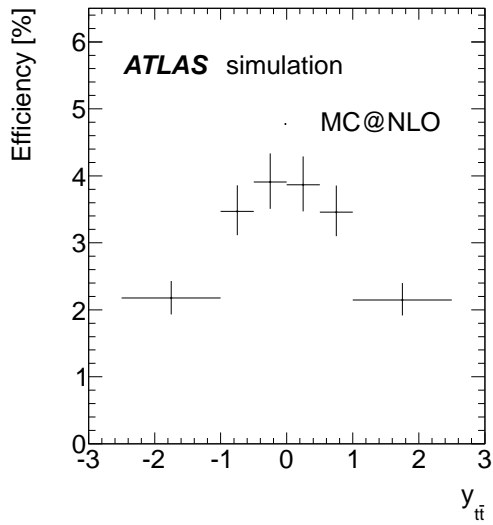
(c) e+jets
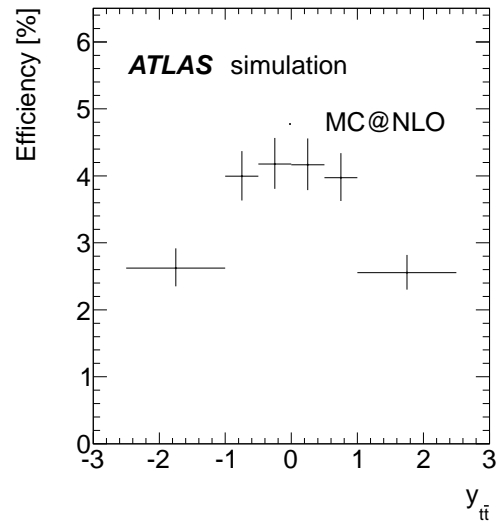
(d) μ+jets

Figure A.2: Efficiencies for $m_{t\bar{t}}$ (Figure A.2(a) and A.2(b)) and $y_{t\bar{t}}$(Figure A.2(c) and A.2(d)). The efficiency is defined according to Equation 9.3 and includes the branching ratio of $BR(t\bar{t} \rightarrow \ell+\text{jets} = 0.438)$ for $t\bar{t}$ lepton+jets channel.
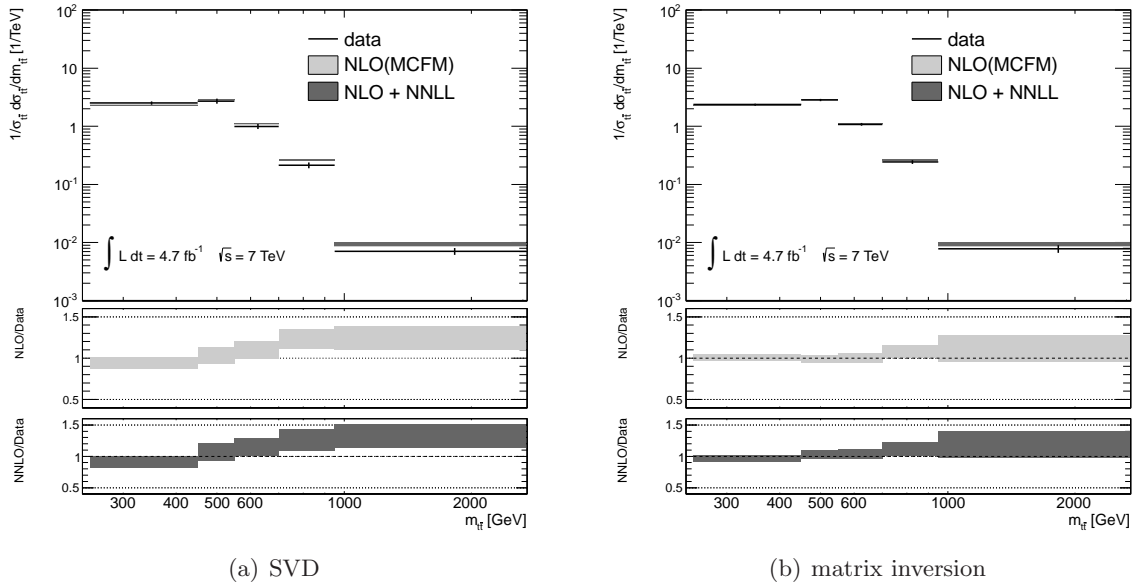
Figure A.3: Unfolded relative differential cross section using unfolding techniques of SVD and Matrix Inversion as a function of $m_{t\bar{t}}$ comparing to MCFM NLO and approximate NNLO theoretical predictions. The measured uncertainty which is 68% confidence level of pseudo-experiment result including statistical and systematic uncertainties is indicated by error bar in upper graph of each plot. The bands in the graph of relative differential cross section represent theory uncertainties. The graph bottom of relative differential cross section represents the ratio between theory prediction and observed result.

114

(a) SVD
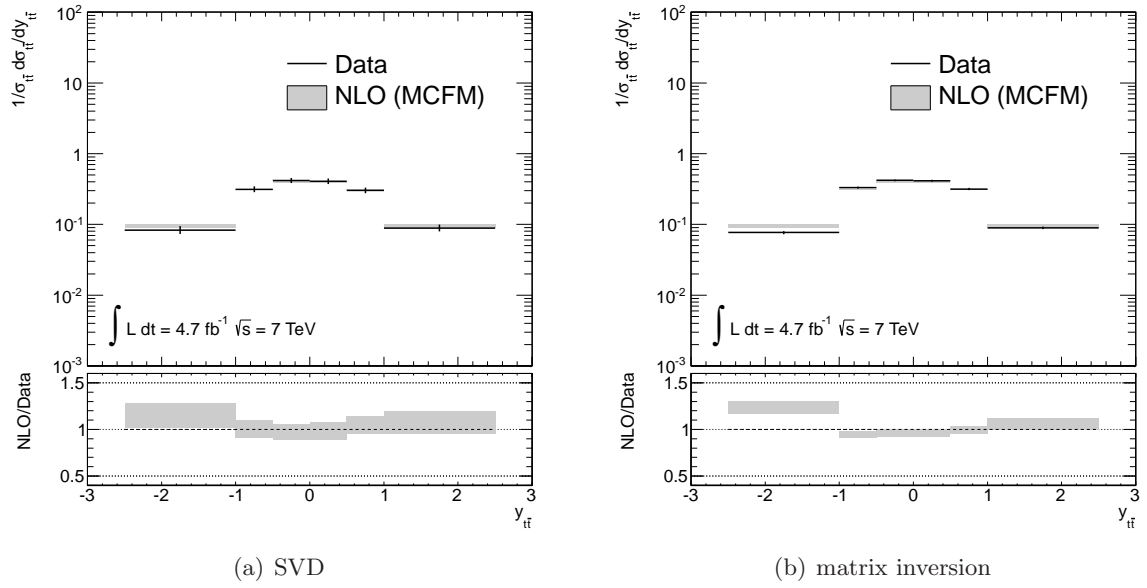
(b) matrix inversion

Figure A.4: Unfolded relative differential cross section using unfolding techniques of SVD and Matrix Inversion as a function of $y_{t\bar{t}}$ comparing to MCFM NLO prediction. The measured uncertainty which is 68% confidence level of pseudo-experiment result including statistical and systematic uncertainties is indicated by error bar in upper graph of each plot. The band in the graph of relative differential cross section represent theory uncertainty. The graph bottom of relative differential cross section represents the ratio between theory prediction and observed result.

Table A.1: Relative differential cross section for $m_{t\bar{t}}$ used SVD and matrix inversion unfolding technique.

$m_{t\bar{t}}$ (GeV)	$1/\sigma_{t\bar{t}} \, d\sigma_{t\bar{t}}/dm_{t\bar{t}}$ (1/TeV)	
	SVD	matrix inversion
250 - 450	2.5 ± 0.2	2.4 ± 0.1
450 - 550	2.7 ± 0.3	2.8 ± 0.1
550 - 700	$0.99 +0.11 / -0.09$	1.08 ± 0.06
700 - 950	$0.21 \pm 0.03 / -0.02$	0.24 ± 0.02
950 - 2700	0.007 ± 0.001	0.008 ± 0.001

Table A.2: Relative differential cross section for $y_{t\bar{t}}$ used SVD and matrix inversion unfolding technique.

$y_{t\bar{t}}$	$1/\sigma_{t\bar{t}} \, d\sigma_{t\bar{t}}/dy_{t\bar{t}}$	
	SVD	matrix inversion
-2.5 - -1.0	$0.083 +0.011/-0.010$	0.077 ± 0.004
-1.0 - -0.5	0.31 ± 0.03	0.33 ± 0.01
-0.5 - 0.0	$0.42 +0.04 / -0.03$	0.42 ± 0.01
0.0 - 0.5	$0.41 +0.04 / -0.03$	0.42 ± 0.01
0.5 - 1.0	0.30 ± 0.03	0.32 ± 0.01
1.0 - 2.5	$0.089 +0.011/-0.010$	0.090 ± 0.004

Acknowledgments

I would like to thank all peoples who directly contributed to this dissertation and indirectly helped me for the past three years at CERN and in Japan.

First of all, I would like to express the deepest appreciation to my supervisors Yoshinobu Unno and Junichi Kanzaki. I cause them so much trouble, and I could not finish the analysis and writing this thesis without them. Their support, suggestions, comments and encouragement were invaluable for me. Especially when I was preparing the presentation for Japanese national meeting and international conference, they take time out of their schedule in days and nights. Thank you so much for the past three years. Also I would like to express my gratitude to Katsuo Tokushuku of Co-leader of the ATLAS Japan Group. I thank him for the possibility to stay at CERN for three full years and travel around Europe and Japan. I could spend profitable days for my study at CERN.

I would like to offer special thanks to top differential cross section group conveners, Francesco Spaó, Jiří Kvita, Jörgen Sjölin and Lorenzo Bellagamba. Discussions with them have been extremely useful for my understanding and improvement of the analysis. Among others, Francesco gave me face-to-face conversation in his busy schedule. Additionally I would like to thank Karl Gellerstedt and Aras Papadelis for their significant contribution to development of unfolding framework which is the core of our analysis. Group members of Nancy Tannouly and Venkatesh Kaushik, they are early members of top differential cross section group. I shared good and bad times with them in this study from founding the analysis group. This study was my first full-fledged physics analysis. I was really confusing at the kick-off meeting, and I was really not sure what I should do. I have received a lot of advice from all member of top differential cross section group at the weekly meeting. Sometimes we discussed the details at the coffee space additionally. I could not have done this without them.

Besides, friends of mine, Keita Hanawa and Takayasu, we spent great time together at CERN. We talked about our study, had stupid chat, played softball, tennis and soccer, and had dumpling party. They would remain as a wonderful memory in Europe. My peers of SOKENDAI, Ayaki Takeda and Shingo Mitsui, we enjoyed the time of coffee break and dinner when I was back to Japan. And I would like to thank Yuko Honda who supported me with a lot of kindness and took care of my trips and other secretary works.

Finally I am deeply grateful to my parents and grandparents.

Bibliography

[1] S. L. Glashow, "Partial Symmetries of Weak Interactions", Nucl. Phys. **22**, 579 (1961); S. Weinberg, "A Model of Leptons", Phys. Rev. Lett. **19**, 1264 (1967); A. Salam, "Weak and Electromagnetic Interactions", Conf. Proc. C **680519**, 367 (1968). S. L. Glashow, J. Iliopoulos and L. Maiani, "Weak Interactions with Lepton-Hadron Symmetry", Phys. Rev. D **2**, 1285 (1970).

[2] G. Aad *et al.* [ATLAS Collaboration], "Observation of a new particle in the search for the Standard Model Higgs boson with the ATLAS detector at the LHC", Phys. Lett. B **716**, 1 (2012) [arXiv:1207.7214 [hep-ex]].

[3] J. Beringer *et al.* [Particle Data Group Collaboration], "Review of Particle Physics (RPP)", Phys. Rev. D **86**, 010001 (2012).

[4] F. Abe *et al.* [CDF Collaboration], "Evidence for top quark production in $\bar{p}p$ collisions at $\sqrt{s} = 1.8$ TeV", Phys. Rev. Lett. **73**, 225 (1994) [hep-ex/9405005].

[5] F. Abe *et al.* [CDF Collaboration], "Observation of top quark production in $\bar{p}p$ collisions", Phys. Rev. Lett. **74**, 2626 (1995) [hep-ex/9503002].

[6] S. Abachi *et al.* [D0 Collaboration], "Observation of the top quark", Phys. Rev. Lett. **74**, 2632 (1995) [hep-ex/9503003].

[7] *The Durham HepData Project*, http://hepdata.cedar.ac.uk/pdf/pdf3.html

[8] H. -L. Lai, M. Guzzi, J. Huston, Z. Li, P. M. Nadolsky, J. Pumplin and C. -P. Yuan, "New parton distributions for collider physics", Phys. Rev. D **82**, 074024 (2010) [arXiv:1007.2241 [hep-ph]].

[9] T. Affolder *et al.* [CDF Collaboration], "Measurement of the $t\bar{t}$ production cross section in $p\bar{p}$ collisions at $\sqrt{s} = 1.8$ TeV", Phys. Rev. D **64**, 032002 (2001) [Erratum-ibid. D **67**, 119901 (2003)] [hep-ex/0101036];

CDF Coolaboration "Measurement of the Top Cross Section in the Lepton+Jets Channel Using Simultaneous Kinematic Fits with 2.7 fb^{-1} of CDF Data", CDF Note 10137.

[10] V. M. Abazov *et al.* [D0 Collaboration], "$t\bar{t}$ production cross-section in $p\bar{p}$ collisions at $\sqrt{s}$ = 1.8-TeV", Phys. Rev. D **67**, 012004 (2003) [hep-ex/0205019];

DØ Collaboration, "Measurements of the $t\bar{t}$ Cross Section in the Lepton+Jets Channel with 4.3 fb^{-1}", DØ Note 60377-CONF

[11] [ATLAS Collaboration], "Measurement of the ttbar production cross-section in pp collisions at sqrts = 7 TeV using kinematic information of lepton+jets events", ATLAS-CONF-2011-121.

[12] G. Aad et al. [ATLAS Collaboration], "Measurement of the cross section for top-quark pair production in pp collisions at $\sqrt{s} = 7$ TeV with the ATLAS detector using final states with two high-pt leptons", JHEP **1205**, 059 (2012) [arXiv:1202.4892 [hep-ex]].

[13] [ATLAS Collaboration], "Measurement of $t\bar{t}$ production in the all-hadronic channel in 1.02 fb^{-1} of pp collisions at $\sqrt{s} = 7$ TeV with the ATLAS detector", ATLAS-CONF-2011-140.

[14] [ATLAS Collaboration], "Measurement of the top quark pair production cross section in the single-lepton channel with ATLAS in proton-proton collisions at 8 TeV using kinematic fits with b-tagging", ATLAS-CONF-2012-149.

[15] M. Aliev, H. Lacker, U. Langenfeld, S. Moch, P. Uwer and M. Wiedermann, "HATHOR: HAdronic Top and Heavy quarks crOss section calculatoR", Comput. Phys. Commun. **182**, 1034 (2011) [arXiv:1007.1327 [hep-ph]].

[16] *MCFM Monte Carlo for FeMtobarn processes*, http://mcfm.fnal.gov/

[17] V. Ahrens, A. Ferroglia, M. Neubert, B. D. Pecjak and L. L. Yang, "Renormalization-Group Improved Predictions for Top-Quark Pair Production at Hadron Colliders", JHEP **1009**, 097 (2010) [arXiv:1003.5827 [hep-ph]].

[18] J. Alwall, P. Demin, S. de Visscher, R. Frederix, M. Herquet, F. Maltoni, T. Plehn and D. L. Rainwater et al., "MadGraph/MadEvent v4: The New Web Generation", JHEP **0709**, 028 (2007) [arXiv:0706.2334 [hep-ph]].

[19] S. Frixione and B. R. Webber, "Matching NLO QCD computations and parton shower simulations", JHEP **0206**, 029 (2002) [hep-ph/0204244].

[20] M. L. Mangano, M. Moretti, F. Piccinini, R. Pittau and A. D. Polosa, "ALPGEN, a generator for hard multiparton processes in hadronic collisions", JHEP **0307**, 001 (2003) [hep-ph/0206293].

[21] J. Pumplin, D. R. Stump, J. Huston, H. L. Lai, P. M. Nadolsky and W. K. Tung, "New generation of parton distributions with uncertainties from global QCD analysis", JHEP **0207**, 012 (2002) [hep-ph/0201195].

[22] G. Corcella, I. G. Knowles, G. Marchesini, S. Moretti, K. Odagiri, P. Richardson, M. H. Seymour and B. R. Webber, "HERWIG 6: An Event generator for hadron emission reactions with interfering gluons (including supersymmetric processes)", JHEP **0101**, 010 (2001) [hep-ph/0011363].

[23] J. M. Butterworth, J. R. Forshaw and M. H. Seymour, "Multiparton interactions in photoproduction at HERA", Z. Phys. C **72**, 637 (1996) [hep-ph/9601371].

[24] [ATLAS Collaboration], "New ATLAS event generator tunes to 2010 data", ATL-PHYS-PUB-2011-008.

[25] B. P. Kersevan and E. Richter-Was, "The Monte Carlo event generator AcerMC version 2.0 with interfaces to PYTHIA 6.2 and HERWIG 6.5", hep-ph/0405247.

[26] T. Sjostrand, S. Mrenna and P. Z. Skands, "PYTHIA 6.4 Physics and Manual", JHEP **0605**, 026 (2006) [hep-ph/0603175].

[27] A. D. Martin, W. J. Stirling, R. S. Thorne and G. Watt, "Parton distributions for the LHC", Eur. Phys. J. C **63**, 189 (2009) [arXiv:0901.0002 [hep-ph]].

[28] S. Agostinelli *et al.* [GEANT4 Collaboration], "GEANT4: A Simulation toolkit", Nucl. Instrum. Meth. A **506**, 250 (2003).

[29] G. Aad *et al.* [ATLAS Collaboration], "The ATLAS Simulation Infrastructure", Eur. Phys. J. C **70**, 823 (2010) [arXiv:1005.4568 [physics.ins-det]].

[30] CERN HADRON LINACS, http://linac2.home.cern.ch/linac2/

[31] ATLAS Collaboration, "ATLAS: Detector and physics performance technical design report. Volume 1", CERN-LHCC-99-14.

[32] ATLAS EXPERIMENT Multimedia, http://www.atlas.ch/photos/index.html

[33] M. Cacciari and G. P. Salam, "Dispelling the N^3 myth for the k_t jet-finder", Phys. Lett. B **641**, 57 (2006) [hep-ph/0512210].

[34] M. Cacciari, G. P. Salam and G. Soyez, "The Anti-k(t) jet clustering algorithm", JHEP **0804**, 063 (2008) [arXiv:0802.1189 [hep-ph]].

[35] [ATLAS Collaboration], ATLAS-CONF-2010-054.

[36] [ATLAS Collaboration], "Jet energy scale and its systematic uncertainty in proton-proton collisions at sqrt(s)=7 TeV with ATLAS 2011 data", ATLAS-CONF-2013-004.

[37] The ATLAS collaboration, https://twiki.cern.ch/twiki/bin/view/AtlasPublic/JetEtmissApproved2011JetResolution

[38] [ATLAS Collaboration], "Performance of Missing Transverse Momentum Reconstruction in ATLAS with 2011 Proton-Proton Collisions at $sqrts = 7$ TeV", ATLAS-CONF-2012-101.

[39] G. Aad *et al.* [ATLAS Collaboration], "Expected Performance of the ATLAS Experiment - Detector, Trigger and Physics", arXiv:0901.0512 [hep-ex].

[40] [ATLAS Collaboration], "Commissioning of the ATLAS high-performance b-tagging algorithms in the 7 TeV collision data", ATLAS-CONF-2011-102.

[41] The Kalman Filter, http://www.cs.unc.edu/~welch/kalman/

[42] G. Piacquadio and C. Weiser, "A new inclusive secondary vertex algorithm for b-jet tagging in ATLAS", J. Phys. Conf. Ser. **119**, 032032 (2008).

[43] [ATLAS Collaboration], "Measurement of the b-tag Efficiency in a Sample of Jets Containing Muons with 5 fb^{-1} of Data from the ATLAS Detector", ATLAS-CONF-2012-043.

[44] [ATLAS Collaboration], "Measuring the b-tag efficiency in a top-pair sample with 4.7 fb^{-1} of data from the ATLAS detector", ATLAS-CONF-2012-097.

[45] [ATLAS Collaboration], "Performance of the ATLAS muon trigger in 2011", ATLAS-CONF-2012-099.

[46] The ATLAS collaboration, https://twiki.cern.ch/twiki/bin/view/AtlasPublic/MuonPerformancePublicPlots

[47] B. Andersson, G. Gustafson, G. Ingelman and T. Sjostrand, "Parton Fragmentation and String Dynamics", Phys. Rept. **97**, 31 (1983).

[48] S. Frixione, P. Nason and G. Ridolfi, "A Positive-weight next-to-leading-order Monte Carlo for heavy flavour hadroproduction", JHEP **0709**, 126 (2007) [arXiv:0707.3088 [hep-ph]].

[49] A. Hocker and V. Kartvelishvili, "SVD approach to data unfolding", Nucl. Instrum. Meth. A **372**, 469 (1996) [hep-ph/9509307].

[50] N. Kidonakis, "Next-to-next-to-leading-order collinear and soft gluon corrections for t-channel single top quark production", Phys. Rev. D **83**, 091503 (2011) [arXiv:1103.2792 [hep-ph]].

[51] N. Kidonakis, "NNLL resummation for s-channel single top quark production", Phys. Rev. D **81**, 054028 (2010) [arXiv:1001.5034 [hep-ph]].

[52] N. Kidonakis, "Two-loop soft anomalous dimensions for single top quark associated production with a W- or H-", Phys. Rev. D **82**, 054018 (2010) [arXiv:1005.4451 [hep-ph]].

[53] [ATLAS Collaboration], "Jet energy measurement and systematic uncertainties using tracks for jets and for b-quark jets produced in proton-proton collisions at $\sqrt{s} = 7$ TeV in the ATLAS detector", ATLAS-CONF-2013-002.

[54] [ATLAS Collaboration], "Characterization of Interaction-Point Beam Parameters Using the pp Event-Vertex Distribution Reconstructed in the ATLAS Detector at the LHC", ATLAS-CONF-2010-027.

[55] M. Aliev, H. Lacker, U. Langenfeld, S. Moch, P. Uwer and M. Wiedermann, Comput. Phys. Commun. **182**, 1034 (2011) [arXiv:1007.1327 [hep-ph]].

[56] A. D. Martin, W. J. Stirling, R. S. Thorne and G. Watt, Eur. Phys. J. C **63** (2009) 189 [arXiv:0901.0002 [hep-ph]].